Dynamical properties of a driven dissipative dimerized $S = \frac{1}{2}$ chain

M. Yarmohammadi,[1] C. Meyer,[2] B. Fauseweh,[3] B. Normand,[4,1,5] and G. S. Uhrig[1]

[1]*Lehrstuhl für Theoretische Physik I, Technische Universität Dortmund, Otto-Hahn-Strasse 4, 44221 Dortmund, Germany*

[2]*Institut für Theoretische Physik, Georg-August-Universität Göttingen, Friedrich-Hund-Platz 1, 37077 Göttingen, Germany*

[3]*Theoretical Division, Los Alamos National Laboratory, Los Alamos, New Mexico 87545, USA*

[4]*Paul Scherrer Institute, CH-5232 Villigen PSI, Switzerland*

[5]*Institute of Physics, Ecole Polytechnique Fédérale de Lausanne (EPFL), CH-1015 Lausanne, Switzerland*

(Received 2 October 2020; revised 16 December 2020; accepted 16 December 2020; published 22 January 2021; corrected 29 January 2021)

We consider the dynamical properties of a gapped quantum spin system coupled to the electric field of a laser, which drives the resonant excitation of specific phonon modes that modulate the magnetic interactions. We deduce the quantum master equations governing the time-evolution of both the lattice and spin sectors, by developing a Lindblad formalism with bath operators providing an explicit description of their respective phonon-mediated damping terms. We investigate the nonequilibrium steady states (NESS) of the spin system established by a continuous driving, delineating parameter regimes in driving frequency, damping, and spin-phonon coupling for the establishment of physically meaningful NESS and their related nontrivial properties. Focusing on the regime of generic weak spin-phonon coupling, we characterize the NESS by their frequency and wave-vector content, explore their transient and relaxation behavior, and discuss the energy flow, the system temperature, and the critical role of the type of bath adopted. Our study lays a foundation for the quantitative modeling of experiments currently being designed to control coherent many-body spin states in quantum magnetic materials.

DOI: 10.1103/PhysRevB.103.045132

I. INTRODUCTION

Both the advent of powerful new laser sources and the increasing demand for next-generation magnetic devices, required to power the information revolution, are focusing intensive research efforts on time-dependent phenomena in condensed matter. On the laser side, x-ray free-electron laser sources in the USA and Europe now allow the "ultrafast" probing of materials on the femtosecond timescales of their fundamental electronic and magnetic processes. On the device side, the immediate target is designer materials for antiferromagnetic (AF) spintronics [1,2], to enable the writing, storage, and reading of large-scale classical magnetic information with factor-1000 improvements over the current levels of speed and power consumption. Already on the horizon, however, is the development of magnetic materials as a route to encoding and manipulating quantum information, and indeed quantum information processing in systems with strong interaction energies would ensure very high-frequency operation at the lowest possible dissipation.

The concept of laser driving generalizes the pump-probe paradigm from simple pulse-delay schemes to the imprinting of arbitrary dynamics (within the limits of field control). The laser excitation of quantum systems has generated theoretical proposals for uniquely out-of-equilibrium states of matter, including nonequilibrium steady states (NESS) [3,4], nonequilibrium topological states [5], and many-body localization (MBL) [6,7]. To date these ideas have been tested largely on systems of ultracold atoms [8–11], where the laser controls the "optical lattice" on which the atoms reside [12]. The undeniable beauty of both the physical concepts and the technological achievements aside, these systems are neither very large nor very readily miniaturized.

Laser facilities operating on the energy and ultrafast timescales of condensed-matter systems have been deployed recently to observe a wide array of novel phenomena in graphene [13], superconductors [14], charge-density-wave materials [15,16], and correlated insulators near their metallic transition [17,18]. Beyond inducing, enhancing, or destroying a symmetry-broken state, a key focus of these experiments has been the high-frequency Floquet regime, where steady laser driving can induce new topological states [19,20], the "time crystal" [21], or more generally allow the "Floquet engineering" of the electronic bands [22,23].

While any material can be laser-driven, the key question is whether this driving creates a coherent quantum state [4]. Some of these new phenomena, notably photo-enhanced superconductivity [14], occur because the laser drives particular phonon excitations of the lattice hosting the electrons. Because strong laser driving can lead to very high populations of any targeted mode, exploiting the anharmonic part of the lattice restoring force leads to the concept of nonlinear phononics [24–26]. However, the phonon ensemble determines the temperature, and hence heating of the system is a fundamental issue in determining whether any of these novel laser-driven phenomena, and particularly their quantum nature, can survive beyond the initial ultrafast laser pulses.

Among the extensive body of theoretical studies of nonequilibrium quantum systems are analyses of short-time transient behavior caused by quenches [27–29], including those due to laser pulses [30,31], and of long-time thermalization behavior [28,32]. Ideas from (near-)integrable systems include MBL, which is known at least in one dimension [7], and prethermalization [33], while numerous studies have explored the Floquet regime [34]. Of the many numerical approaches to quenched or driven models, one of the most successful is nonequilibrium dynamical mean-field theory [35,36], which has been applied to many problems in cold atoms [37] and condensed matter [38–40]. However, these studies are largely restricted to fermionic systems and focus mostly on leading qualitative effects due to intrinsic system dynamics, rather than on the dynamics in the presence of dissipation.

By contrast, a realistic NESS requires a path for outflow of the injected energy [4]. The most general approach to describe a dissipative (open) quantum system is the Lindblad formalism [41], in which damping is provided by bath operators whose Hamiltonian dynamics are not required to formulate the equations of motion governing the time evolution of physical observables in the Heisenberg representation [42,43]. Recent studies of driven condensed-matter systems have included dissipative effects by using a phenomenological Gilbert damping [44], a phenomenological phonon damping [45], or numerical methods where a thermal bath of phonons [46–48], a temperature-independent fermionic bath [39,49], or both [50], form(s) part of the system on which calculations are performed. While these studies therefore consider NESS implicitly or explicitly, in fact none correspond to the problem of an open, driven quantum system subject to Lindblad dissipation processes, whose quantitative treatment is the aim of the current work.

For this purpose we will focus on quantum magnetic systems, which historically have provided a clean, readily realized, low-dissipation test bed for many concepts in condensed-matter and statistical physics. The small number and unique behavior of the spin degrees of freedom lead to exact solutions including the Heisenberg spin chain, the transverse-field Ising model, and the Kitaev model. In nonequilibrium physics, idealized (and often integrable) spin-chain models as the Hamiltonian part of a Lindblad system have provided the framework for illustrating NESS [51], MBL [52,53], Floquet prethermalization [54], and dynamical quantum phase transitions [55], as well as lending themselves very well to numerical investigation. With a view to future device application, single spins have long been considered as excellent candidate qubits and the application of suitable laser control schemes [4] has been attempted in ensembles of quantum dots [56,57]. The entangled quantum many-body states available in magnetic materials present not only a rich variety of options for encoding (protected) quantum information, keywords including (topological) magnonics [2,58–61], quantum spin liquids [62], and magnetic textures such as vortices [63] and skyrmions [64], but also many routes for exploiting intrinsic interactions [65–67] or extrinsic materials-design flexibility [68] to obtain "handles" for manipulating magnetism using laser light [69–71].

The reason why insulating quantum magnets are a relative latecomer to the game of laser excitation and pump-probe physics is the weak direct coupling of light to spin. In general one may consider four routes for the creation of magnetic excitations by incident light. (1) The response of metallic magnetic systems is usually described in terms of the inverse Faraday effect; this mechanism remains present (in the form of virtual electronic processes) in insulators and is quadratic in the electric-field strength of the light. It was exploited recently [72] to study the coherent transport of GHz precession modes of the magnetization over 100 μm distances in ferromagnetic iron garnet films. (2) At the intrinsic frequencies of magnetic modes in condensed matter, which are of order 1 THz, processes by which one photon creates one magnon depend on anisotropies in the spin Hamiltonian. While many forms of spin anisotropy exist, they are in general a consequence of spin-orbit coupling and thus they are rather weak in the most familiar quantum magnetic materials, whose magnetic ions are $3d$ transition metals. However, they are present in type-II multiferroics and other systems with finite magnetoelectric [73] and thermomagnetic coupling [74], and one such anisotropy was exploited in a recent discussion of a laser-pumped spin chain as a test case for a Generalized Gibbs Ensemble approach to near-integrable dissipative systems [46].

(3) The mechanism invoked most commonly in condensed matter emerges from the coupling of the electrons to an electromagnetic vector potential described by the Peierls substitution. In insulating magnets, the leading-order processes are of Raman type, where the scattering of one photon excites two magnon modes [75,76] and thus spin is conserved. For this type of process, the light frequency should be a significant fraction of the on-site Coulomb repulsion, U, of the electrons being excited virtually; because U is of order 5 eV, the incident light should be around the visible range. At lowest order, incident photons with frequency ω modify U to $U-\omega$ or $U+\omega$, thereby affecting the magnetic (super)exchange interaction. If one considers the effect of the electromagnetic field not on the (virtual) electronic hopping but on localized electronic energy levels, the interaction between two spins localized on sites i and j that have the same energy is not changed at linear order by the electric field. By contrast, if the energies on i and j are different, the electric field of the light can have a linear (albeit weak) influence on the exchange interactions. However, in the common situation where the atomic structure ensures a mirror symmetry between ions, this interaction vanishes.

(4) The lattice geometry is fundamental to the magnetic interactions, because exchange and superexchange processes are very sensitive to the distances and angles of the bonds between the ions along the exchange path. Thus the selective excitation of specific phonon modes would provide direct control of magnetic interactions through a mechanism resonant both between laser and phonon and between the selected phonon and the spin sector. By symmetry, the phonons must be infrared (IR)-active if they are to be driven directly by the light. Once the excitation of a phonon ensures that the atoms in a magnetic material are displaced, the modulation of the interactions is in general linear in the displacement coordinate; the structural complexity of most materials ensures both

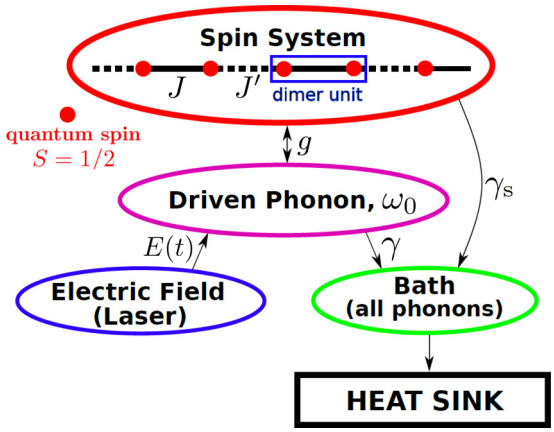

FIG. 1. Schematic representation of a lattice spin system, here a structurally dimerized chain with antiferromagnetic interaction parameters $J > J'$, driven by the selective excitation of one specific phonon mode of the lattice. Both the driven phonon and the spin system are damped by the ensemble of lattice phonons. We envisage an experimental geometry with the sample attached to an efficient heat sink for thermal regulation.

IR- and Raman-active phonons over a range of frequencies, and only for bond paths and displacement directions of especially high symmetry do the linear terms vanish.

We comment for completeness that recent experiments have used nonlinear mixing of two driven IR-active phonons to produce excitations at the sum and difference frequencies, whose symmetry compositions include Raman-active phonons [77] and magnetic modes [78]. While this mechanism should allow Raman-active phononic modulation of the magnetic interactions at quadratic order in the electric-field strength, it is important to distinguish such "nonlinear driving with harmonic phonons" [77,78] from "nonlinear phononics" [24]. The latter depends on anharmonic phonons and has been exploited to influence the electronic properties of correlated many-body states in superconductors [50,79–81] and Mott insulators [82]. Although nonlinear phononic effects on magnetism have to date been considered only in the form of creating effective static magnetic fields [83], more sophisticated protocols could be devised that provide a further channel for dynamical driving. Here we restrict our focus to the simple case of direct and coherent driving of the spin system by single, IR-active phonon modes in the harmonic regime. This situation was given the name "magnetophononics" by the authors of Ref. [84], who performed a theoretical study of classical magnets with phenomenological damping, and here we apply the magnetophononic protocol to a quantum spin system with quantum dissipation.

To discuss the dynamics of a driven dissipative quantum magnet we use the example of the alternating spin chain shown in Fig. 1. The driving is effected by laser excitation of an Einstein phonon that couples to one of the magnetic interactions in the spin chain and the dissipation is modeled in the Lindblad formalism by bath operators that damp both the lattice and spin sectors directly. We establish the equations of motion governing the basic physics of quantum NESS in this system, in terms of the driving frequency, the system parameters, and the response of the separate lattice and spin sectors. These equations enable us to discuss the different regimes of weak and strong spin-phonon coupling, of weak and strong damping, and all the timescales associated with driving, NESS formation, and relaxation. Thus our study establishes a foundation for many types of extension, specifically to different types of spin system, to different types of bath (characterized by whether they conserve spin and momentum), to finite system temperatures and thus to driving protocols for the management of heat and of coherence, and to quantitative studies of materials and device geometries for practical experiments.

The structure of this article is as follows. In Sec. II we present our model for the quantum spin chain, for the laser-coupled phonon mode that drives it, and for the Lindblad bath operators that damp it. We derive the equations of motion for the coupled lattice and magnetic sectors and comment on their structure. Section III contains a preliminary analysis of the content of these master equations, with specific attention paid to NESS. We demonstrate numerically that NESS can indeed be established, and illustrate how their basic properties are governed by the primary system parameters, namely, the driving power, the driving frequency, the lattice and spin damping coefficients, and the spin-lattice coupling. With this basis, in Sec. IV we concentrate on the regime of low spin-phonon coupling to perform a complete investigation of the dynamical properties of the NESS in the spin sector, characterizing their response by frequency, wave-vector components, and spin damping.

In Sec. V we turn to a different but essential aspect of NESS, namely, the transient processes occurring as they are established, from the moment the laser driving is switched on, and the relaxation processes by which equilibrium is restored when the drive is removed. At higher net occupancies of lattice and spin excitations we find anomalously slow convergence to NESS, and in Sec. V A we apply analytical arguments to discuss the underlying physics. Section V B extends this analysis to the question of limits in parameter space for the existence of NESS within our model framework, and Sec. V C provides a brief discussion of relaxation and temperature. In Sec. VI we analyze the energy flow in the NESS, considering both its uptake by the spin system as a function of laser power and frequency and its dissipation by the Lindblad terms. This allows us to provide experimentally oriented estimates for the rate of temperature increase in the driven system, for its control by the heat sink shown in Fig. 1, and the resulting timescales for read-out and control processes. In Sec. VII we discuss the context of our results from a number of angles, including methodology, the influence of the bath model, timescales and heating effects, and laser experiments on real materials. Section VIII consists of a brief summary and perspectives for future extensions of the framework established in this study.

II. MODEL AND METHODS

We begin by representing the Hamiltonian of the coupled system shown in Fig. 1 as

$$H = H_{\rm s} + H_{\rm sp} + H_{\rm p} + H_{\rm l}, \tag{1}$$

where the four terms describe, respectively, the spin system, the spin-phonon coupling, the Einstein phonon, and the effect of the laser electric field on this phonon. The bath operators damping the spin and lattice systems do not enter Eq. (1) explicitly, but are introduced at the level of the Lindblad formalism. While some authors have investigated the strong and controllable effects obtained by considering the quantum nature of the light field, generally referred to as "cavity QED" [85,86], for the purpose of driving phonon modes we treat the laser light field as classical.

A. Spin system

We express the Hamiltonian for the structurally dimerized, antiferromagnetic spin chain as

$$H_{\rm s} = \sum_i J\vec{S}_{1,i}\cdot\vec{S}_{2,i} + J'\vec{S}_{2,i}\cdot\vec{S}_{1,i+1}, \tag{2}$$

with $J > J' > 0$. For simplicity we consider only Heisenberg interactions between the spins and neglect any anisotropy terms; in real materials these could be of exchange, Dzyaloshinskii-Moriya, single-ion, g-tensor, or other origin, and as noted in Sec. I are generally weak in $3d$ transition-metal compounds. A representation particularly useful for dimerized spin systems is the bond-operator description [87,88], in which the Hamiltonian is transformed by expressing the two spin operators on each dimer using the identity

$$S^{\alpha}_{1,2} = \pm\frac{1}{2}(s^{\dagger}t_{\alpha} + t^{\dagger}_{\alpha}s) - \frac{1}{2}i\sum_{\beta\zeta}\epsilon_{\alpha\beta\zeta}t^{\dagger}_{\beta}t_{\zeta}, \tag{3}$$

where s and t_{α} ($\alpha = x, y, z$) are operators for the singlet and triplet states of each dimer (J) bond. These operators have bosonic statistics, required to reproduce the spin algebra of $S^{\alpha}_{1,2}$; however, because each dimer may be in only a singlet state or one of the three triplets (equivalent to the four possible states of two spin-1/2 entities), the bond operators must also obey a local hard-core constraint,

$$s^{\dagger}_i s_i + \sum_{\alpha} t^{\dagger}_{i,\alpha}t_{i,\alpha} = 1, \tag{4}$$

on each dimer i and hence are hard-core bosons.

For a system whose magnetic interactions are inversion-symmetric, the minimal Hamiltonian of Eq. (2) takes the form $H_{\rm s} = H_0 + H_2 + H_4$, where [88,89]

$$H_0 = \sum_i -J\left(\frac{3}{4}s^{\dagger}_i s_i - \frac{1}{4}t^{\dagger}_{i,\alpha}t_{i,\alpha}\right) - \mu_i(s^{\dagger}_i s_i + t^{\dagger}_{i,\alpha}t_{i,\alpha} - 1), \tag{5}$$

with summation over the repeated index α,

$$H_2 = -\frac{1}{4}J'\sum_{i,\alpha}(t^{\dagger}_{i,\alpha}t_{i+1,\alpha}s^{\dagger}_{i+1}s_i + t^{\dagger}_{i,\alpha}t^{\dagger}_{i+1,\alpha}s_i s_{i+1} + \text{H.c.}), \tag{6}$$

and

$$H_4 = \frac{1}{8}J'\sum_{i,\alpha\neq\beta}(t^{\dagger}_{i,\alpha}t^{\dagger}_{i+1,\beta}t_{i+1,\alpha}t_{i,\beta} - t^{\dagger}_{i,\alpha}t^{\dagger}_{i+1,\alpha}t_{i+1,\beta}t_{i,\beta} + \text{H.c.}). \tag{7}$$

The second term in H_0 enforces the constraint [Eq. (4)] using the Lagrange multipliers μ_i. At zero applied magnetic field, the term quadratic in the singlet operators is negative, which ensures a singlet condensation and justifies their replacement by a constant, $s_i = \langle s_i\rangle$, on each dimer. The ground state of the system is then a condensate of singlets with a spin gap to all triplet excitations, whose dispersion is specified by the quadratic terms in H_2. Here we will not consider any spatial gradients (for example, in temperature, magnetic field, or laser flux) and hence $\langle s_i\rangle = \bar{s}$ and $\mu_i = \mu$; the latter condition enforces the hard-core constraint at a global level, but not locally. For the purposes of the present analysis we will not consider triplet-triplet interactions, and thus we neglect H_4.

We transform the quadratic triplet Hamiltonian $H_0 + H_2$ to reciprocal space using

$$t_{i,\alpha} = \frac{1}{\sqrt{N}}\sum_k t_{k,\alpha}e^{-ikr_i}, \tag{8}$$

where N is the number of dimers, and express the result in the form

$$H_{\rm mf} = E_0 + \sum_{k,\alpha}\Bigg[\left(\frac{1}{4}J-\mu\right)t^{\dagger}_{k,\alpha}t_{k,\alpha} - \frac{1}{4}J'\bar{s}^2\cos k(t^{\dagger}_{k,\alpha}t_{k,\alpha} + t_{-k,\alpha}t^{\dagger}_{-k,\alpha} + t^{\dagger}_{k,\alpha}t^{\dagger}_{-k,\alpha} + t_{-k,\alpha}t_{k,\alpha})\Bigg], \tag{9}$$

where

$$E_0 = N\left[\left(-\tfrac{3}{4}J-\mu\right)\bar{s}^2 + \tfrac{5}{2}\mu - \tfrac{3}{8}J\right]. \tag{10}$$

We note that the only terms generated are those coupling operators at wave vectors k and $-k$, and there is no mixing of the triplet indices, α. The conventional approach [88,89] is to symmetrize the Hamiltonian matrix, diagonalize it to obtain a new bosonic quasiparticle, known as the triplon [90], form two mean-field equations, and solve these for μ and $\bar{s}$. By the use of effective quasiparticle statistics, this procedure may also be followed at finite temperatures [91,92].

Here we adopt one further simplification with a view to applying equation-of-motion methods. In the "Holstein-Primakoff" approximation [89], the singlet occupation is replaced directly by invoking the local constraint [Eq. (4)], giving

$$\bar{s}^2 = 1 - \frac{1}{N}\sum_{k,\alpha}t^{\dagger}_{k,\alpha}t_{k,\alpha}. \tag{11}$$

At quadratic order, this substitution reduces to the approximation $\bar{s} = 1$, $\mu = -\frac{3}{4}J$, which is clearly valid in the limit of a strongly dimerized chain. From extensive studies of the spin ladder [92], it is generally recognized that the bond-operator description retains semiquantitative validity for interaction ratios $J'/J \lesssim 1/2$ at low temperatures. For the present qualitative purposes, this approximation has the major advantage of not requiring a solution of the self-consistent equations at each time step.

From the spin Hamiltonian in the "mean-field" form

$$H_{\rm s} = \sum_{k,\alpha}\Bigg[Jt^{\dagger}_{k,\alpha}t_{k,\alpha} - \frac{1}{4}J'\cos k\,(2t^{\dagger}_{k,\alpha}t_{k,\alpha} + t^{\dagger}_{k,\alpha}t^{\dagger}_{-k,\alpha} + t_{k,\alpha}t_{-k,\alpha})\Bigg], \tag{12}$$

we diagonalize it by applying the Bogoliubov transformation

$$t_{k,\alpha} = \tilde{t}_{k,\alpha}\cosh\theta_k + \tilde{t}^\dagger_{-k,\alpha}\sinh\theta_k, \tag{13a}$$

$$t^\dagger_{k,\alpha} = \tilde{t}^\dagger_{k,\alpha}\cosh\theta_k + t_{-k,\alpha}\sinh\theta_k, \tag{13b}$$

where

$$\tanh 2\theta_k = \frac{\lambda\cos k}{2-\lambda\cos k} \tag{14}$$

with $\lambda = J'/J$, to obtain

$$H_s = \sum_{k,\alpha}\omega_k\tilde{t}^\dagger_{k,\alpha}\tilde{t}_{k,\alpha}. \tag{15}$$

The operators $\tilde{t}^\dagger_{k,\alpha}$ and $\tilde{t}_{k,\alpha}$ create and destroy the triplon modes of the dimerized chain and have dispersion relation

$$\omega_k = J\sqrt{1-\lambda\cos k}. \tag{16}$$

B. Phonon system and spin coupling

As shown in Fig. 1, we consider a situation in which the interaction J is modulated by the oscillations of one specific phonon mode on every bond. We take this to be an Einstein phonon with wave vector $q = 0$ and a finite energy, ω_0. As noted in Sec. I, we focus on the situation where this optical phonon is IR-active and hence is driven directly by the electric field of the incident light, and we do not consider the further possibilities offered by high-order phonon excitation processes. We assume that the laser illuminates the entire sample, meaning that we treat the driving as a bulk effect. In a real material, many different phonon modes are present in addition to the driven phonon, and all of them, in particular the acoustic phonons, are responsible for the dissipation of energy from both the lattice and spin sectors.

The Hamiltonian terms involving the driven phonon are

$$H_p + H_{sp} + H_l = \sum_j[\omega_0 b^\dagger_j b_j + g(b_j + b^\dagger_j)\,\vec{S}_{1,j}\cdot\vec{S}_{2,j} + E(t)(b_j + b^\dagger_j)], \tag{17}$$

where g is the spin-phonon coupling constant and $E(t) = a\cos(\omega t)$ is the oscillating electric field of the laser, which we assume to contain a single driving frequency, ω; as noted above, for the amplitudes a we consider, $E(t)$ may safely be treated as classical field. For our purposes, $E(t)$ is an internal field, meaning it is the fraction of the incident laser light transmitted into the sample, and we do not concern ourselves with the reflected component. The dissipative terms do not enter Eq. (17), but will be included using the Lindblad formalism in Sec. II C.

The transformation of Eq. (17) includes single- and triple-operator terms. For pedagogical accuracy we take a conventional definition of the Fourier transform,

$$b_j = \frac{1}{\sqrt{N}}\sum_q b_q e^{-iqr_j}, \tag{18}$$

under which the electric-field term becomes

$$\frac{E(t)}{\sqrt{N}}\sum_{j,q}(b_q e^{-iqr_j} + b^\dagger_q e^{iqr_j}) = \frac{E(t)}{\sqrt{N}}\sum_q(b_0 + b^\dagger_0), \tag{19a}$$

$$= NE(t)d, \tag{19b}$$

where only the $q = 0$ mode is selected, but we express it as an intensive quantity summed over q, with effective displacement operator $d = \frac{1}{\sqrt{N}}(b_0 + b^\dagger_0)$. Even more simply, the phonon term becomes $\sum_q \omega_0 b^\dagger_q b_q$.

Finally, the spin-phonon coupling term becomes

$$\frac{1}{N\sqrt{N}}\sum_{j,q,k,k',\alpha}(b_q t^\dagger_{k,\alpha}t_{k',\alpha}e^{i(k-k'-q)r_j} + \text{H.c.}) = \frac{1}{\sqrt{N}}\sum_{q,k,\alpha}(b_q t^\dagger_{k,\alpha}t_{k-q,\alpha} + b^\dagger_q t^\dagger_{k,\alpha}t_{k+q,\alpha}), \tag{20}$$

with $q = 0$ as the only relevant phonon mode. At the mean-field level one obtains the decoupled terms

$$H_{sp} = H_{sp,s} + H_{sp,p}, \tag{21a}$$

$$H_{sp,s} = g\langle d\rangle\left[\sum_{k,\alpha}t^\dagger_{k,\alpha}t_{k,\alpha} - \langle t^\dagger_{k,\alpha}t_{k,\alpha}\rangle_{eq}\right], \tag{21b}$$

$$H_{sp,p} = g\left\langle\sum_{k,\alpha}t^\dagger_{k,\alpha}t_{k,\alpha} - \langle t^\dagger_{k,\alpha}t_{k,\alpha}\rangle_{eq}\right\rangle d, \tag{21c}$$

where we have omitted the product of the two expectation values in Eq. (21a) because it has no influence at all on the dynamics of the system. Here $H_{sp,s}$ contains the operator part acting on the spin degrees of freedom, expressed in triplon operators, while $H_{sp,p}$ contains the operator part acting on the driven phonon. In both terms the spin-phonon interaction is expressed by deducting the equilibrium value of the triplon occupation, such that it has no effect when the system is not driven. While this mean-field decoupling is an approximation, we will show in Sec. VI that its quantitative limitations are minor.

To transform H_{sp} into the diagonal (triplon) basis of the spin sector, we use the identity

$$t^\dagger_{k,\alpha}t_{k,\alpha} = y_k(\tilde{t}^\dagger_{k,\alpha}\tilde{t}_{k,\alpha} + \tfrac{1}{2}) - \tfrac{1}{2} + \tfrac{1}{2}y'_k(\tilde{t}^\dagger_{k,\alpha}\tilde{t}^\dagger_{-k,\alpha} + \tilde{t}_{k,\alpha}\tilde{t}_{-k,\alpha}), \tag{22}$$

in which

$$y_k = \frac{1-\frac{1}{2}\lambda\cos k}{\sqrt{1-\lambda\cos k}} = \frac{J}{2}\frac{1+\omega_k^2/J^2}{\omega_k} \quad \text{and} \tag{23a}$$

$$y'_k = \frac{\frac{1}{2}\lambda\cos k}{\sqrt{1-\lambda\cos k}} = \frac{J}{2}\frac{1-\omega_k^2/J^2}{\omega_k}, \tag{23b}$$

to obtain the expression

$$H_{sp,s} = g\langle d\rangle\sum_{k,\alpha}\left\{y_k[\tilde{t}^\dagger_{k,\alpha}\tilde{t}_{k,\alpha} - n(\omega_k)] + \frac{1}{2}y'_k(\tilde{t}^\dagger_{k,\alpha}\tilde{t}^\dagger_{-k,\alpha} + \tilde{t}_{k,\alpha}\tilde{t}_{-k,\alpha})\right\}. \tag{24}$$

Here the bosonic occupation function, $n(\omega_k) = [\exp(\hbar\omega_k/k_BT) - 1]^{-1}$, provides an accurate value for the equilibrium occupancy of the triplon mode with frequency ω_k [Eq. (16)] at the low temperatures we consider, despite the hard-core nature of these modes [93].

We define the operators

$$u_k = \sum_\alpha \tilde{t}^\dagger_{k,\alpha}\tilde{t}_{k,\alpha} \quad \text{and} \tag{25a}$$

$$\tilde{v}_k = \sum_\alpha \tilde{t}^\dagger_{k,\alpha}\tilde{t}^\dagger_{-k,\alpha} \tag{25b}$$

in the triplon sector and denote their expectation values at any given time, t, by

$$u_k(t) = \langle u_k\rangle(t), \tag{26a}$$

$$\tilde{v}_k(t) = \langle \tilde{v}\rangle(t); \tag{26b}$$

the expectation value of the product of two annihilation operators is manifestly the complex conjugate of $\tilde{v}_k$,

$$\tilde{v}^*_k(t) = \sum_\alpha \langle \tilde{t}_{k,\alpha}\tilde{t}_{-k,\alpha}\rangle(t). \tag{27}$$

We comment that the triplon branch, α, is summed over here and, because we do not consider an applied magnetic field or any anisotropy in the spin Hamiltonian, will not enter our considerations again.

$u_k(t)$ is clearly a real variable due to the hermiticity of the operator on the right-hand side of Eq. (25), while the complex variable $\tilde{v}_k(t)$ is conveniently separated into its real and imaginary parts,

$$v_k(t) = \mathrm{Re}\,\tilde{v}_k(t), \tag{28a}$$

$$w_k(t) = \mathrm{Im}\,\tilde{v}_k(t). \tag{28b}$$

In the equations of motion to be derived in Sec. II C, the spin-phonon coupling introduces two quantities composed of the above expectation values, which we include by defining

$$\mathcal{U}(t) = \frac{1}{N}\sum_k y_k[u_k(t) - 3n(\omega_k)], \tag{29a}$$

$$\mathcal{V}(t) = \frac{1}{N}\sum_k y'_k v_k(t), \tag{29b}$$

both of which are real by construction. For the description of the spin sector in the driven system, we define the number, n_x, of elementary (Bogoliubov, or "dressed") triplons per site,

$$n_\mathrm{x}(t) = \frac{1}{N}\sum_k u_k(t), \tag{30}$$

and it will be helpful to compare this with the number of original (or "bare") triplons per site in the starting basis of Eq. (1),

$$n_\mathrm{b}(t) = \frac{1}{N}\sum_{k,\alpha}\langle t^\dagger_{k,\alpha}t_{k,\alpha}\rangle(t). \tag{31}$$

Using Eq. (22), this last definition is equivalent to

$$n_\mathrm{b}(t) = \mathcal{U}(t) + \mathcal{V}(t) + \frac{1}{N}\sum_{k,\alpha}\langle t^\dagger_{k,\alpha}t_{k,\alpha}\rangle_\mathrm{eq}, \tag{32}$$

in which the last term is given by

$$\frac{1}{N}\sum_{k,\alpha}\langle t^\dagger_{k,\alpha}t_{k,\alpha}\rangle_\mathrm{eq} = \frac{3}{2N}\sum_k[(2n(\omega_k)+1)y_k - 1]. \tag{33}$$

At zero temperature and for $\lambda = 1/2$, which will be our test case in what follows, the equilibrium expectation value is $n_{\mathrm{b}0} = 0.028$. This number quantifies the quantum fluctuations in equilibrium and will serve as a reference for the extent of modifications to the phonon-driven spin state relative to the undriven ground state.

C. Equations of motion

The time evolution of an open quantum system is specified by adjoint quantum master equations [42] of the form

$$\frac{d}{dt}A_\mathrm{H}(t) = i[H, A_\mathrm{H}(t)] + \sum_l \tilde{\gamma}_l\left[A^\dagger_l A_\mathrm{H}(t)A_l - \frac{1}{2}A_\mathrm{H}(t)A^\dagger_l A_l - \frac{1}{2}A^\dagger_l A_l A_\mathrm{H}(t)\right] \tag{34}$$

for any operator $A_\mathrm{H}(t)$ describing a physical observable. In these Heisenberg equations of motion, H is the Hamiltonian of the "reduced" system under consideration, by which is meant the quantum system with no environment. The "Lindblad" operators, $\{A_l\}$, are formed from the Liouville space of the reduced system to describe its interaction with the environment (the "bath"), which is excluded from explicit consideration. It was proven by Lindblad [41] that Eq. (34) is the most general form of the dissipation term for a separable (system-bath) Hilbert space when l describes a bounded set of operators. The coefficients $\tilde{\gamma}_l$ play the role of damping parameters.

The driven phonon exemplifies the textbook case [42,43] of the Lindblad equations, namely, those of the damped harmonic oscillator. The Lindblad operators in this case are $A_1 = b^\dagger_0$ and $A_2 = b_0$, with damping rates γ_1 and γ_2. For the system to relax back to its equilibrium state in the absence of driving, it is known [42] that the ratio of the two rates must be given by the ratio $n(\omega_0)/(1+n(\omega_0))$, and hence the conventional parametrization is

$$\tilde{\gamma}_1 = \gamma\, n(\omega_0), \tag{35a}$$

$$\tilde{\gamma}_2 = \gamma(1+n(\omega_0)), \tag{35b}$$

leaving only one damping parameter, γ. For physical transparency we separate the Lindblad operators into those that excite the system by an energy ω_l, which we denote by B_l, and those that de-excite, which are given by the Hermitian conjugates, $B^\dagger_l$. The dissipative part of Eq. (34), which is the second line, may then be separated into the two contributions

$$T_1 = \frac{1}{2}\sum_l \gamma_l n(\omega_l)\{[B_l,[A_\mathrm{H}(t),B^\dagger_l]]+[B^\dagger_l,[A_\mathrm{H}(t),B_l]]\}, \tag{36a}$$

$$T_2 = \frac{1}{2}\sum_l \gamma_l\{[B_l,A_\mathrm{H}(t)]B^\dagger_l + B_l[A_\mathrm{H}(t),B^\dagger_l]\}. \tag{36b}$$

The commutators in these expressions facilitate their rapid evaluation in comparison with the expression in Eq. (34); if the observable and the Lindblad operators are linear bosonic operators, as for the damped phonon, it can be seen without explicit calculation that the term T_1 vanishes and hence no dependence on the bosonic occupation, $n(\omega_l)$, arises.

To describe the driven phonon we consider the real variables

$$q(t) = \left\langle \tfrac{1}{\sqrt{N}}(b_0 + b_0^\dagger)\right\rangle(t), \tag{37a}$$

$$p(t) = \left\langle \tfrac{i}{\sqrt{N}}(b_0^\dagger - b_0)\right\rangle(t), \tag{37b}$$

$$n_{\rm ph}(t) = \left\langle \tfrac{1}{N} b_0^\dagger b_0\right\rangle(t), \tag{37c}$$

describing respectively the displacement of the Einstein phonon (d in Sec. II B), the conjugate phonon momentum, and the number operator. We recall that, despite the presence of all phonon modes, $b_q^\dagger$, in $H_{\rm p}$, only the operators b_0 and $b_0^\dagger$ appear elsewhere in the Hamiltonian of the reduced system and hence are candidates for the formation of Lindblad operators. The other phonons form the environment and their presence gives rise to the damping, which is contained in the single parameter γ.

By evaluating Eq. (34) or (36) with the expectation values from the spin sector [Eqs. (29)] in the spin-phonon coupling term, one obtains the closed set of equations of motion [42]

$$\frac{d}{dt}q(t) = \omega_0 p(t) - \frac{1}{2}\gamma q(t), \tag{38a}$$

$$\frac{d}{dt}p(t) = -\omega_0 q(t) - \frac{1}{2}\gamma p(t) - 2[E(t) + g(\mathcal{U}(t) + \mathcal{V}(t))], \tag{38b}$$

$$\frac{d}{dt}n_{\rm ph}(t) = -[E(t) + g(\mathcal{U}(t) + \mathcal{V}(t))]p(t) - \gamma[n_{\rm ph}(t) - n(\omega_0)]. \tag{38c}$$

One observes the characteristic structure in Eqs. (38a) and (38b) of the displacement and momentum serving as conjugate time derivatives, but damping themselves through the $\gamma/2$ term. The electric-field driving and the spin-system coupling appear only in the equation for the phonon momentum [Eq. (38b)]. The number operator reflects the driving of the momentum [Eq. (38c)] and also features as its own damping term, where $n(\omega_0)$ is the occupation of phonon mode ω_0 at thermal equilibrium. Here we do not extend these considerations to bilinear Lindblad operators in either the phonon or the spin sector.

Turning to the spin degrees of freedom, we consider the real expectation values $u_k(t)$, $v_k(t)$, and $w_k(t)$ introduced in Eqs. (26a) and (28) to describe the dynamical spin processes diagonal and off-diagonal in the triplon number basis. To determine the equations of motion, it is expected that the spin sector will be subject to a direct damping due both to weak spin-anisotropic terms and to phononic processes arising from the many acoustic and optical phonon modes in the Hamiltonian of any real material. The specific nature of these damping processes will be the subject of more extended discussion in Secs. IV and VII, but the available Lindblad operators will in general be linear and bilinear combinations of $\tilde{t}_k$ and $\tilde{t}_k^\dagger$. In the present analysis we focus on linear operators, in order to present the primary phenomena associated with the driven dissipative quantum spin chain. The equations of motion we will deduce have the analytical advantage of maintaining a simple form with transparent physical consequences. However, it is true that such one-triplon Lindblad operators are spin nonconserving, meaning that this type of bath is appropriate for materials with the non-negligible spin anisotropies more commonly associated with systems of $4d$ and $5d$ magnetic ions. Usually such anisotropic terms are nevertheless corrections to the spin Hamiltonian of Eq. (2), whereas they may be the leading dissipative terms; we discuss this situation in more detail, and comment on the case of spin-conserving bath operators, in Sec. VII.

Thus the Lindblad operators, B_k, that we consider are simply $\tilde{t}_{k,\alpha}^\dagger$, and have damping coefficient

$$\tilde{\gamma}_k = \gamma_{\rm s} n(\omega_k), \tag{39}$$

while $B_k^\dagger$ has damping $\gamma_{\rm s}(1 + n(\omega_k))$. We neglect a possible dependence of $\gamma_{\rm s}$ on the wave vector, k, along the chains. While one may ask whether this approximation constitutes a severe omission, given that energy and momentum conservation allow dissipation only for particular combinations of both, we observe that energy conservation as contained in Fermi's Golden Rule does not impose a strong constraint when one recalls that the one-dimensional (1D) chains are embedded in a three-dimensional (3D) crystal. Thus k-dependent damping coefficients, $\gamma_{\rm s}(k)$, are averaged over the transverse momentum, $\vec{k}_\perp$, and the assumption that energy conservation is satisfied at some value of $\vec{k}_\perp$ is fully justified. While some dependence of $\gamma_{\rm s}$ on the longitudinal momentum, k, may indeed remain, we proceed for the purposes of our present pedagogical exposition with a single value of $\gamma_{\rm s}$ for clarity.

To deduce the equations of motion when $A_{\rm H}(t)$ in Eq. (34) is one of the bilinear operator combinations in Eq. (25), we first consider the Hamiltonian parts of the respective expressions,

$$[H_{\rm s}, u_k] = 0, \tag{40a}$$

$$[H_{\rm s}, \tilde{v}_k] = 2\omega_k \tilde{v}_k, \tag{40b}$$

$$[H_{\rm sp,s}, u_k] = g q(t) y_k'(\tilde{v}_k^\dagger - \tilde{v}_k), \tag{40c}$$

$$[H_{\rm sp,s}, \tilde{v}_k] = 2g q(t)\left[y_k \tilde{v}_k + y_k'\left(u_k + \tfrac{3}{2}\right)\right]. \tag{40d}$$

Combining the unitary parts of Eqs. (40) with the dissipative part, T_2, from Eq. (36b), and taking the appropriate expectation values, leads to the final expressions

$$\frac{d}{dt}u_k(t) = 2g q(t) y_k' w_k(t) - \gamma_{\rm s}[u_k(t) - 3n(\omega_k)] \tag{41a}$$

$$\frac{d}{dt}v_k(t) = -2[\omega_k + g y_k q(t)] w_k(t) - \gamma_{\rm s} v_k(t) \tag{41b}$$

$$\frac{d}{dt}w_k(t) = 2[\omega_k + g y_k q(t)] v_k(t) + 2g q(t) y_k'\left[u_k(t) + \frac{3}{2}\right] - \gamma_{\rm s} w_k(t). \tag{41c}$$

In combination with Eqs. (38a)–(38c), these form the equations of motion for the coupled spin-lattice system. Regarding the structure of these equations, we comment only that $n_{\rm ph}(t)$ [Eq. (38c)] does not have any direct effect on the evolution of the other coupled equations and hence it appears that this variable can be neglected for dynamical purposes, but we will continue to show $n_{\rm ph}(t)$ as a valuable diagnostic of the state of the driven phonon sector.

Regarding the solution of these equations, in order to study the steady-state and dynamical properties of the driven and dissipative ensemble of Fig. 1, this will be our task in Secs. III and IV. In the majority of our calculations, we will use a periodic chain of $N = 400$ dimers and hence by inversion symmetry will have 201 independent values of k, which we will consider both separately and in summed quantities such as Eqs. (29) and (30). The equations of motion [Eqs. (38a)–(38c) and (41a)–(41c)] have no lower or upper validity cutoff in time, and thus can be applied to discuss the formation, switching, and relaxation of quantum spin NESS from $t = 0$ to ∞.

III. NESS IN THE PHONON-DRIVEN SPIN SYSTEM

We begin by choosing input parameters that establish quantum spin NESS, deferring a detailed analysis of the limits to NESS formation until Sec. V. Our first aim is a preliminary characterization of the response of NESS to the different factors influencing their driving. To reduce the space of possible driving parameters, in the present analysis we restrict our considerations to resonant excitation of the Einstein phonon mode, meaning that we select the laser frequency such that $\omega = \omega_0$ and hence $E(t) = a\cos(\omega_0 t)$. From a driving standpoint, for the electric-field intensities we wish to study and for a generically weak spin-phonon coupling, off-resonant driving is largely just a less efficient means, by a factor proportional to $[(\omega - \omega_0)^2 + (\gamma/2)^2]^{-1}$, of exciting a response at frequency ω. However, in systems with stronger spin-phonon coupling, nontrivial phenomena are indeed found by pumping and probing at frequencies $\omega \neq \omega_0$. We remind the reader that the minimal model of Sec. II A was not designed to describe driving by any of the other physical mechanisms summarized in Sec. I, all of which are less frequency-selective than phonon driving. It is easy to anticipate that the strongest effects of the driven phonon on the spin system will be found when ω_0 matches the spectrum of triplon excitations.

We consider first the driven phonon system without coupling to the spin chain, meaning with $g = 0$. To represent the phonons of a typical inorganic material we choose a damping coefficient $\gamma = 0.02\omega_0$. From Eqs. (38a)–(38c) one observes that, up to a coupling to the spin system (g) that is typically below 10%, the phonon has the behavior of a classical damped harmonic oscillator with a driving term. This is borne out by the time dependence of the variables q, p, and $n_{\rm ph}$, shown in Fig. 2. Figure 2(a) illustrates that the phonon number is driven up to a finite average value and the inset that it oscillates steadily around this constant value for all later times; this is the NESS of the driven phonon system. Figures 2(b) and 2(c) show the corresponding behavior of the displacement and momentum, which have a relative $\pi/2$ phase difference.

Several straightforward comments are in order. First, the phonon number operator in this laser-pumped steady state has been driven to a nonequilibrium average value of approximately 0.04. Although this value appears small, it does constitute a macroscopic occupation of a single mode. This driven ω_0 phonon is the primary source of lattice excitations in the system, and all other phonon modes will have very low occupations at low temperatures. In all of the considerations to follow, we maintain the value of $n_{\rm ph}$ in this range, both for meaningful comparisons as other parameters are varied and for a realistic account of the temperature of the steadily driven system, as we discuss in Sec. VI.

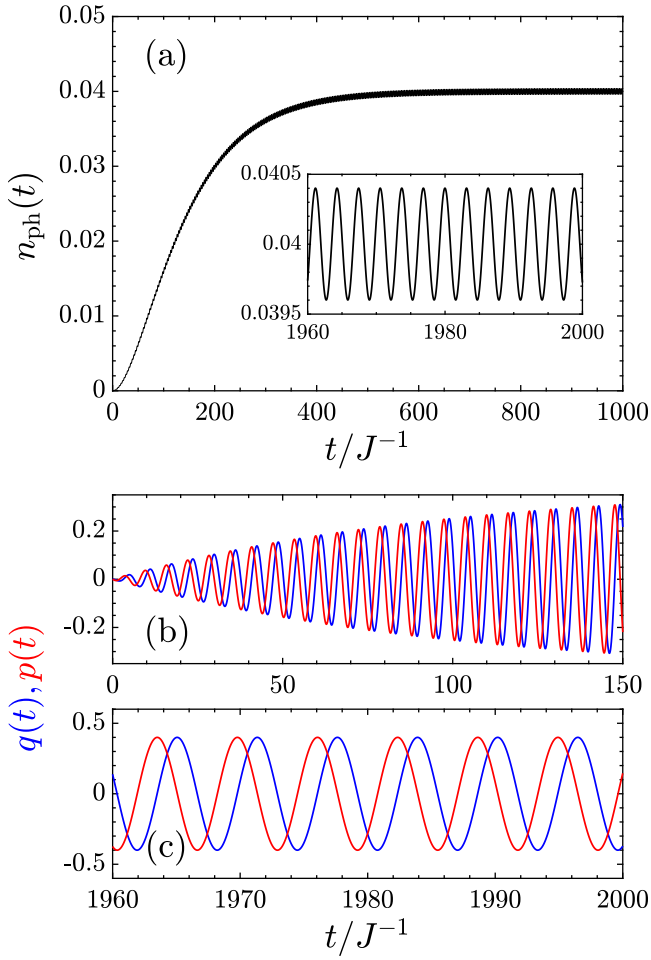

FIG. 2. Response of the Einstein phonon to a resonant driving field. Here $\omega_0/J = 1$, $a = 0.004J$, $\gamma = 0.02\omega_0$, and $g = 0$. (a) Phonon number, $n_{\rm ph}(t)$, produced by switching on a constant laser electric field at $t = 0$. The inset shows the steady state of the driven phonon system at long times. (b) Phonon displacement, $q(t)$, and momentum, $p(t)$, shown from $t = 0$. (c) $q(t)$ and $p(t)$ at long times.

Second, the frequency of the oscillations in the driven phonon occupation, $n_{\rm ph}(t)$, is twice that of $q(t)$ and $p(t)$, as expected from the number of nodes in the displacement cycle; the latter pair can be taken as the base frequency of the system, while the former is characteristic of $2\omega_0$, reflecting the fact that $n_{\rm ph}$ is essentially the sum of the squares of q and p. Third, the characteristic timescale for convergence of the average of $n_{\rm ph}$ to the phonon NESS is $2/\gamma$ for all three quantities [Figs. 2(a) and 2(b)]. For $q(t)$ and $p(t)$, this is to be expected from the corresponding equations of motion [Eqs. (38)], which contain explicit terms with prefactor $-\gamma/2$, while for $n_{\rm ph}(t)$ it is the behavior of $p(t)$ on the right-hand side of Eq. (38c) that induces the same convergence rate. Because the convergence is exponential, the actual establishment of a phonon NESS depends on the chosen accuracy criterion.

To a good approximation, the phonon number in the NESS [inset, Fig. 2(a)] is given by $n_{\rm ph}(t) = n_{\rm ph0} + n_{\rm ph2}\cos(2\omega_0 t)$;

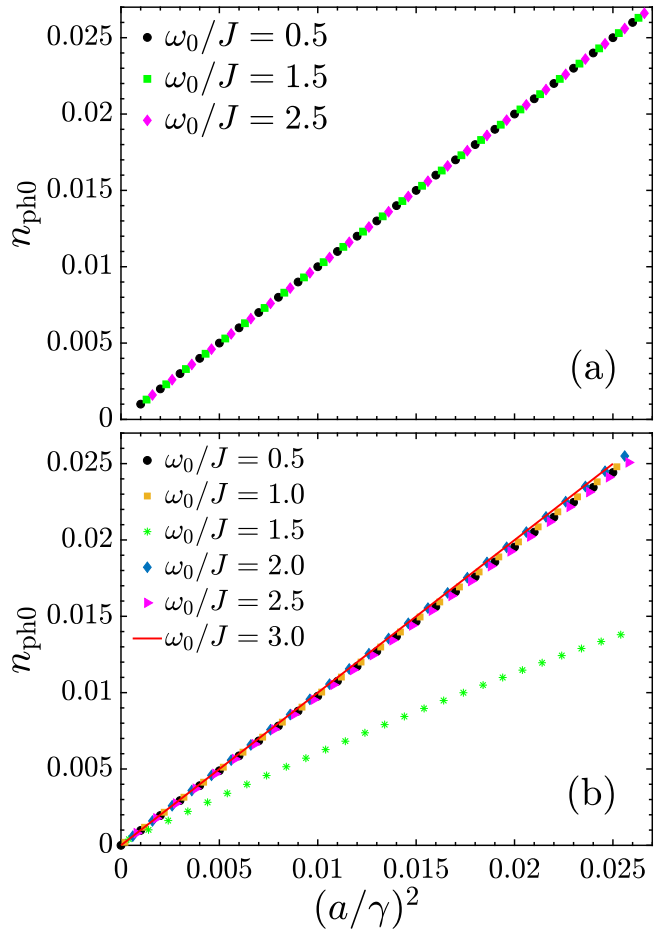

FIG. 3. Average value of the driven phonon occupation number, $n_{\rm ph0}$, in a NESS of the phonon system, displayed as a function of a^2 for various driving frequencies at fixed $\gamma = 0.02\omega_0$ and $\gamma_{\rm s} = 0.01J$. (a) No coupling to the spin system ($g = 0$). (b) $g = 0.1J$.

we will investigate the corrections to this situation, which arise due to coupling to the spin system, in Sec. IV. To study the quasistationary behavior of the NESS, we focus on the mean phonon occupation, $n_{\rm ph0}$. Figure 3(a) shows that, for all driving frequencies, the average energy in the driven phonon mode rises with the driving power, which is proportional to the square of the electric-field amplitude. In a fully classical treatment of the driven oscillator, $n_{\rm ph0} \propto (a/\gamma)^2$, and this result may equally be understood from Fermi's Golden Rule, where the flow of energy into the system is proportional to the square of the matrix element, and hence to a^2. We discuss the topic of energy flow in detail in Sec. VI. Because we have chosen for realism to scale γ to the phonon frequency, a will also be scaled to ω_0 in all of the studies to follow, thereby maintaining a constant $(a/\gamma)^2$ when ω_0 is varied.

The spin system is driven by the pumped phonon through the coupling parameter g. Given that the amplitude of the phonon oscillation, $q(t)$, is proportional to a/γ, it follows that the amplitude of the induced driving of the spin system is proportional to ga/γ. Figure 3 compares the driven phonon system with $g = 0$ to the situation with a finite value of g. Here we have chosen driving parameters suitable for the formation of NESS; those causing the spin system to inhibit NESS formation are the explicit focus of Sec. V. We observe in Fig. 3(b) that a generic spin-phonon coupling, $g = 0.1J$, results in only small changes being induced by the spin system relative to the isolated driven and damped phonons of most frequencies, but that some more significant alterations are possible at specific phonon frequencies, for reasons we investigate next.

Turning now to the response of the driven spin system, it is necessary first to establish the nature and characteristic frequencies of the excitations created by the driving phonon. Throughout the present study, we will consider the dimerized $S = 1/2$ chain of Sec. II A with an illustrative coupling ratio $\lambda = J'/J = 1/2$. Equation (16) states that the triplon modes of this chain form one triply degenerate branch dispersing from a value of $\omega_{\rm min} = J/\sqrt{2}$ at $k = 0$ to $\omega_{\rm max} = \sqrt{3/2}J$ at $k = \pi$. However, by spin conservation it is not possible for a phonon to create a single spin excitation, and from the form of $H_{\rm sp}$ in Eq. (17) it is evident that one phonon ($b_0^\dagger$) couples to two spin excitations. One therefore anticipates that the strongest effects of the driving phonon on the spin system will be found when ω_0 is chosen to lie within the band of two-triplon excitations, namely, when $2\omega_{\rm min} \leqslant \omega_0 \leqslant 2\omega_{\rm max}$ ($1.414J \leqslant \omega_0 \leqslant 2.449J$). Thus an origin for the special behavior of the $\omega_0/J = 1.5$ phonon in Fig. 3(b) is apparent immediately, although the detailed mechanism will not become clear until Sec. V.

In Fig. 4(a) we choose six driving phonon frequencies below, in, and above the two-triplon band, and consider the amplitude of the perturbation transferred to the triplon system by the phonon for a spin-phonon coupling parameter $g = 0.1J$. We include a direct spin damping, $\gamma_{\rm s} = 0.01J$, which we scale to the energy of the spin system; to reflect the observed fact that the spin degrees of freedom are in general very weakly damped, we also adopt a value that is significantly lower than the phonon damping over most of the range of ω_0. Figure 4(a) shows that laser driving at any frequency does create a response in the spin system that is qualitatively similar to that in the phonon system, namely, that the spin occupation is "pumped" to a new average value, about which it oscillates. At constant (a/γ), the average triplon occupation, $n_{\rm x0}$, displays a hierarchy of values as the NESS is approached. While at frequencies far from the two-triplon band ($\omega_0/J = 0.5$, 1.0, and 3.0) this degree of driving produces only a very weak occupation, $n_{\rm x0} < 0.001$ [inset, Fig. 4(a)], for frequencies in or near the band we find a state with $n_{\rm x0} \simeq 0.05$ at $\omega_0/J = 1.5$, but also one with an occupation of only $n_{\rm x0} \simeq 0.0006$ at the band center, $\omega_0/J = 2.0$.

Before discussing these occupation amplitudes, we demonstrate that each of the driven states is a true NESS. The detailed time structure, $n_{\rm x}(t)$, is shown for three selected frequencies in Figs. 4(b) to 4(d). In each case we compare the triplon occupation in a time window near the center of Fig. 4(a) with the long-time limit, for which we take the window $9960 \leqslant t \leqslant 10\,000$; we have shifted all the long-time traces by a phase $0 \leqslant \phi < 2\pi$ to start each cycle at the same point. The most important result of Figs. 4(b) to 4(d) is to prove that the driven model system damped by γ and $\gamma_{\rm s}$ does indeed host spin NESS, in that identical periodic traces are obtained for arbitrarily long times. The subsidiary result is that, for most ω_0 values, a good approximation to the NESS is reached already at rather short times. Because convergence is exponential, any meaningful accuracy criterion will be

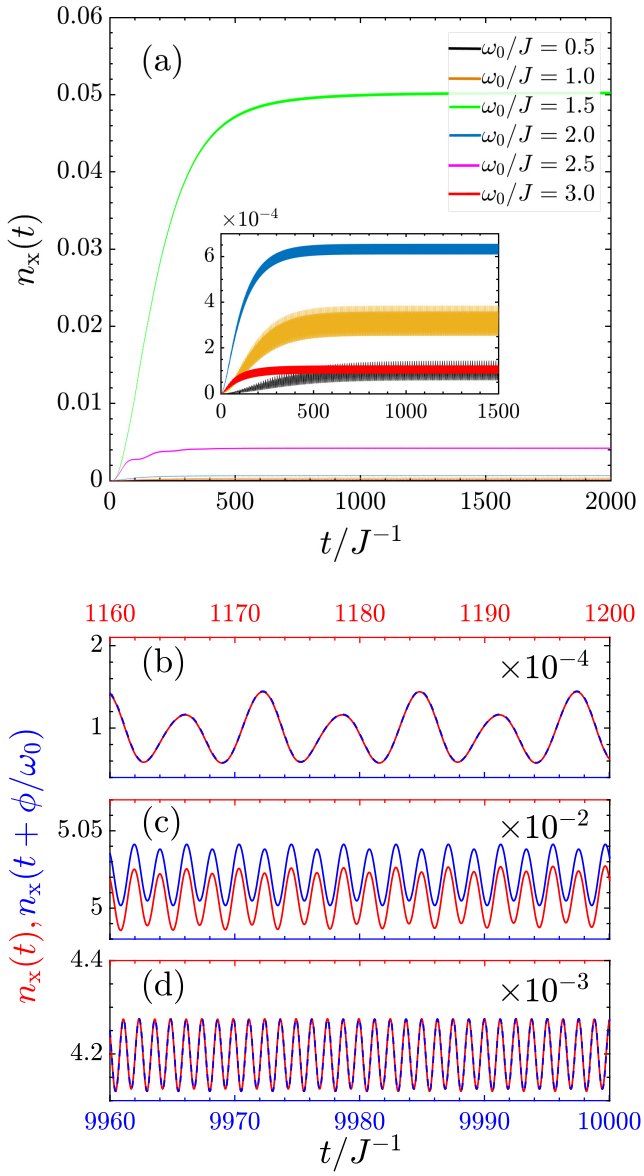

FIG. 4. (a) Response of the spin system, measured by $n_x(t)$ [Eq. (30)], to driving phonon frequencies $\omega_0/J = 0.5$, 1.0, 1.5, 2.0, 2.5, and 3.0. The driving field ensures that $a/\gamma = 0.2$ and we set $g = 0.1J$, $\gamma_s = 0.01J$. $n_x(t)$ in the spin NESS is shown at (b) $\omega_0/J = 0.5$, (c) $\omega_0/J = 1.5$, and (d) $\omega_0/J = 2.5$, where we compare results in the time window $1160 \leqslant t \leqslant 1200$, meaning after a small number of spin-system time constants, with those at $9960 \leqslant t \leqslant 10\,000$, meaning at truly long times.

reached after a single-digit number of time constants, and thus for quantitative purposes (Sec. VI), bearing experimental uncertainties in mind, we define a NESS to exist using a relative criterion of 2% (corresponding to approximately $4/\gamma_s$). According to this criterion, the driven state in Fig. 4(c) is not yet a NESS, for reasons we will revisit below, but those shown in Figs. 4(b) and 4(d) are.

As a benchmark for the meaning of the n_{x0} values in Fig. 4, one may compare with the value $n_{b0} = 0.028$ deduced below Eq. (33) (Sec. II B), which expressed the mixing of dimer singlet and triplet states due to the quantum spin fluctuations in the pure spin chain. Thus by inspection of the average nonequilibrium triplon populations characterized by n_{x0}, one may state that the spin NESS established at low and high frequencies constitute only a weak perturbation of the equilibrium state. This result also implies that in the "Floquet" regime of frequencies above the two-triplon band, the spin state is not altered qualitatively, although it may obtain a nontrivial phase structure. By contrast, for some frequencies in and around the two-triplon band, the quantum spin NESS can be altered significantly from the equilibrium state, and our results for $\omega_0/J = 1.5$ suggest that rather modest phonon driving at certain frequencies can create an essentially different type of triplon system. We will characterize these qualitatively new states in detail in Sec. IV.

Here we note that the hard-core nature of the dimer spin states sets an absolute upper limit of $n_x = 1$ on the triplon occupation, and in fact such a situation would represent the most extreme out-of-equilibrium state possible, at which many of the approximations in Sec. II A would no longer be valid. Anticipating the discussion of Secs. IV and V A, we introduce an operational threshold value of $n_x(t)$ in the driven spin state, such that our description of the spin sector will remain appropriate, and we set this to $n_x^{\max} = 0.2$.

In addition to the order-of-magnitude differences observed in n_{x0} as a consequence of the driving frequency, Fig. 4 invites two further remarks. First, we observe that the time structure, $n_x(t)$, of the NESS in Figs. 4(b) to 4(d) shows a rather complex form, with a definite superposition of different frequency harmonics in evidence. We will investigate this harmonic mixing, which appears to be strongest at the below-band frequency of Fig. 4(b), in detail in Sec. IV. Second, the timescale over which the spin system reaches its NESS appears to be similar at all frequencies, other than $\omega_0/J = 0.5$ and 1.5, at $t \approx 400J^{-1}$. This value corresponds to approximately four time constants of the spin system ($1/\gamma_s$). Of the exceptional cases, at $\omega_0/J = 0.5$, where $\gamma_s = \gamma$, the process is somewhat delayed by the phonon "switch-on" timescale (Fig. 2). At $\omega_0/J = 1.5$, the process appears to be longer still, with the NESS not yet fully established after $t = 1200J^{-1}$ [Fig. 4(c)]. We will investigate the transient behavior of the spin system at switch-on, and explain this curiously slow convergence, in Sec. V A.

We conclude our initial survey of spin NESS in response to a driving phonon by showing the spin-system analog of Fig. 3. In the analysis of experiments, a key quantity in characterizing any phenomenon is its dependence on the power, or fluence, of the laser, which is quite straightforward to measure. From elementary electrodynamics, the fluence is proportional to the squared amplitude of the laser field, and hence in Fig. 5(a) we show the dependence on a^2 of the average triplon occupation, n_{x0}, in the NESS for the six representative driving frequencies. As for the driven phonon, the dependence is clearly linear over the full range of γ-normalized a^2 values for all driving frequencies, again except for $\omega_0/J = 0.5$ and $\omega_0/J = 1.5$. The latter shows a saturation as n_{x0} is driven towards unphysical values at very large a, while the former shows a crossover to a dependence that it as least quadratic in $(a/\gamma)^2$ at strong driving. Next (Sec. IV) we discuss the dynamical properties of the driven NESS, which will allow us to understand the origin of this form, after which (Sec. V) we will address the issue of limits on $(a/\gamma)^2$ for spin NESS to exist at long driving times.

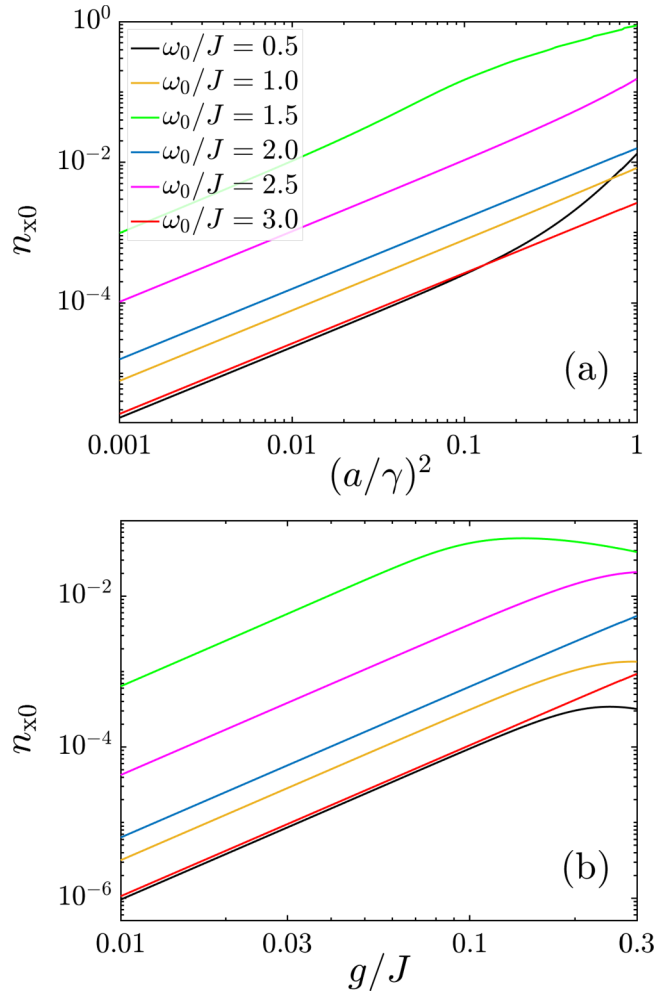

FIG. 5. (a) Dependence of the average triplon number, n_{x0}, in the NESS on the fluence, shown as $(a/\gamma)^2$, at driving phonon frequencies $\omega_0/J = 0.5$, 1.0, 1.5, 2.0, 2.5, and 3.0. The fixed system parameters are $g = 0.1J$, $\gamma = 0.02\omega_0$, and $\gamma_s = 0.01J$. Only the $\omega_0/J = 0.5$ and 1.5 phonons at very high fluences show deviations from a linear form. (b) Dependence of n_{x0} on the spin-phonon coupling constant, g, for driving phonons of the same six frequencies at fixed $a/\gamma = 0.2$. A well-defined g^2 dependence at all small couplings gives way to a suppression of n_{x0} at larger g values whose onset depends on ω_0.

In Fig. 5(b) we show the dependence of the driven triplon occupation on the spin-phonon coupling, g, for the same six driving frequencies. At low values of g, n_{x0} shows a g^2 form that is directly analogous to its dependence on a^2. However, at high g we observe a suppression of n_{x0} below its expected value, the onset of which occurs at lower g for the phonons closest to resonance with the two-triplon band, and find that the spin response can even decrease as the coupling is increased. This onset of more complex behavior, which is also evident in the response of the $\omega_0/J = 1.5$ phonon in Fig. 3(b), allows us to define a regime of "weak" (or "linear") spin-phonon coupling, which terminates around $g = 0.08J$, and a "strong-coupling" regime. Most magnetic quantum materials do not show strong spin-phonon coupling at equilibrium, and thus for the purposes of the present analysis, which is to discuss the properties of a generic driven quantum magnet, we will focus on the weak-coupling regime. Hence we adopt the value $g = 0.05J$ to be representative of the class of magnetic materials in which to seek linear quantum spin NESS phenomena.

In this weak-coupling regime, one may exploit the equivalence of a and g to define a dimensionless effective driving parameter for the spin system,

$$D = ga/(\gamma J), \tag{42}$$

which can be used to simplify the analysis, and we will employ this parameterization in Sec. V. However, when working beyond this regime it is not possible to avoid studying the full space of a/γ and g. Although we defer the analysis of strong coupling to a later study, we stress that all of the treatment in Sec. II remains fully valid for all the g values shown in Fig. 5(b). Nevertheless, as we will mention in Sec. VII, values of g up to $0.5J$ are known in some dimerized-chain compounds, and for such extreme spin-phonon coupling one may not exclude the possibility of a different type of physics at equilibrium, such as the formation of combined phonon-triplon entities; we comment only that the formalism of Sec. II would not be appropriate for such a situation.

IV. DYNAMICAL PROPERTIES OF THE QUANTUM SPIN NESS

We turn now to a quantitative analysis of the dynamics of the spin NESS. It is already clear from Sec. III, and particularly Fig. 4, that the superposition of frequencies present in the steady state can be complex. For full insight into the harmonic content of the spin NESS, we introduce the Fourier transform (FT) of the NESS signal, which we apply to $n_{ph}(t)$, to the individual spin components, $u_k(t)$ and $v_k(t)$, and to the summed quantities $n_x(t)$ [Eq. (30)] and

$$V(t) = \frac{1}{N}\sum_k v_k(t), \tag{43}$$

which characterize respectively the average triplon occupation and the average behavior in the off-diagonal two-triplon sector. The definition of the FT is simplied by making use of the results in shown in Fig. 4, where we demonstrated that NESS had been achieved at long times. We use one cycle of the signal taken from the time window $9960 \leqslant t/J^{-1} \leqslant 10\,000$ to determine the coefficients of the Fourier series

$$X(t) = \sum_m X_m \exp(im\omega t) \tag{44}$$

for any quantity X appearing in a NESS driven by any frequency ω; with this notation, any quantity with an integer subscript (X_m) denotes a Fourier component, and those with $m = 0$ are all real numbers. Without performing a detailed analysis beyond the level of Fig. 4, we comment that the system described by the model of Sec. II does not generate any significant dynamics at frequencies other than $m\omega$, where m is an integer. We also comment that there are no discernible extrinsic features arising in the FT as a consequence of the finite length of the chain on which we perform our calculations.

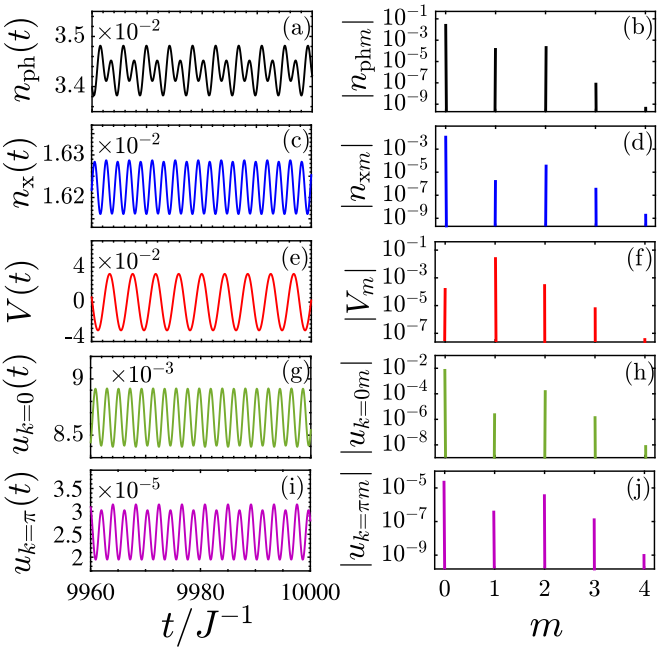

FIG. 6. Illustration of the quantities (a) $n_{\rm ph}(t)$, (c) $n_{\rm x}(t)$, (e) $V(t)$, (g) $u_{k=0}(t)$, and (i) $u_{k=\pi}(t)$ in the NESS obtained with driving parameters $a/\gamma = 0.2$ and $g = 0.05J$ at frequency $\omega_0/J = 1.5$ in the presence of spin damping $\gamma_{\rm s} = 0.01J$. Panels (b), (d), (f), (h), and (j) show the corresponding Fourier decompositions.

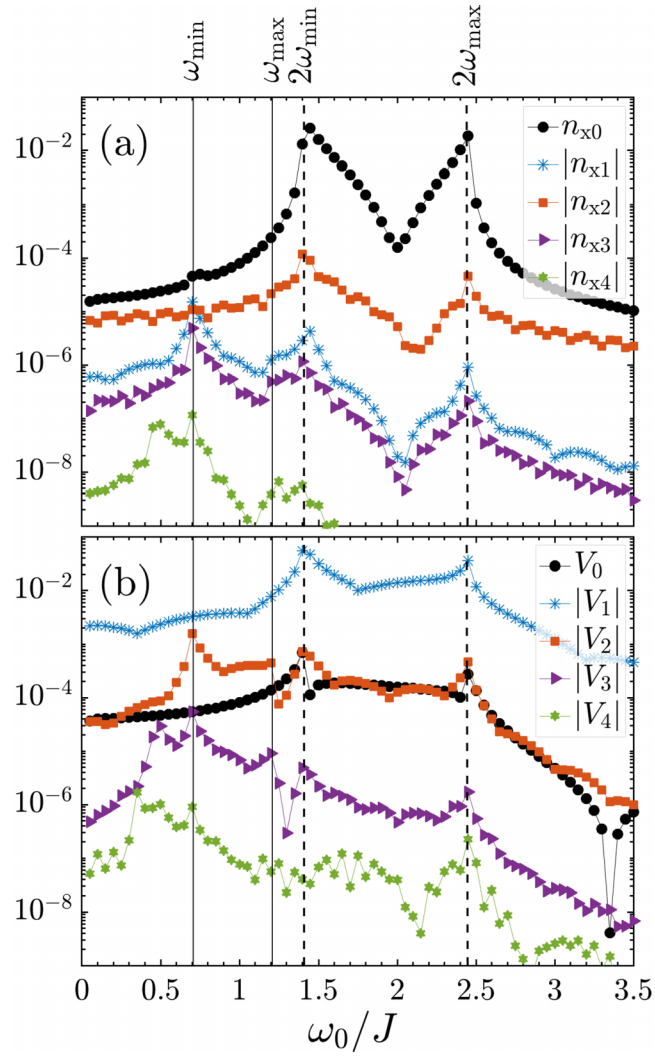

FIG. 7. Coefficients of the Fourier transforms of (a) $n_{\rm x}(t)$ and (b) $V(t)$ in the NESS obtained with driving $a/\gamma = 0.2$ and $g = 0.05J$, shown as a function of the driving phonon frequency, ω_0, for damping parameters $\gamma = 0.02\omega_0$ and $\gamma_s = 0.01J$.

Returning to the case of resonant driving ($\omega = \omega_0$), we illustrate the FT in Fig. 6 by showing in the left panels the time structure of $n_{\rm ph}(t)$, $n_{\rm x}(t)$, $V(t)$, and the single-k components $u_{k=0}(t)$ and $u_{k=\pi}(t)$ in the NESS of Fig. 4 at $\omega_0/J = 1.5$; juxtaposed in the right panels are the corresponding harmonic decompositions determined from Eq. (44). We have chosen a relatively conventional NESS trace [Fig. 6(c), similar to Fig. 4(c)], in which $n_{\rm x}(t)$ and $u_k(t)$ are dominated by the even Fourier components $m = 0$ and 2, while $V(t)$ [and by extension $v_k(t)$] is dominated by $m = 1$. This result is quite natural if one considers the equations of motion [Eqs. (41)], taking $q(t)$ to be a sinusoidal driving with small amplitude and a frequency ω_0. At leading order in $q(t)$, all components $v_k(t)$ and $w_k(t)$ will also oscillate at this same frequency, giving a dominant $m = 1$ component, while the leading-order response in $u_k(t)$ oscillates at $2\omega_0$ and possesses a constant offset (a zeroth harmonic). Because $n_{\rm x}(t)$ is the sum over all $u_k(t)$, it therefore shows harmonic components primarily at $m = 0$ and 2. All of these features are evident in Figs. 6(c)–6(j). In addition, we observe that the different k-components of $u_k(t)$ display different harmonic contributions, and because $\omega_0/J = 1.5$ excites triplons closer to the band minimum, the $m = 0$ and 2 coefficients are larger at $k = 0$ than at $k = \pi$; one may verify (data not shown) that the converse is true at a driving frequency of $\omega_0/J = 2.5$, and we consider the k-dependence of the response in more detail below.

Given this conventional behavior of the spin NESS, it is somewhat surprising to observe the presence of a significant $m = 1$ harmonic in the phonon NESS, $n_{\rm ph}(t)$, of Fig. 6(a). In fact $n_{\rm ph0}$ is suppressed by 14% compared to its $g = 0$ value (Fig. 2), which is a weaker version of the effect visible for the $\omega_0/J = 1.5$ phonon in Fig. 3(b). The presence of the $m = 1$ harmonic is another consequence of strong feedback from the spin system at this "resonant" (in-band) frequency, and arises from the term $g\mathcal{U}(t)p(t)$ in Eq. (38c), where $\mathcal{U}(t)$ oscillates primarily at $2\omega_0$ and $p(t)$ at ω_0. It is also clear that additional harmonics are present in the spin NESS analyzed in Fig. 6, including at higher multiples of ω_0, and one may anticipate [not least from Fig. 4(b)] that for certain frequencies they are significant.

To investigate the effect of the frequency of the driving phonon, in Fig. 7 we show the coefficients of $n_x(t)$ and $V(t)$ from $m = 0$ to 4 as a function of ω_0. Across the full range of frequencies, $n_{\rm x}(t)$ is indeed dominated by the $m = 0$ and 2 coefficients [Fig. 7(a)] and $V(t)$ by $m = 1$ [Fig. 7(b)], meaning that the case study of Fig. 6, performed for $\omega_0/J = 1.5$, is in fact well representative of the hierarchy of coefficient values, with only one significant exception. This is the frequency range around $\omega_0 = \omega_{\rm min}$, where a clear peak appears in a number of the harmonic components. Although frequencies

around $\omega_0/J = 0.7$ are far from a direct resonance, their second harmonic ($2\omega_0/J = 1.4J$) coincides with the peak density of states at the two-triplon band minimum. Inspection of Eqs. (41b) and (41c) reveals that oscillations are indeed induced at $2\omega_0$ because $q(t)$ is multiplied by $v_k(t)$ or $w_k(t)$. While this process appears at next-to-leading order in $q(t)$, it is strongly enhanced when the second harmonic satisfies the resonance condition.

The resonantly enhanced second harmonic of $w_k(t)$ in turn induces stronger first and third harmonic components in $u_k(t)$, as may be read from Eq. (41b), in which $w_k(t)$ is multiplied by $q(t)$ where it acts as a driving term for $u_k(t)$ at frequencies $(2 \pm 1)\omega_0$. This type of harmonic mixing results, for the driving we consider in Fig. 7, in the coefficient $|n_{x1}|$ even exceeding $|n_{x2}|$ around $\omega_0 = \omega_{\min}$, where $|n_{x3}|$ is also strongly enhanced. Similarly, $|V_2|$ and $|V_3|$ are also enhanced over a wide frequency range around $\omega_0 = \omega_{\min}$, where at its peak $|V_2|$ approaches $|V_1|$. Thus the resonant enhancement of the second harmonic explains why the temporal behavior of the spin NESS displays more and different features at below-band frequencies around $\omega_0/J = 0.5$ [Fig. 4(b)] than it does for the cases $\omega_0/J = 1.5$ [Figs. 4(c) and 6] and $\omega_0/J = 2.5$ [Fig. 4(d)].

We comment briefly on the physical meaning of the "frequency-doubling" effects that cause the enhancement of so many Fourier components around $\omega_0 = \omega_{\min}$. First, it is important to stress that the response observed at $2\omega_0$ in $n_x(t)$ is not a doubling phenomenon; it is merely a consequence of the fact that the triplon number is an operator square of the triplon degree of freedom, and in this sense the behavior of $u_k(t)$, $v_k(t)$, and $w_k(t)$ is directly analogous to that of the driven phonon variables discussed in Sec. III. By contrast, the frequency doubling observed between phonon driving at $\omega_0 = \omega_{\min}$ and the strong response of the spin system at $2\omega_{\min}$ is a real effect, which at a "classical" level can be read directly from the equations of motion. At a quantum level, this frequency doubling requires the involvement of two phonons at frequency ω_0, taking part in off-shell phonon-triplon processes that are allowed in the strongly out-of-equilibrium system.

We stress again that all physical processes of this type [meaning those contained in Eqs. (41)] do involve multiple driving phonons, as is standard in Floquet physics. Our treatment of the lattice system does not allow for the creation of phonons with frequencies of $2\omega_0$, $3\omega_0$, or higher due to anharmonicities in the lattice potential, as was discussed in Refs. [24,25]. Because the factors enhancing multiphonon response and harmonic mixing (Figs. 6 and 7) are the same, it is no surprise to find that both phenomena are strongest in the same range of frequencies. Quantitatively, the strength of these subdominant signals at constant a/γ is a product of powers of g with the height of the density-of-states peak at $2\omega_{\min}$, and the enhancement can exceed an order of magnitude at $\omega_0 = \omega_{\min}$.

Turning to the physical quantities characterizing the NESS, we have seen in Sec. III, and see again in Fig. 7, that the response of the spin system is very sensitively dependent on the driving frequency, with clearly different adiabatic, antiadiabatic, and "resonant" (by which is meant in-band) forms. However, some in-band frequencies are not particularly remarkable, due to small matrix elements or low densities of two-triplon states, and some adiabatic frequencies clearly have rather strong anomalous (multiphonon) enhancement. For a quantitative visualization of this response, in Fig. 8(a) we show the mean amplitude, n_{x0}, of the driven triplon occupation and in Fig. 8(b) the amplitude of the off-diagonal response, which we gauge using $|V_1|$. The rising lines indicate decreasing values of γ_s, which we terminate at $\gamma_s = 0.005J$ to avoid having n_{x0} exceed $n_x^{\max} = 0.2$, thereby allowing NESS formation at all frequencies for the chosen driving parameters. At frequencies far from a resonance with the edges of the band, n_{x0} is surprisingly insensitive to γ_s [Fig. 8(a)]. However, as ω_0 approaches $2\omega_{\min}$ and $2\omega_{\max}$, the driven n_{x0} varies strongly with γ_s, and the same is true around $\omega_0 = \omega_{\min}$.

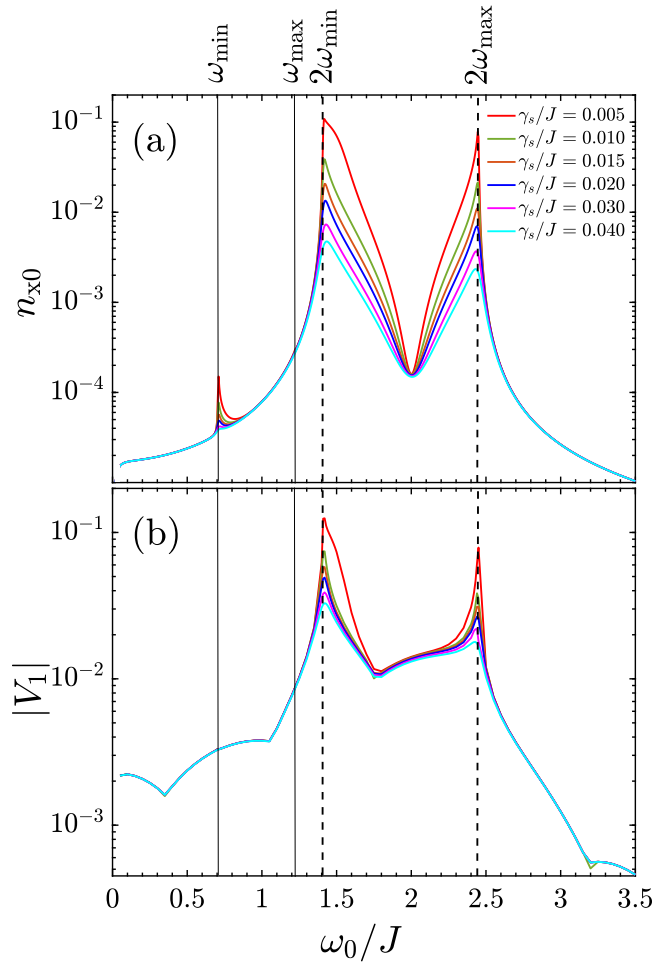

FIG. 8. (a) Average triplon occupation, n_{x0}, in the NESS obtained with driving $a/\gamma = 0.2$ and $g = 0.05$, shown on logarithmic axes as a function of ω_0 for different values of γ_s. The band-edge features become increasingly prominent as γ_s decreases, as does the peak at $\omega_0 = \omega_{\min}$, but for most other phonon frequencies n_{x0} is quite insensitive to the spin damping. (b) Corresponding off-diagonal response, shown by the quantity $|V_1|$.

As Fig. 8(b) makes clear, analogous effects are present at $\omega_0 = 2\omega_{\min}$ and $2\omega_{\max}$ in $|V_1|$, which also rises to values of order 0.1 at the lower band edge for $\gamma_s = 0.005J$ but is essentially independent of γ_s for driving frequencies more than $0.1J$ outside the two-triplon band. Because we have cho-

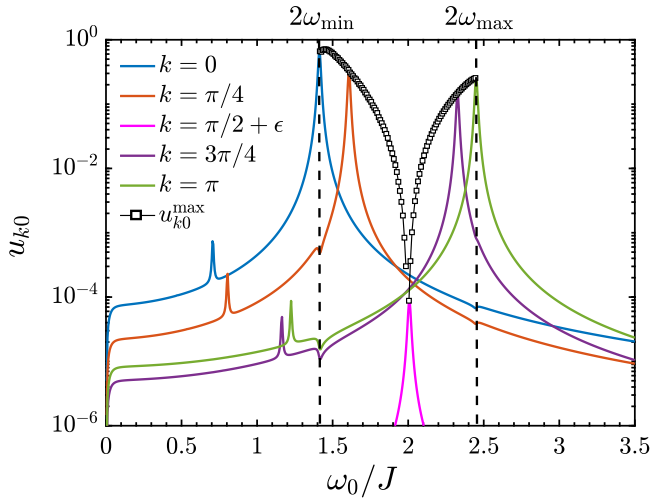

FIG. 9. Wave-vector-resolved average triplon occupation, u_{k0}, in the NESS obtained with driving $a/\gamma = 0.2$ and $g = 0.05J$, shown as a function of the driving frequency, ω_0, for $k = 0$, $\pi/4$, $\pi/2 + \epsilon$, $3\pi/4$, and π. Black squares show the maxima, $u_{k0}^{\max}$, of the u_{k0} functions peaking at different energies across the Brillouin zone, which defines the wave vectors $k_{\rm res}$. At all frequencies $\omega_0 < 2\omega_{\min}$ the strongest peak is found in $u_{k=0}$ and at $\omega_0 > 2\omega_{\max}$ in $u_{k=\pi}$. $\epsilon = \pi/N$ is an offset from the band center, where $u_{k=\pi/2} = 0$.

sen $|V_1|$ as the off-diagonal diagnostic, and this is a primary driving term in Eqs. (41) rather than a driven term, there is no γ_s-dependence around $\omega_0 = \omega_{\min}$; this response of the off-diagonal sector is found rather in the coefficients $|V_2|$ and $|V_3|$ in Fig. 7. The other differences in the frequencies of characteristic features in $|V_1|$, most notably the in-band minimum occurring at $\omega_0/J = 1.7$ rather than 2.0, may be traced to the leading dependence in Eq. (41b) on the coefficient y_k in Eq. (23a) as opposed to y'_k in Eq. (23b).

To understand the degree to which individual k-components of the spin system are selected by the phonon driving, in Fig. 9 we show u_{k0} over the full range of driving frequencies for selected values of k across the Brillouin zone. For $k = 0$ and π, it is no surprise that the respective u_{k0} functions peak strongly at $\omega_0 = 2\omega_{\min}$ and $2\omega_{\max}$, because these are the dominant available wave-vector components; we note that there is no problem with the fact that $u_{k=0}(t)$ exceeds the threshold when the system is driven at $\omega_0 = 2\omega_{\min}$, because the triplon occupation is determined by the average over all components [Eq. (30)]. For driving frequencies within the two-triplon band, one might expect a broad spin response on the grounds that triplon pairs from a wide range of wave vectors may contribute. However, the response at each frequency remains dominated by the resonance condition $\omega_0 = 2\omega_k$, and thus the components u_{k0} for $k = \pi/4$ and $3\pi/4$ continue to show sharp peaks (which fall by one order of magnitude over an energy range of 10% of the band width). Thus k-selection on the basis of the driving energy is rather accurate and it is well justified to introduce a "resonant" wave vector, $k_{\rm res}$, selected by each ω_0. The black squares in Fig. 9 show the maxima, $u_{k0}^{\max}$, of a sequence of $u_{k_{\rm res}}(t)$ functions selected in this way.

In addition to this characteristic frequency, each u_{k0} shows a pronounced below-band two-phonon process, visible at one half of the peak frequency, and it is only the act of averaging over all the k-components that disguises these features in our figures showing n_{x0}. For the driving and damping parameters used in Fig. 9, no three-phonon processes are discernible in the individual k-components. Nevertheless, a wealth of structure is revealed by considering the FT of the different k-components on logarithmic axes for a range of frequencies (analogies of Fig. 6, data not shown). The differential response of different k-components is also clearly visible when the drive is switched on, leading to complex envelope oscillations at initial times, and we will touch on these phenomena in Sec. V A. We remind the reader that the structure of our model ensures no interactions between triplons at different k, and so all $u_k(t)$ components evolve independently in time.

We close our discussion of dynamical phenomena in the NESS by commenting on the possibility of new dynamical modes emerging in the driven system, for example where the pumped phonon is strongly dressed by triplons. Excitations with combined phononic and spin character are known in a number of materials, including manganites and "spin-Peierls" chains. In general these are a property of the equilibrium system arising for strong g and, as noted at the end of Sec. III, their inclusion would require an extension of the present treatment. While this treatment does reveal unconventional dynamical processes in the driven system, specifically those involving multiple phonons, it is not designed to capture the formation of bound states of these excitations at equilibrium.

V. TRANSIENT AND RELAXATION PROCESSES

Although the primary aim of our present study is to discuss NESS themselves, clearly their short-time (transient) behavior on "start-up" is a key to measurement windows, as well as to analyzing switching processes of the type one may wish to use in logic operations. Despite the clear presence of the timescales set by the lattice and spin dampings, respectively $1/\gamma$ and $1/\gamma_s$, we have already observed in Figs. 4(a) and 4(c) that curiously slow convergence to a NESS can take place. To shed light on this result, we first analyze the convergence process and identify a further effective timescale arising from the driving. This allows us to illustrate the nature of convergence within the spin system, given the narrow resonance regimes of all the different k-components shown in Sec. IV. We then discuss the consequences of this relationship between driving and convergence for the possibilities, both theoretical and practical, that NESS may not be reached at all because the system is driven too strongly. Finally, the long-time behavior of the NESS in the absence of driving has both important benchmarking properties for theoretical purposes and a key role in thermal control for experimental implementations. As noted in Sec. II C, the formalism we derived there has no lower or upper cutoff in time, and thus can be applied to address every aspect of switching on and off a quantum spin NESS.

A. Transients at switch-on

In the introduction to NESS in our model (Sec. III), we showed in Figs. 2(a) and 2(b) how the phonon variables are "pumped up" on application of the electric field, with $n_{\rm ph}(t)$ approaching its steady state, and thus becoming a steady drive

for the spin system, after a time of approximately $4/\gamma$. In Fig. 4(a) we showed how the spin system reacts to this oscillatory driving, with $n_x(t)$ approaching its steady state after a time of approximately $4/\gamma_s$ at most of the driving frequencies in Fig. 4(a). However, it was clear from the $n_x(t)$ curve at $\omega_0/J = 1.5$, which took significantly longer to reach its NESS [Fig. 4(c)], that this reasoning alone does not explain every aspect of the spin response at the onset of driving.

For a quantitative analysis of the convergence timescale, we focus first on in-band driving ($2\omega_{\min} \leqslant \omega_0 \leqslant 2\omega_{\max}$) and consider the process by which $n_x(t)$ is "pumped up" by the driving phonon [Fig. 4(a)]. We simplify the analysis by using the fact that, in this range of ω_0, the driven phonon approaches its plateau of constant $n_{\text{ph}0}$ more quickly than the spin system, because $1/\gamma < 1/\gamma_s$. Thus we take the phonon oscillations as sinusoidal with a fixed amplitude [Fig. 2(c)], which to match the unit slope of Fig. 3 is given by

$$q(t) = 2\frac{a}{\gamma}\sin(\omega_0 t) \;=\; 2\frac{DJ}{g}\sin(\omega_0 t), \tag{45}$$

where we reintroduce the driving parameter, D [Eq. (42)], of the weak-coupling regime. For any selected k-value we define the function

$$f_k(t) = 4DJ\sin(\omega_0 t)y_k'[u_k(t) + 3/2], \tag{46}$$

which appears as an inhomogeneous term in the linear differential equation of Eq. (41c). We combine Eq. (41c) with Eq. (41b) by defining the variable $z_k(t) = v_k(t) + iw_k(t)$, which then obeys the inhomogeneous differential equation

$$\frac{dz_k}{dt} = 2i[\omega_k + 2DJ\sin(\omega_0 t)y_k]z_k - \gamma_s z_k + if_k(t). \tag{47}$$

A suitable primitive of the prefactor of the first term on the right-hand side is

$$h_k(t) = 2\int[\omega_k + 2DJy_k\sin(\omega_0 t)]\,dt \tag{48a}$$

$$= 2\omega_k t - \frac{4DJy_k}{\omega_0}\cos(\omega_0 t), \tag{48b}$$

allowing the solution of Eq. (47) to be expressed in the form

$$z_k(t) = ie^{ih_k(t)-\gamma_s t}\int_0^t f_k(t')e^{-ih_k(t')+\gamma_s t'}\,dt'. \tag{49}$$

This is not yet an explicit expression, because the right-hand side depends on $u_k(t)$, which remains unknown, but can be related to $z_k(t)$ by an expression based on Eq. (41a),

$$\tilde{u}_k(t) = u_k(t)e^{\gamma_s t} \tag{50a}$$

$$= -2iDJy_k'\int_0^t \sin(\omega_0 t')[z_k(t') - z_k^*(t')]e^{\gamma_s t'}\,dt', \tag{50b}$$

where $z^*(t')$ denotes the complex conjugate. While this general expression still does not represent an explicit function, it can be used to identify the primary trends in the response of the spin NESS.

We focus on the slowly varying component of $n_x(t)$, and not on the rapidly oscillating ones. For this it is sufficient to consider the slowly varying parts of each mode occupation, $u_k(t)$, as may be verified by numerical integration of Eqs. (41). Figure 9 indicates that the dominant term will be the one at the resonant momentum, k_{res}, which is determined from the driving frequency by $2\omega_{k_{\text{res}}} = \omega_0$. The behavior of k-components away from k_{res} is discussed in Appendix A and the results are summarized below. Henceforth we omit the subscript k_{res}. The slowly varying component of the right-hand side of Eq. (49) is obtained by averaging over one period, $T_0 = 2\pi/\omega_0$, giving

$$\frac{1}{T_0}\int_0^{T_0}\sin(\omega_0 t)e^{-ih(t)}dt = J_1(\beta)/\beta, \tag{51}$$

in which $\beta = 4DJy/\omega_0$ and $J_1(\beta)$ is the Bessel function of the first kind. Replacing $\sin(\omega_0 t')\exp[-ih(t')]$ in the integrand of Eq. (49) by its average taken from Eq. (51) leads to

$$z(t) = i\frac{y'}{y}\omega_0 J_1(\beta)e^{ih(t)-\gamma_s t}F(t) \tag{52a}$$

with

$$F(t) = \int_0^t\left[\tilde{u}(t') + \frac{3}{2}e^{\gamma_s t'}\right]dt', \tag{52b}$$

which is a real quantity. We stress that the approximations leading to this result are well justified because the driving oscillations are much faster than the build-up in the triplon expectation values [Fig. 4(a)]. By inserting Eq. (52a) into Eq. (50b) we obtain

$$\tilde{u}(t) = \frac{(2y')^2 DJ\omega_0 J_1(\beta)}{y}\text{Re}\left[\int_0^t \sin(\omega_0 t')e^{ih(t')}F(t')\,dt'\right] \tag{53a}$$

$$= \left[\frac{y'\omega_0 J_1(\beta)}{y}\right]^2\int_0^t F(t')\,dt', \tag{53b}$$

where again we have used Eq. (51) to obtain the last expression. Taking the second derivative yields

$$\frac{d^2\tilde{u}}{dt^2} = \Gamma^2\left[\tilde{u}(t) + \frac{3}{2}e^{\gamma_s t}\right], \tag{54}$$

in which we have defined

$$\Gamma = \left|\frac{y'\omega_0}{y}J_1\left(\frac{4DJy}{\omega_0}\right)\right|. \tag{55}$$

The differential equation is readily solved with the relevant initial conditions, $\tilde{u}(0) = 0$ and $d\tilde{u}/dt(0) = 0$, to give the final expression for $u(t)$ as

$$u(t) = \frac{3\Gamma}{4}\left(\frac{1 - e^{-(\gamma_s-\Gamma)t}}{\gamma_s - \Gamma} - \frac{1 - e^{-(\gamma_s+\Gamma)t}}{\gamma_s + \Gamma}\right). \tag{56}$$

This result makes the essential feature clear immediately. At the level of the present analysis, the true convergence rate is given by the quantity

$$\tilde{\gamma}_s = \gamma_s - \Gamma, \tag{57}$$

which can become arbitrarily small when Γ approaches γ_s. The qualitative situation is quite intuitive: γ_s decribes the rate of relaxation of the system back to a state with zero triplons at zero temperature, which is the case considered here (and discussed in Sec. V C); the phonon driving acts in the opposite direction by creating pairs of triplons, and thus strong driving changes the effective relaxation (damping) timescale. In fact it

is clear that Eq. (57) also specifies a regime where Γ exceeds γ_s, so that triplon creation outweighs the relaxation term and Eq. (56) specifies that the resonant triplon occupation, $u(t)$, will undergo an exponential divergence. This situation will be the focus of our attention in Sec. V B. Quantitatively, in most circumstances the argument of J_1 will be non-negative and smaller than 1.84, which is where the function has its first maximum. In this interval, J_1 is a monotonically increasing function of the driving strength, D, and thus one expects that Γ can indeed be raised to values on the order of γ_s.

Before computing Γ as a function of ω_0, we make two further general remarks. First, in the qualitative view of Γ as a driving rate, or excitation rate, that competes with the relaxation rate, γ_s, one is tempted to interpret Γ in terms of Fermi's Golden Rule. However, a conventional application of the Golden Rule gives a rate proportional to the square of the matrix element, whereas in the present analysis $\Gamma = 2DJy'$ at small driving ($D \to 0$), meaning that Γ is linearly proportional to the driving amplitude. In more detail, the value of $u(t)$ in the NESS is given from the long-time limit of Eq. (56) by $3\Gamma^2/[2(\gamma_s^2 - \Gamma^2)]$ and thus is indeed proportional to Γ^2, and hence to D^2, in accordance with the Golden Rule. However, the timescale of the transient behavior as the system approaches the NESS is governed by a different coherent mechanism that yields $\Gamma \propto D$.

Second, for quantitative purposes it is necessary to consider the effect of driving at frequency ω_0 on the modes at $k \neq k_{\rm res}$, meaning the action of the driving phonon as a "detuned" pump of all other triplon modes. The algebra of the detuned case is presented in Appendix A and we summarize the results as follows. As a function of a detuning parameter we define as

$$\delta = 2\omega - \omega_0, \tag{58}$$

there are two possible regimes. If $|\delta| < \Gamma$, it is convenient to define the quantity

$$\widetilde{\Gamma} = \sqrt{\Gamma^2 - \delta^2}, \tag{59}$$

in terms of which

$$u(t) = \frac{3\Gamma^2}{2\left(\gamma_s^2 - \widetilde{\Gamma}^2\right)}\left\{1 - e^{-\gamma_s t}\left[\cosh(\widetilde{\Gamma}t) + \frac{\gamma_s}{\widetilde{\Gamma}}\sinh(\widetilde{\Gamma}t)\right]\right\}. \tag{60}$$

Thus from the behavior of the hyperbolic function, $\widetilde{\Gamma}$ adopts the role of Γ in Eq. (57) and the relevant convergence rate becomes $\tilde{\gamma}_s = \gamma_s - \widetilde{\Gamma}$. By contrast, when $|\delta| > \Gamma$, so that the detuning of the driving frequency exceeds the driving threshold, it is convenient to define the quantity

$$\tilde{\delta} = \sqrt{\delta^2 - \Gamma^2}, \tag{61}$$

in terms of which

$$u(t) = \frac{3\Gamma^2}{2\left(\gamma_s^2 + \tilde{\delta}^2\right)}\left\{1 - e^{-\gamma_s t}\left[\cos(\tilde{\delta}t) + \frac{\gamma_s}{\tilde{\delta}}\sin(\tilde{\delta}t)\right]\right\}. \tag{62}$$

Because all the hyperbolic functions become trigonometric, the sole remaining exponential convergence is governed by γ_s, leading to the result that the convergence is conventional. We note in this case that slow oscillations arise at frequency $\tilde{\delta}$, which may cause the triplon number to overshoot before it converges to its NESS limit (example data not shown).

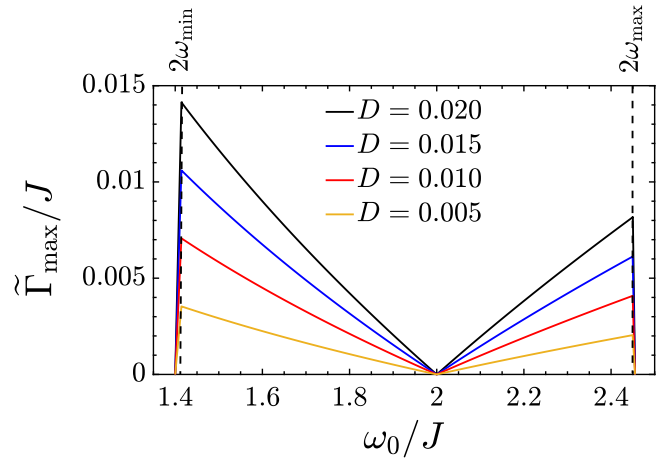

FIG. 10. Dependence of the inverse driving timescale, $\widetilde{\Gamma}_{\rm max}$, on the frequency, ω_0, of the driving phonon, shown for four values of the driving strength, D.

Although one might assume that the resonant case, $2\omega_k = \omega_0$, described by Eq. (56) will provide the highest threshold value, making $\widetilde{\Gamma}_{\rm max} = \Gamma$, the complicated dependence of Γ on k [Eq. (55)] makes it possible that, for a given ω_0, a slightly detuned mode at $k \neq k_{\rm res}$ yields a higher $\widetilde{\Gamma}$. In particular, for frequencies close to but outside the two-triplon band, detuned driving will be of primary importance. To capture these possible effects, we compute $\widetilde{\Gamma}_{\rm max}$ by variation of k at each fixed ω_0, and the results are shown in Fig. 10.

Clearly $\widetilde{\Gamma}_{\rm max}$ is finite throughout the in-band regime, although it drops to zero at the band center ($\omega_0 = 2J$) due to a matrix-element effect ($y'_k|_{k=\pi/2} = 0$). Although the dependence of $\widetilde{\Gamma}_{\rm max}$ on ω_0 is both direct and indirect, occurring both through proximity to the resonance condition ($2\omega_{k_{\rm res}} = \omega_0$) and through the momentum dependence of y_k and y'_k, it shows an almost linear rise with frequency towards the two band edges. Because we consider the linear driving regime of Sec. III, it is also a linear function of D. Importantly, $\widetilde{\Gamma}_{\rm max}$ is also finite outside the two-triplon band as a consequence of detuned driving, although for the parameters in Fig. 10 it falls rapidly (in fact over a frequency window of order DJ) beyond the band edges. For any given D, the function $\widetilde{\Gamma}_{\rm max}(\omega_0)$ indicates the values of the triplon damping, γ_s, for which unconventional convergence can occur, and it is no surprise to find that in-band frequencies near the two band edges are the most likely candidates [Fig. 4(a)]. From Fig. 10, and specifically from the value of $\widetilde{\Gamma}_{\rm max}$ at $\omega_0 = 2\omega_{\rm min}$, one may read that, at the level of our analysis, the value of γ_s ensuring conventional or slow convergence at all frequencies for driving $D = 0.01$ (Sec. IV) is approximately 0.007. We comment on the minor discrepancy with our numerical findings in Fig. 8, where NESS formation was verified at all ω_0 with $\gamma_s = 0.005$, in Sec. V B.

Here we make three quantitative side remarks to this analysis. First, the effective driving timescale, $\widetilde{\Gamma}_{\rm max}$, is not easily read from the external driving parameters, because it depends crucially on the phonon amplitude. Even in the weak-coupling

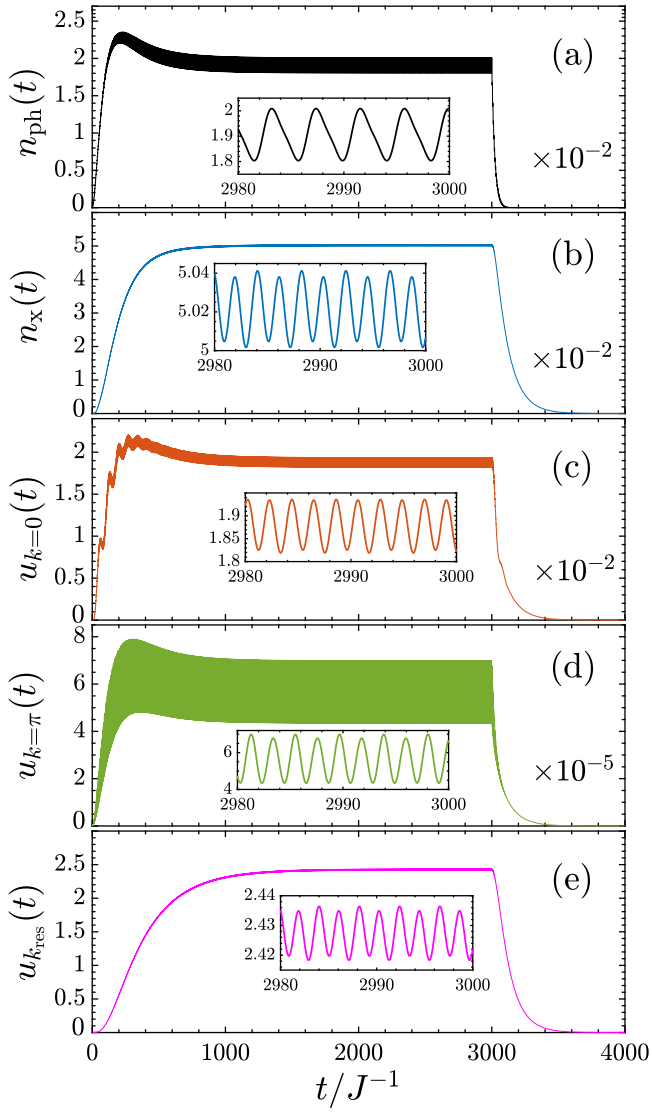

FIG. 11. Creation of the NESS established with $a/\gamma = 0.2$ and $g = 0.1J$ (driving parameter $D = 0.02$) for driving frequency $\omega_0/J = 1.5$ and spin damping $\gamma_{\rm s} = 0.01J$; these are the parameters of the green line in Fig. 4(a). (a) $n_{\rm ph}(t)$. (b) $n_{\rm x}(t)$. (c) $u_{k=0}$. (d) $u_{k=\pi}$. (e) $u_{k_{\rm res}}$. Also shown is the relaxation of each variable when the driving is removed after 3000 time steps.

regime, meaning small g as defined in Sec. III, we have seen that the oscillations of the driven phonon are not entirely independent of the spin system for in-band driving frequencies. Second, we do not consider the additional complexity of a k-dependent $\gamma_{\rm s}$, although the framework developed here could be used without alteration. Third, the effect of nonlinear processes occurring at multiples of ω_0, is not included in our discussion of Γ and $\widetilde{\Gamma}$, although it could be incorporated by considering a very weak effective D.

To illustrate the phenomenon of slow convergence at switch-on, we consider driving field $a/\gamma = 0.2$ and $g = 0.1J$, which is the situation in Fig. 4(a). For the in-band driving frequency $\omega_0 = 1.5J$ and spin damping $\gamma_{\rm s} = 0.01J$, we show in Figs. 11(a) and 11(b) the driven phonon and triplon numbers. The driving strength is the same as that in Fig. 2(a), and thus $n_{\rm ph}(t)$ first rises towards the plateau value of 0.04 in a time dictated by $1/\gamma$, but is pulled down again to an average value $n_{\rm ph0} \simeq 0.02$ [Fig. 3(b)] in a time dictated by $1/\tilde{\gamma}_{\rm s}$. This is a direct reflection of the "inertia" of the spin system as it begins to absorb some of the input phonon energy, a topic we analyze in more detail in Sec. VI A. The values of $\gamma_{\rm s}$ and $\widetilde{\Gamma}$ (Fig. 10) place the system very close to the threshold specified by Eq. (57), with the result that the spin NESS [Fig. 11(b)] is reached only after approximately 1200 time steps [Fig. 4(c)], indicating that $1/\tilde{\gamma}_{\rm s} \approx 3/\gamma_{\rm s}$. For a more quantitative understanding of the transient phenomena in this regime, in Figs. 11(c) to 11(e) we show the $k = 0$-, π-, and $k_{\rm res}$-components of $u_k(t)$. It is not a surprise to confirm that the majority of the slow-convergence behavior is indeed concentrated in $u_{k_{\rm res}}(t)$ [Fig. 11(e)], which is both the largest and the most slowly converging component, apparently requiring 50% longer than $n_{\rm x0}(t)$ to converge within 2% of its final value. However, it is somewhat surprising to find that the nonresonant $u_k(t)$ components actually rise above their NESS values (on a timescale dictated by $\gamma_{\rm s}$) before falling again as the driving phonon amplitude reaches its final NESS value [on the timescale dictated by $u_{k_{\rm res}}(t)$].

B. Existence of NESS

In Secs. III, IV, and V A, we have used parameters allowing the formation of NESS in order to analyze their response to the driving parameters and their internal dynamical properties. Having established this foundation, we now discuss the crucial issue of whether a NESS can exist at all for strong driving over long driving times. Clearly, unlimited driving would lead to heating of the system on a finite timescale, and we defer a discussion of this topic until Sec. VI; here we continue to assume that the heat sink represented in Fig. 1 maintains a steady, low system temperature despite the injection of energy from the laser. The focus of our present discussion is the possibility that the lattice or spin system could be driven so strongly that it breaks down rather than converge to a NESS.

The integrity of the driven lattice is easy to establish. A straightforward application of the Lindemann criterion, whose details we present in Appendix B, leads to the result that lattice melting due to phonon driving would become an issue for average phonon mode occupancies on the order of $n_{\rm ph0} = 3$. Thus the driving parameters we consider here, and the resultant $n_{\rm ph0}$ values, pose no threat to the periodic lattice. By contrast, based on the discussion of Sec. V A, one might expect that Eq. (57) represents a threshold of driving strength (D) beyond which triplon creation exceeds their relaxation and $n_{\rm x}$ should diverge exponentially, meaning that NESS formation is impossible. Here we discuss two criteria for the loss of NESS. The first is breaching of the condition on the triplon occupation, $n_{\rm x}(t) < n_{\rm x}^{\rm max} = 0.2$ (Sec. III), beyond which the formalism of Sec. II can no longer be applied to the spin system. The second is breaching of the positivity of $\tilde{\gamma}_{\rm s}$ as defined in Eq. (57).

Considering first the maximum triplon occupation, in Fig. 12 we show the threshold value of the driving strength, $(a/\gamma)_{\rm t}$, required to drive the triplon occupation of the spin NESS above $n_{\rm x}^{\rm max}$. Red colors are chosen to represent regions of small $(a/\gamma)_{\rm t}$, because this indicates efficient triplon

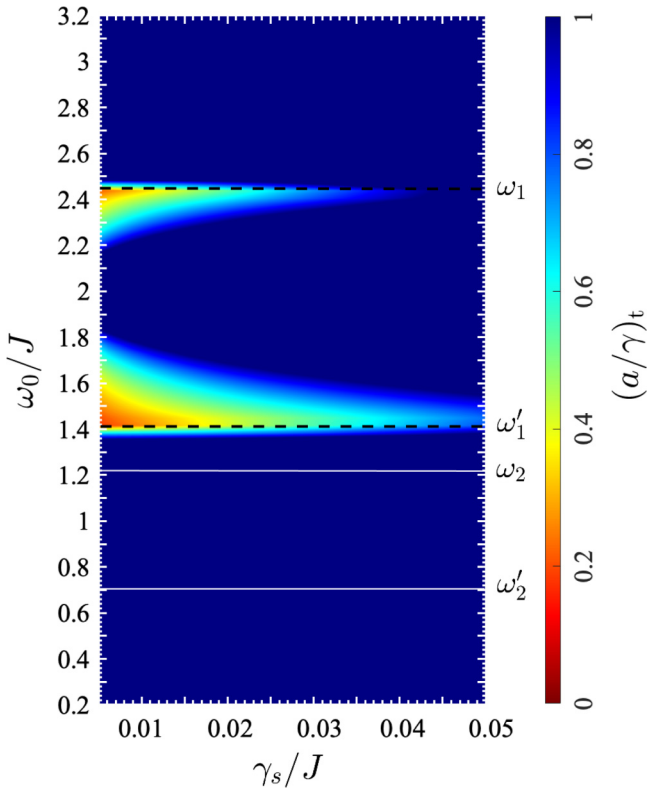

FIG. 12. Threshold value, $(a/\gamma)_t$, of the normalized laser electric field strength required to achieve the maximum steady-state triplon occupation of $n_x = 0.2$, shown as a function of γ_s and ω_0 for fixed $g = 0.05J$ and $\gamma = 0.02\omega_0$. We draw attention to the 3 regimes of behavior demarcated by $\omega_1' = 2\omega_{min}$ and $\omega_1 = 2\omega_{max}$. Also marked are the frequencies $\omega_2' = \omega_{min}$ and $\omega_2 = \omega_{max}$, where unlike Fig. 8(a) no additional structure is visible in $(a/\gamma)_t$.

occupation, and these are found at driving frequencies corresponding to the lower and upper edges of the two-triplon band, intensifying as γ_s becomes smaller (Sec. IV). As in Fig. 8(a), it is evident that the system does not respond as efficiently for in-band frequencies near the band center, and that very strong driving is required when ω_0 lies above the two-triplon band. In contrast to Fig. 8(a), $(a/\gamma)_t$ does not reflect the presence of the two-phonon response feature at and above $\omega_0 = \omega_{min}$, underlining that the n_{x0} values arising due to these processes are indeed small.

Nevertheless, one may worry that $n_x^{max} = 0.2$ is an arbitrary criterion, which would have no relevance if a more sophisticated treatment of the spin sector were implemented, and thus that the driving criterion should give a more rigorous statement on the existence of NESS. However, here we encounter departures from the idealized analytical discussion of Sec. V A. There we also remarked on the observation in our numerical results that the driven phonon does not reach the average occupation, n_{ph0}, expected from Fig. 3(a) because of the effects of the spin system that it drives. While this result was visible at $g = 0.1J$ for the $\omega_0/J = 1.5$ phonon in Fig. 3(b), it is not absent in what we have called the weak-g regime, as one may observe from the value of n_{ph0} in Fig. 6(a). This is one example of a feedback effect between the lattice and spin systems, which we will encounter again in Sec. VI A. Its consequence for the analysis in Sec. V A is that one may no longer assume a fixed driving strength, D, but because of this downwards renormalization one should work with an effective driving, D_{eff}. The deviation between D and D_{eff} becomes larger as D is increased. We have also encountered strong feedback effects as γ_s becomes very small and as n_{ph0} becomes large enough to alter the dimerization, λ, of the spin system. What all of these feedback effects have in common is that they are significant only when the triplon occupation is large, meaning $n_x > n_x^{max}$, and thus the constraint $n_x^{max} = 0.2$ adopts additional significance. Feedback is a complex topic that will be important in discussing driven systems with strong g, but lies beyond the scope of our current exposition.

Even without a driving criterion, it is nonetheless instructive to ask how the breakdown of NESS occurs. We perform only a brief and numerical examination of how the model of Sec. II behaves when NESS formation is precluded, for which we set $\gamma_s = 0$. In Fig. 13 we depict the time-evolution of the lattice and spin systems for different driving frequencies with a fixed driving strength, $D = 0.01$. For in-band driving at $\omega_0/J = 1.5$ and a spin damping $\gamma_s = 0.01J$, Fig. 13(a) shows the NESS of Fig. 6. However, when $\gamma_s = 0$, Fig. 13(b) shows how the triplon number is driven rapidly to a regime well beyond n_x^{max}, which in turn causes the phonon occupation to become unstable and creates complex, aperiodic feedback phenomena.

When ω_0 lies above the two-triplon band, one may read from the detuning discussion, and also directly from Fig. 12, that two possibilities exist. If ω_0 is sufficiently far beyond $2\omega_{max}$, as shown in Fig. 13(c) for the case $\omega_0/J = 3.0$, a NESS can be formed even with $\gamma_s = 0$. In this case, the phonon driving cannot cause the direct occupation of triplons and the steadily driven state of the spin sector remains only very weakly excited. Any feedback from the spin to the lattice sector under these circumstances is negligible, and thus the latter is also unaffected by the value of g. The beating envelope in $n_x(t)$ in Fig. 13(c) is a consequence of transient signals in individual components of $u_k(t)$ that are never damped with $\gamma_s = 0$. The second possibility arises when ω_0 lies above but very close to $2\omega_{max}$, in which case the driving phonon acts as a detuned pump of the spin response at the upper band edge and the physics is that of Figs. 13(a) and 13(b).

Finally, the situation for driving frequencies below the lower two-triplon band edge is somewhat more complicated. Once again there is a regime of potentially divergent behavior due to detuned driving when ω_0 lies slightly below $2\omega_{min}$ (Fig. 12). [This phenomenon also allows one to understand why the lower and upper two-triplon band edges do not create extremely sharp features, or even discontinuities, as a function of ω_0 in the response observed in Figs. 7 and 8.] At frequencies below the detuned regime, the generic situation is that illustrated in Fig. 13(d) for a frequency $\omega_0 = 0.75J$. The phonon does indeed approach a NESS, but this essentially steady driving does not create a spin NESS because high-order processes always exist that pump the undamped spin system on some potentially very long timescale. In Fig. 13(d) the higher-order process involves the second harmonic, and it is necessary both to follow the spin dynamics to multiples of 10^4 time steps and to use long chains (here $N = 3000$) to verify the situation. In general, driving of the system by a

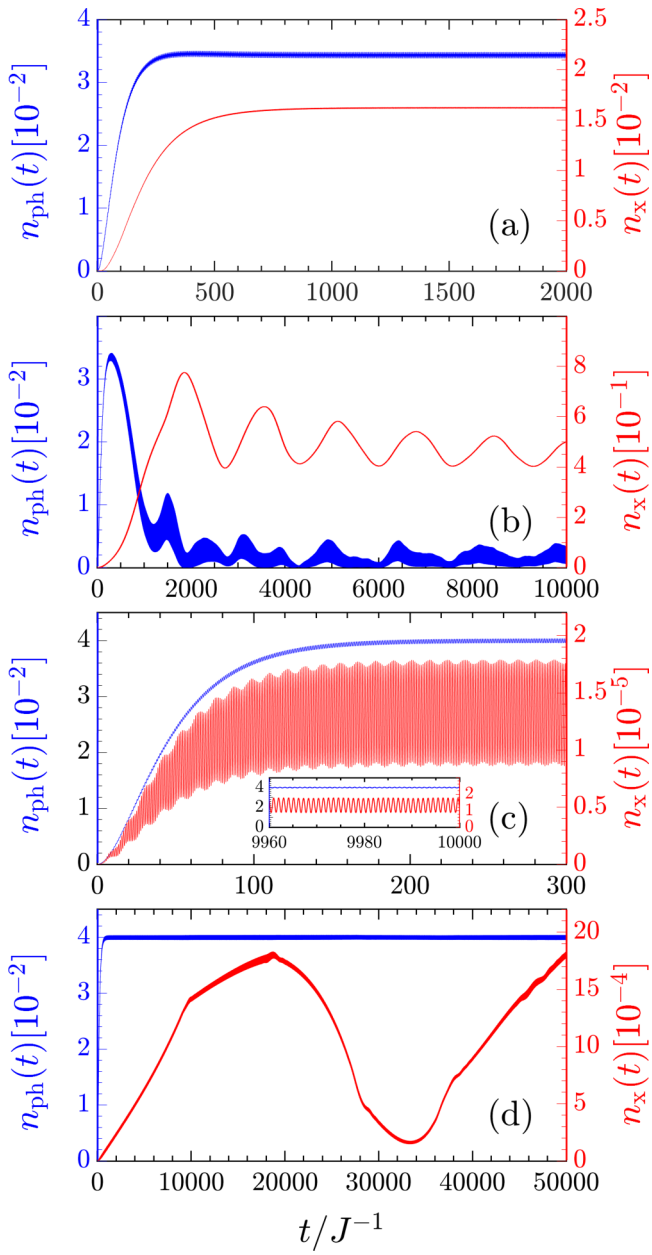

FIG. 13. Time dependence of the phonon number, $n_{\rm ph}(t)$, and triplon number, $n_{\rm x}(t)$, shown with $a/\gamma = 0.2$ and $g = 0.05J$ ($D = 0.01$). (a) When $\omega_0/J = 1.5$ and $\gamma_{\rm s} = 0.01J$ (the parameters of Fig. 6), the system converges to a NESS on a conventional timescale. (b) When $\omega_0/J = 1.5$ and $\gamma_{\rm s} = 0$, $n_{\rm x}(t)$ increases rapidly beyond $n_{\rm x}^{\rm max}$, destabilizing the phonon occupation. (c) When $\omega_0/J = 3.0$, the driving frequency lies sufficiently far above the two-triplon band that NESS exist even when $\gamma_{\rm s} = 0$. (d) When $\omega_0/J = 0.75$, the driving frequency lies well below the two-triplon band but the second harmonic, $2\omega_0$, lies within it. In this case, when $\gamma_{\rm s} = 0$ the lattice approximates a NESS, but with this near-constant driving of the spin system a NESS cannot be formed.

multiphonon process can be captured by the same analytical arguments applied for in-band frequencies, although the effective value of D should be replaced by the amplitude of the relevant higher harmonic. As a result, the qualitative situation at arbitrary below-band frequencies is that of Fig. 13(d), but quantitatively the required timescale may extend to millions of steps. We conclude this analysis by stressing again that NESS formation is the most natural behavior in the model of Fig. 1 at all frequencies for realistic values of a and $\gamma_{\rm s}$, as shown in Fig. 13(a), as well as throughout Sec. III.

C. Relaxation at switch-off

The process of relaxation of a system with Lindblad damping is the recovery of thermal equilibrium in the absence of the drive. In our analysis, the system started at temperature $T = 0$ before the drive was switched on, and thus it relaxes back to this state. The present analysis is readily extended to finite T by including (1) a thermal phonon occupation, (2) a more sophisticated treatment of the spin system [92], and (3) the thermal factors in the definition of the bath properties that are already contained in the Lindblad formalism (Sec. II C). However, this extension would not account for the fact that the driving introduces energy to the system, and hence causes heating; for this we appeal to the heat sink represented in Fig. 1, which corresponds to the cooling apparatus in any condensed-matter experiment. We will discuss the issues associated with the system temperature, particularly in the presence of the laser drive, more deeply in Secs. VI and VII.

For the purposes of this subsection, in Fig. 11 we have switched off the phonon drive after 3000 time steps. It is clearly visible in all cases that the phonon sector [characterized by $n_{\rm ph}(t)$] relaxes to its equilibrium, $n_{\rm ph} = 0$, over a timescale governed by $1/\gamma$ and the spin sector [characterized by $n_{\rm x}(t)$] over a timescale governed by $1/\gamma_{\rm s}$. This behavior is independent of the value of ω_0 at which the system was being driven and of the amplitude of the driving (data not shown). In this sense, relaxation can be considered as similar to the process of "pumping up" the NESS with a very low drive, so that the system remains far from the driving-induced timescale obtained in Sec. V A. Thus one may conclude that unconventional transient processes appear only when the system is driven, and indeed driven near its band edges, whereas relaxation dynamics are straightforward.

VI. ENERGY FLOW AND SYSTEM HEATING

A. Energy flow

Particularly valuable for both conceptual and practical purposes is to consider the energy flow through the spin-lattice system. For a true NESS, the rate of energy throughput should be constant from the driving to the final stage of dissipation. Figure 14 provides a schematic representation of the situation, which we characterize using seven separate stages of the flow process. The energy flow (energy per unit time) is a power and is defined to be positive in the direction of the arrows in Fig. 14. Clearly the input power is the uptake of laser energy by the driven phonon, part of which also drives the spin sector through the effect of the spin-phonon coupling. Energy absorption by the lattice, which is also the bath, will determine the temperature of the system; while this is limited by possible melting of the crystal, the loss of coherence in the quantum spin states is a much more stringent criterion. To avoid a monotonic rise in the lattice, or bath, temperature, we

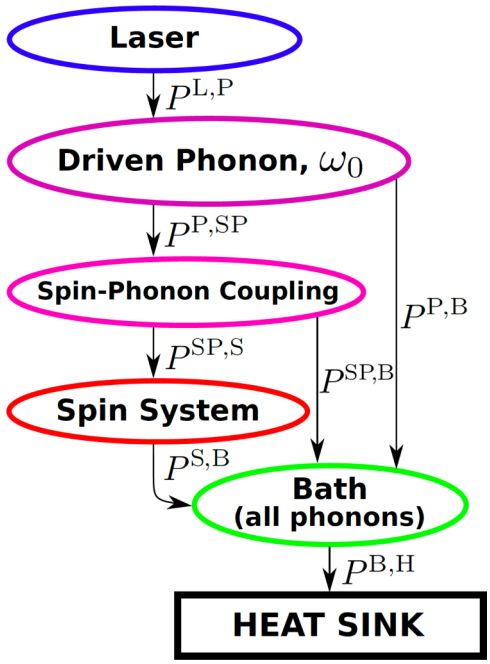

FIG. 14. Schematic representation of energy flow into and out of the NESS of the combined lattice and spin system.

model the system as being connected to a large and efficiently conducting heat sink.

To compute the different energy flows in Fig. 14, the following two relations may be read directly from the differential equation of Eq. (38c), which describes the time evolution of the number of energy quanta in the driven phonon. The energy flow from the laser into this phonon, normalized to the number of dimers, is given by

$$P^{\mathrm{L,P}}(t) = -E(t)\omega_0 p(t), \tag{63}$$

while the energy flowing from it and directly to the bath is given by

$$P^{\mathrm{P,B}}(t) = \gamma\omega_0[n_{\mathrm{ph}}(t) - n(\omega_0)]. \tag{64}$$

The energy flowing out of the driven phonon due to the presence of the spin-phonon coupling is given by using the same equation to obtain

$$P^{\mathrm{P,SP}}(t) = g\omega_0[\mathcal{U}(t) + \mathcal{V}(t)]p(t). \tag{65}$$

By considering energy conservation for the phonon we obtain the sum rule

$$P_0^{\mathrm{L,P}} = P_0^{\mathrm{P,SP}} + P_0^{\mathrm{P,B}} \tag{66}$$

for the temporal averages of each power. We remark that all of the powers in Fig. 14 have a temporal oscillation in the NESS at multiples of the driving frequency, in the same way as all the other quantities discussed in Secs. III and IV. However, these oscillations are not very relevant to the overall energy flow or system temperature and we focus on their average values, which are the $m = 0$ harmonics of Sec. IV, so we denote them by $P_0^{\mathrm{X,Y}}$.

Turning to the spin sector, Eq. (41a) gives the energy flow into the spin system as

$$P^{\mathrm{SP,S}}(t) = 2gq(t)\frac{1}{N}\sum_k y_k'\omega_k w_k(t). \tag{67}$$

The same equation also states that the energy flow from the spin system into the bath is given by the decay rate of all the triplons, which yields

$$P^{\mathrm{S,B}}(t) = \frac{\gamma_{\mathrm{s}}}{N}\sum_k \omega_k[u_k(t) - 3n(\omega_k)]. \tag{68}$$

Once again, energy conservation within the spin system enforces the sum rule

$$P_0^{\mathrm{SP,S}} = P_0^{\mathrm{S,B}} \tag{69}$$

on the time-averaged values. However, if one considers Eq. (65) as the work done by the phonon on the spin system and Eq. (67) as the work received by the spin system due to the phonon, it is evident that there is no mathematical reason for these two quantities to be equal. To obtain the physical sum rule, it is necessary to consider in detail the spin-phonon coupling term, H_{sp} in Eqs. (1) and (21a). In the mean-field approximation, we have by construction

$$\frac{1}{N}\langle H_{\mathrm{sp}}\rangle(t) = gq(t)(\mathcal{U} + \mathcal{V})(t), \tag{70}$$

and hence the time derivative

$$\frac{1}{N}\partial_t\langle H_{\mathrm{sp}}\rangle = g[(\partial_t q)(\mathcal{U} + \mathcal{V}) + q\partial_t(\mathcal{U} + \mathcal{V})]. \tag{71}$$

Using Eqs. (38a), (41a), and (41b) to evaluate the partial derivatives on the right-hand side yields

$$\frac{1}{N}\partial_t\langle H_{\mathrm{sp}}\rangle = g\omega_0(\mathcal{U} + \mathcal{V})p - \frac{1}{2}g\gamma q(\mathcal{U} + \mathcal{V}) \tag{72a}$$

$$+ gq\frac{1}{N}\sum_k y_k\{2gqy_k'w_k - \gamma_{\mathrm{s}}[u_k - 3n(\omega_k)]\} \tag{72b}$$

$$-gq\frac{1}{N}\sum_k y_k'[2(gqy_k + \omega_k)w_k + \gamma_{\mathrm{s}}v_k]. \tag{72c}$$

By inspection, the first term in Eq. (72a) is $P^{\mathrm{P,SP}}(t)$ and the second term in Eq. (72c) is $P^{\mathrm{SP,S}}(t)$, while the first terms in Eqs. (72b) and (72c) cancel, as a result of which the expression takes the form

$$\frac{1}{N}\partial_t\langle H_{\mathrm{sp}}\rangle = P^{\mathrm{P,SP}}(t) - P^{\mathrm{SP,S}}(t) \tag{73a}$$

$$-gq(t)\left(\frac{1}{2}\gamma + \gamma_{\mathrm{s}}\right)(\mathcal{U} + \mathcal{V})(t). \tag{73b}$$

The second line suggests rather strongly the definition

$$P^{\mathrm{SP,B}}(t) = gq(t)\left(\tfrac{1}{2}\gamma + \gamma_{\mathrm{s}}\right)(\mathcal{U} + \mathcal{V})(t) \tag{74a}$$

$$= \left(\tfrac{1}{2}\gamma + \gamma_{\mathrm{s}}\right)\langle H_{\mathrm{sp}}\rangle(t), \tag{74b}$$

where $-P^{\mathrm{SP,B}}(t)$ describes a relaxation of $\langle H_{\mathrm{sp}}\rangle(t)$ towards zero. This quantity corresponds to a flow of energy from

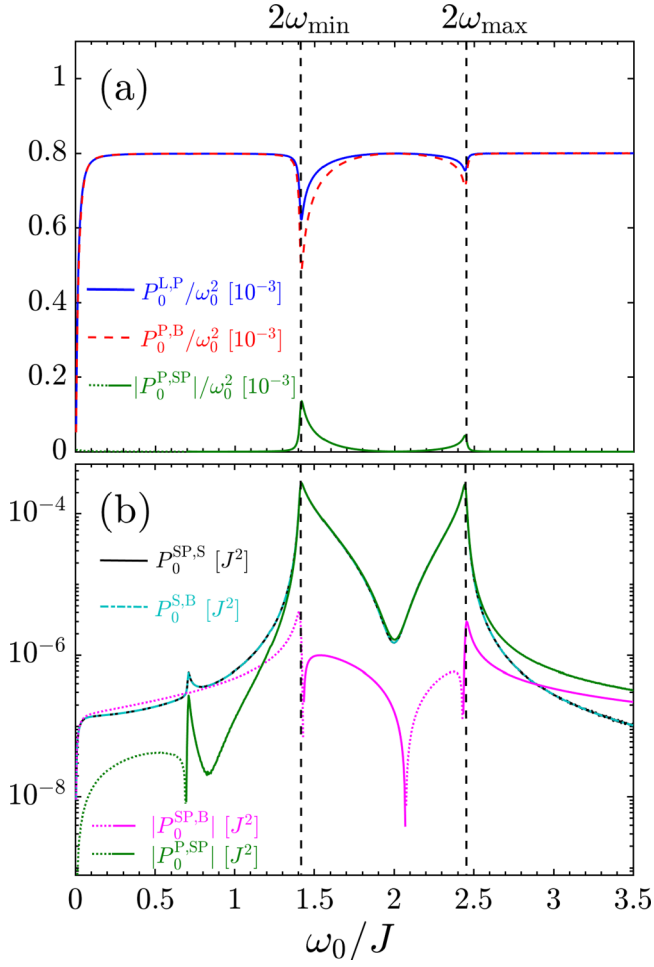

FIG. 15. Average energy flows, $P_0^{\rm X,Y}$, through the combined lattice and spin system depicted in Fig. 14, normalized to the number of dimers and shown as a function of ω_0 for $\gamma = 0.02J$, $a/\gamma = 0.2$, $g = 0.05J$, and $\gamma_{\rm s} = 0.01J$. (a) Power delivered to the driving phonon ($P_0^{\rm L,P}$) and power dissipated directly to the bath from this phonon ($P_0^{\rm P,B}$), whose difference is the power transferred towards the spin system from this phonon ($P_0^{\rm P,SP}$). For clarity we show $P_0^{\rm X,Y}$ normalized by ω_0^2. (b) Work done by the phonon system due to the spin system ($P_0^{\rm P,SP}$) and power delivered to the spin system ($P_0^{\rm SP,S}$), with their difference ($P_0^{\rm P,SP}$) represented on the logarithmic scale as a modulus with a solid (dashed) line for a positive (negative) power. $P_0^{\rm SP,S}$ is identically equal to the power dissipated by the effect of the bath on the spin system ($P_0^{\rm S,B}$).

the spin-phonon coupling towards the bath and its temporal average completes the balance

$$P_0^{\rm P,SP} = P_0^{\rm SP,S} + P_0^{\rm SP,B}, \tag{75}$$

which results from the fact that the time-average of the derivative $\partial_t \langle H_{\rm sp}\rangle$ must vanish in a NESS. Thus the definition of Eq. (74a) and the additional sum rule of Eq. (75) provide the appropriate linkage to describe energy conservation in the coupled spin-phonon system.

In Fig. 15 we show how the energy flows of Eqs. (63)–(65), (67), (68), and (74a) depend on the driving frequency. All of the powers we compute obey the steady-state sum rules of Eqs. (66), (69), and (75), which describe every stage of the process. This is clearest when considering the spin system, shown in Fig. 15(b), where the forms of $P_0^{\rm SP,S}$ and $P_0^{\rm S,B}$ reflect the exponential increase in its sensitivity to driving at frequencies near the edges of the two-triplon band, which we have seen already in Secs. IV and V B. This is particularly true in Fig. 12, which can in fact be understood as a graph of energy absorption by the spin system (red colors being high values). Although both energy flows bear a close resemblance to Fig. 8(a), we note from the latter that the quantity summed to obtain the net power contains an additional weighting factor of ω_k; among other effects, this acts to make the heights of the peaks at $2\omega_{\rm min}$ and $2\omega_{\rm max}$ more symmetrical in Fig. 15(b) than in Sec. IV.

Turning to the phonon system, in Fig. 15(a) we show the input energy flow from the laser, $P_0^{\rm L,P}$, the energy flowing out of the driven phonon due to the spin system, $P_0^{\rm P,SP}$, and the output flow directly from this phonon to the bath, $P_0^{\rm P,B}$. Our first observation is that, in the regime of weak spin-phonon coupling considered here, the majority of the laser energy flows directly to the bath, while the quantity central to our analysis, $P_0^{\rm P,SP}$, is always relatively small. Next we observe that it peaks around $\omega_0 = 2\omega_{\rm min}$ and $2\omega_{\rm max}$, as anticipated from Sec. IV. To illustrate the relative importance of the energy in the spin-phonon coupling term, $H_{\rm sp}$, we show $P_0^{\rm P,SP}$ once more as the green line in Fig. 15(b) for comparison with $P_0^{\rm SP,S}$. Their difference, $P^{\rm SP,B}$, remains at the percent level for all driving frequencies within the two-triplon band, indicating that $H_{\rm sp}$ does not act to store significant energy, but in essence transmits it from the phonon to the spin system as expected physically. At very high and very low frequencies, $|P^{\rm SP,B}|$ becomes a more significant fraction of the energy in the spin system, but this energy is in turn a very small fraction of the total (laser) energy flowing through the system. We take these results as evidence that treating the spin-phonon term as a perturbation in the mean-field approach is well justified, and by extension that the neglect of higher spin-phonon correlations is appropriate for the relevant driving frequencies.

We comment in passing that $P^{\rm SP,B}$ can in fact have a negative sign, implying a small energy flow from the bath due to the spin-phonon coupling term. While this may at first appear counterintuitive, we stress that the splitting of the system Hamiltonian into the three parts $H_{\rm p}$, $H_{\rm s}$, and $H_{\rm sp}$ [Eq. (1)] is somewhat arbitrary, and combining $H_{\rm s}$ and $H_{\rm sp}$ would remove this feature. In total, there is no violation of the fact that energy flows from the combined spin-phonon system into the bath, and indeed one may compute this net power, $P_0^{\rm P,B} + P_0^{\rm SP,B} + P_0^{\rm S,B}$, which by the sum rules at each step of Fig. 14 matches $P_0^{\rm L,P}$. We do not calculate $P_0^{\rm B,H}$, assuming simply that it matches the power flowing into the bath.

Because $P_0^{\rm L,P}$ is the average power, or fluence, taken up by the combined spin-lattice system, it is closely related to quantities that might be measured in an absorption experiment. To make contact with experimental methods it is necessary to generalize our treatment. In comparison with a conventional pump-probe procedure, we have considered only the pumping step, because in a NESS there is no concept of a delay time before probing. Further, we have considered pumping only at the frequency of one hypothetical phonon, lying at any value of ω_0, which we have varied to probe the behavior of

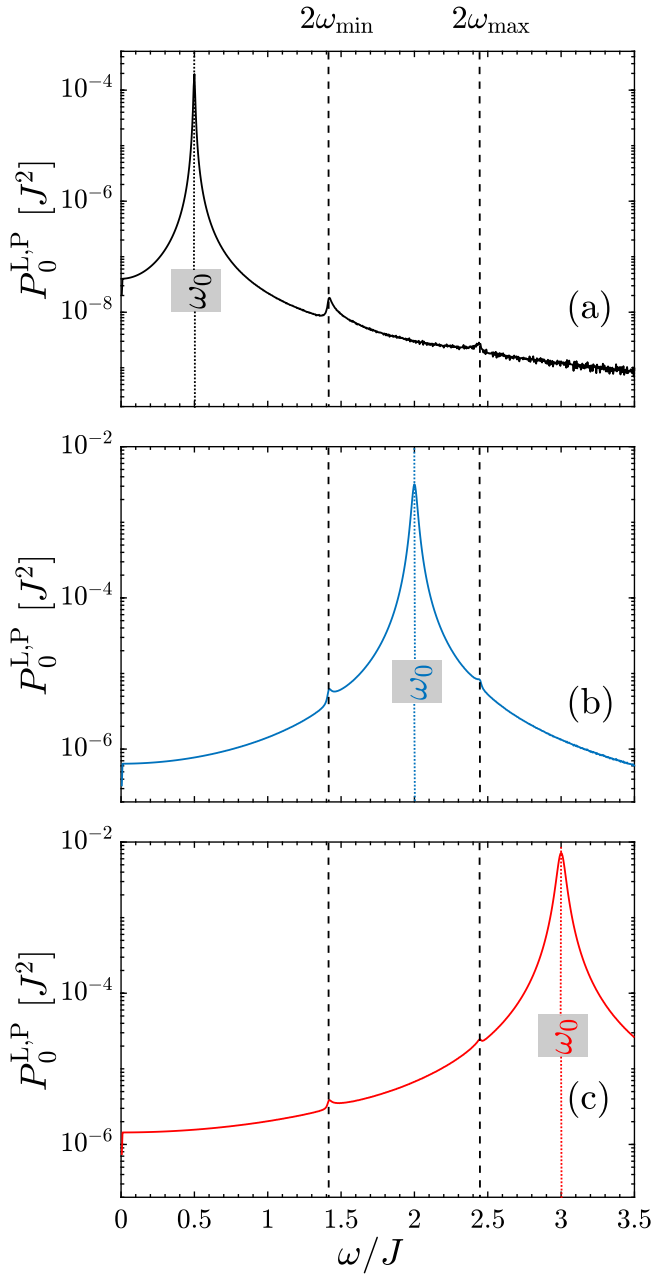

FIG. 16. $P_0^{\rm L,P}$ shown as a function of ω for $\gamma = 0.02\omega_0$, $a/\gamma = 0.2$, $g = 0.1J$, and $\gamma_{\rm s} = 0.01J$, for systems with one phonon (coupled to the J bond as in Sec. II) at a frequency (a) $\omega_0/J = 1.0$, (b) $\omega_0/J = 2.0$, and (c) $\omega_0/J = 3.0$.

the spin system. By contrast, in a real material there is only one, or a small number of, phonon(s) coupled strongly to the primary magnetic bonds, but it is relatively straightforward to pump the system at all frequencies $\omega \neq \omega_0$. Thus in Fig. 16 we depart from the conventions used so far in our study and adjust the frequency of the driving laser in order to illustrate the fluence as a function of ω for systems with one strongly coupled phonon, which lies at a frequency below, in, or above the two-triplon band.

In this type of experiment it is clear that the resonant phonon at ω_0 dominates the absorption. However, the fingerprints of the two-triplon band are visible as, for the parameters chosen, 0.1%-level effects across the full frequency range of the band. This nonresonant absorption is naturally stronger in a material where the relevant phonon lies close to the frequencies $2\omega_{\rm min}$ and $2\omega_{\rm max}$. We recall that the net fluence at the phonon peak increases with ω_0^2, and thus that pumping higher-lying phonons may result in a stronger signal if these are suitably coupled to the spin system.

However, for driving a phonon that lies very close to a resonant frequency of the spin system, we draw attention to an additional phenomenon. The blue line in Fig. 15(a) shows that the absorption peak at $\omega = \omega_0$ is actually suppressed when ω_0 lies in the spin band, most strongly so for phonons resonant with $2\omega_{\rm min}$ and $2\omega_{\rm max}$. This "self-blocking" effect appears initially to be counterintuitive, as one might expect stronger absorption when more system degrees of freedom are at resonance with the incoming laser. However, the spin system is not coupled directly to the light, being excited only by the driven phonon, and this situation suggests a heuristic image of the spin system as an extra "inertia" that the driven phonon must move. While we also used this word Sec. V A, a rather more specific description of the physics can be read from the prefactor of $p(t)$ in Eq. (38c), where one observes that the spin system acts against $E(t)$, making it more difficult for the phonon to draw energy from the laser electric field by oscillating maximally. Once this self-blocking effect is taken into account, the difference between the blue and red dashed lines in Fig. 15(a) shows the additional absorption of the incoming fluence actually taken up by the spin system [shown again in more familiar form in Fig. 15(b)].

B. Heating

Both conceptually and experimentally, extended continuous driving must inevitably lead to heating, which without remediation would destroy the coherence of the system, and later the system itself. Throughout this work we have assumed that the heat sink represented in Figs. 1 and 14 will be able to maintain a constant, low system temperature despite the steady drive, and our brief analysis of relaxation to equilibrium in Sec. V C was predicated on this assumption. We now turn to a quantitative investigation of the reality of the situation in driven condensed-matter systems.

We comment first on the physical meaning of the Lindblad bath model. Because the energy flowing directly from the driven phonon to the bath, $P^{\rm P,B}$ in Eq. (64), is directly proportional to the phonon damping and phonon occupation, $\gamma n_{\rm ph0}/\omega_0$ of the phonon energy is transferred to the bath in every period. Thus for the parameters we use, an energy of ω_0 per dimer is dissipated after approximately 1500 cycles; we recall that in our model the Einstein phonon modes are present on every bond in the system, meaning that the laser driving is a bulk effect. To introduce some typical numbers for quantum magnetic materials, we consider the inorganic compound $CuGeO_3$, which forms a quasi-1D spin-1/2 system and has been well characterized in the context of quantum magnetism at equilibrium. In fact $CuGeO_3$ was studied in detail [94,95] due to its spin-Peierls behavior, by which is meant that it shows a lattice transition from a uniform to an alternating chain that is driven by reducing the energy in the magnetic sector. This type of transition is a ground-state

phenomenon not related to the phonon driving we consider here, and our present analysis would in principle be applicable to the distorted state; however, $CuGeO_3$ also possesses second-neighbor and interchain interactions, and thus the nature of the transition has remained the subject of some debate. Although $CuGeO_3$ is known for its strong spin-phonon coupling, meaning that its g value lies outside the weak-coupling regime we consider here (for analyzing driven, out-of-equilibrium physical properties), we borrow its thermal parameters to analyze energy transfer and heating.

$CuGeO_3$ has leading magnetic exchange constants of approximately 10 meV [96], and so we use this value for illustrative energy estimates. Taking the triplon band width into account, we will assume that a phonon driving the system near $2\omega_{\min}$ also has $\hbar\omega_0 = 10$ meV ≈ 2.4 THz ≈ 80 cm^{-1}. The phonon spectrum of $CuGeO_3$ contains Raman and IR-active modes over a wide range of frequencies [97], with the lowest-lying IR-active modes at 6.0, 11.9, and 16.4 meV. Because all of these normal modes involve some motion of all the atoms in the unit cell, a quantitative model of the type we consider would have J and J' modulated simultaneously by the driven phonon. Proceeding with the illustrative phonon frequency of 10 meV, from Eq. (64) we obtain for the parameters of Secs. III and IV ($n_{\rm ph0} = 0.04$ and $\gamma = 0.02\omega_0$) that the energy deposited in the bath by the driving phonon is

$$\begin{aligned} P_0^{\rm P,B} &= 1.95\times10^{-11}\ {\rm Js}^{-1}\ \text{per dimer} \\ &= 5.89\times10^{12}\ {\rm W}\ \text{per mole of spins.} \end{aligned} \tag{76}$$

As noted in Appendix B, this value of $n_{\rm ph0}$ poses no risk of melting the lattice. However, to understand the effect of the energy in Eq. (76) on the lattice temperature, we use the result [98] that the low-temperature specific heat of $CuGeO_3$ is given approximately by the standard pure-phonon form, $C = \beta T^3$, with prefactor $\beta \approx 0.3$ mJ/(mol K^4). Thus the time required for the driven system to reach a temperature $T_{\max}$ in the absence of any cooling apparatus would be

$$t_{\rm h} = \frac{\beta}{4P_0^{\rm P,B}}\left[T_{\max}^4 - T_{\rm init}^4\right] \approx 1.2\times10^{-17}\left[T_{\max}^4 - T_{\rm init}^4\right]\frac{\rm s}{\rm K^4}. \tag{77}$$

Starting at $T_{\rm init} = 0$ or 2 K, the time required to reach a temperature $T_{\max} = 20$ K is $t_{\rm h} = 2.04\times10^{-12}$ s. We assume that this $T_{\max}$ is a realistic estimate of the temperature where one could no longer argue for quantum coherence of spin processes taking place in a triplon band whose minimum lies at 5 meV. The resulting $t_{\rm h}$ corresponds to only five cycles of the driving phonon and is clearly too short by a factor of several hundred when compared with the results of Secs. III to V.

Even allowing for considerable latitude with system parameters and materials choices, it is clear that the study of spin NESS in a quantum magnet is not realistic without an efficient heat sink attached to the sample (Figs. 1 and 14). To address the effect of the heat sink, it is necessary to introduce further materials parameters, specifically for sample dimensions and the thermal conductivities removing heat from the sample. As will shortly become clear, there are two reasons why an experiment of the type we analyze is relevant for a very thin sample, and thus we illustrate the heat flow for a thickness of 20 nm. Using that the mass of one mole of spins in $CuGeO_3$ is 184 g and the density is 5.11 g cm^{-3} [99], a sample of area $A = 1$ mm^2 would be 5.54×10^{-10} moles of $CuGeO_3$, meaning from Eq. (76) that a laser power

$$P_{\rm laser} = 3.26\ {\rm kW}, \tag{78}$$

should be transported through this area to the heat sink. First, for the sample itself, the thermal conductivity of $CuGeO_3$ at low temperatures is neither constant nor isotropic, but an approximate value for the cross-chain (b-axis) direction is $\kappa = 0.1$ W/(K cm) [100]. For the rate at which heat leaves the sample, we compute

$$P_\kappa = \kappa A\Delta T/\Delta l = 9.0\ {\rm kW}, \tag{79}$$

where we have set $\Delta T = T_{\max} - 2 = 18$ K as the temperature difference across the sample ($\Delta l = 20$ nm). Thus the qualitative conclusion from this crude estimate is that the thermal conductivity of the sample can match the power to be dissipated if a sufficiently thin film can be prepared. In slightly more detail, an energy-flow balance would dictate that ΔT should stabilize around 8.5 K.

This worked example illustrates that $P_{\rm laser}$ is directly proportional to Δl and P_κ inversely proportional, making the film thickness a crucial parameter. Nevertheless, the penetration depth of light into insulating matter is not well characterized for frequencies where the light is resonant with phonon excitations, and further with the spin sector. As a consequence, a thin film is indeed the most reliable geometry for ensuring that the bulk is uniformly irradiated by the incident laser beam. Materials that are difficult to prepare as thin films therefore suffer the twin disadvantages that their thermal conductivity becomes a bottleneck in the energy-flow process and that attenuation of the laser electric field inside the sample becomes a concern. While a significantly more detailed and materials-specific analysis is required for planning an experiment, our considerations indicate that it it always possible to study spin NESS in thin-film systems.

Certainly an optimized cooling system is a prerequisite for such studies, even at the nominally weak driving strengths ($n_{\rm ph0} = 0.04$) we have considered in Secs. III to V. The heat sink should be a highly conducting metal able to remove the input power efficiently, and thus no bottleneck should arise due to its thermal contact or the thermal conductivity. However, metals are not known to have a high heat capacity, and thus we estimate the thermal energy that could be taken up by a metal block. We consider high-quality Al (residual resistivity ratio RRR = 30) and note first that $\kappa_{\rm Al} = 1$ W/(K cm) [101], which is well in excess of the value in $CuGeO_3$. The specific heat has the form $C = \gamma_{\rm Al}T$ with $\gamma_{\rm Al} \approx 0.05$ J/(kg K^2) at low temperatures [101], and hence for a block with area 1 cm^2 and thickness 5 mm (giving a mass $m = 1.35$ g [101]), the energy absorbed by increasing the temperature from $T_{\rm init} = 2$ K to $T_{\rm hs}$ is

$$\Delta E = \tfrac{1}{2}\gamma_{\rm Al}m\left[T_{\rm hs}^2 - T_{\rm init}^2\right] = 7.1\times10^{-4}\ {\rm J} \tag{80}$$

if the temperature of the heat sink is limited to 5 K. With an input power of 3.26 kW, the time to overheating of the block is

$$t_{\rm sink} = 2.2\times10^{-7}\ {\rm s}, \tag{81}$$

which corresponds to over half a million cycles of the 2.4 THz driving phonon. Thus an Al heat sink has plenty of reserve capacity for the purposes of a NESS experiment.

Returning to the beginning of the experimental process depicted in Figs. 1 and 14, we have assumed that the parameter a is freely variable. The maximum electric field in a modern THz laser source is approximately $E = 3\times10^{8}$ Vm^{-1} [78]. If one assumes that the field acts on an oxygen ion, one obtains

$$a = \tfrac{1}{\sqrt{2}} 2eEq_{\rm osc} = 4.8 \text{ meV} \tag{82}$$

where $q_{\rm osc} = 1.1\times10^{-11}$ m when computed using $M_{\rm O}$. For comparison, the value we have used to ensure $n_{\rm ph} = 0.04$ in Secs. III to V corresponds with $\hbar\omega_0 = 10$ meV to $a =$ 0.16 meV. Thus even for predominantly reflective surfaces, values of a suitable for probing the energy range of J and ω_0 typical in inorganic quantum magnets are readily achievable.

In summary, experiments of the type we discuss to establish and to control bulk quantum spin NESS are possible in real magnetic materials. The sole caveat is that it should be possible to prepare the system with a thickness in the range of tens of nanometres. Even at the rather modest phonon occupations required to observe nontrivial nonequilibrium spin states, maintaining the spin system at a low temperature over a long period of steady driving does pose a significant challenge to the cooling capacity of a conventional cold finger, which normally is designed to control the system temperature with high precision using liquid ^{4}He coolant, rather than functioning as an optimized heat sink. We assume that both of the issues we have identified can be solved for a wide range of quantum magnets. However, in the event of a materials system that does not allow the driving energy to be removed quickly enough to avoid heating, one solution may lie in altering the experimental geometry away from laser irradiation of the entire sample, as we discuss in more detail in Sec. VII B.

VII. DISCUSSION

A. Approximations: Time, coupling, and intensity scales

In constructing our description of the phonon-driven and dissipative quantum magnetic system we have appealed to a number of approximations. In fact establishing the validity of the framework presents an interlinked problem involving (a) the treatments we have adopted for the laser, for the spin and phonon sectors, and in the master-equation method, (b) the fast and slow timescales of the spin-lattice system, (c) the coupling constants, and (d) the intensities or mode occupations. As examples, the magnetic interactions determine our treatment of the dimerized chain, a relatively weak spin-lattice coupling is intrinsic to our treatment of both sectors, the timescales of the dynamics in these sectors should allow the Born-Markov and rotating-wave approximations within the quantum master equation, and if mode occupations are too high anharmonic or nonlinear effects can set in.

1. Triplons as bosons

A first approximation is that we treat the triplons as noninteracting bosons, diagonalizing them by a standard Bogoliubov transformation. The triplons in a system of coupled dimers are in fact hard-core bosons, because at most one may be present at each site, and finite intertriplon interactions are well known when the quasiparticles are adjacent to each other in real space. However, for relatively low densities (below our threshold of $n_{\rm x}^{\rm max} = 0.2$) and weak interdimer coupling, $\lambda = J'/J \leqslant 0.5$, approximating the triplons as interaction-free bosons is well justified [92], as discussed in Sec. II A. To study the regime of larger interdimer coupling, the standard Bogoliubov transformation can be replaced by a unitary transformation controlled to high orders in λ [102–104].

2. Laser and mean-field decoupling

As noted in Sec. II, we have described the laser field driving the optical phonon as a classical oscillating field. In view of the fluences commonly used in experiment, which make the quantum fluctuations of the laser field negligible relative to its expectation value, this approximation is perfectly justified. The time-dependent mean-field decoupling of the driven phonon and the spin system [Eq. (21a)] is a further approximation, although we have demonstrated in Sec. VI that it is well justified at all relevant driving frequencies. From the definition of Eq. (37), $O(10^{-2})$ values $n_{\rm ph}$ on every bond mean that the optical phonon is macroscopically occupied (the phonon number, being proportional to the system size, is extensive). Thus the relative size of the quantum fluctations is again negligible, justifying a mean-field treatment of the phononic field. While we cannot exclude completely that more complex physics occurs for particularly large spin-phonon coupling, such as triplon-phonon bound-state formation, this would need to be built first into the ground states and then into the driven dynamics.

3. Lindblad damping of driven phonon

The damping rate, γ, of the driven phonon should be significantly smaller than its energy, and we have set it to a value of order 2% of the phonon energy. The way that γ enters, which leads to the description of the driven phonon as a classical damped harmonic oscillator, is well justified for the reasons stated in the preceding paragraph. The Lindblad framework treats the relaxation of a degree of freedom by using its established damping term. More generally, fundamental theorems about the Lindblad formalism [42] state that the dynamics of an open quantum system can always be captured by decay rates for certain Lindblad operators, which we labeled A_l in Eq. (34); at this level, the only open issue is which operators in system Hamiltonian are the relevant Lindblad operators, but this is manifestly obvious for the driven Einsein phonon considered here.

A more physical question concerns the microscopic mechanism of this damping. Clearly, the only bath in an insulator at the energies we consider consists of the optical and acoustic phonons. Due to anharmonic effects, the driven phonon can decay into two (or more) other phonons. Compared to the single driven phonon, the large number of other phonons in a 3D material constitute a large bath, which is not strongly influenced by the driven phonon, except in cases where the driving exceeds the heat-sink capacities in the sense of Sec. VI and heating effects enter. The fact that the phonon lines observed in inelastic scattering studies are usually rather sharp

demonstrates that the coupling of a given phonon to the bath represented by the other phonons is weak, as a result of which the Born approximation is fully justified.

A further required property of the bath is to obey the Markov approximation, that its correlations should decay significantly faster than the decay dynamics of the quantum system (specified by the Hamiltonian). This property is difficult to verify without a detailed knowledge of all the phonons and their anharmonicities, but an estimate is possible. In general the spectrum of phonons covers the energy range from zero to the Debye energy, $\hbar\omega_{\rm D}$, and hence $1/\omega_{\rm D}$ sets the timescale for the decay of bath correlations. The Debye energy is typically 50–100 meV (12–24 THz). For driving frequencies in the 1–10 THz regime and a decay rate, γ, which is 1/50 of these, it is clear that the correlation time scale, $1/\omega_{\rm D}$, is indeed shorter than the timescale $1/\gamma$ of the phonon damping (with the possible exception of very soft materials). Finally, the rotating-wave approximation is the statement that one may neglect fast oscillations to focus only on the slow variables (as we did in Sec. V A) [42], and again this is clearly justified because the oscillatory terms for a phonon driven at ω_0 are fast on the timescale of the damping.

4. Lindblad damping of triplons

The previous arguments can be repeated to justify the use of t_k as the Lindblad operators in the spin sector. We observed in Sec. II C that these operators break spin conservation, so that our treatment is relevant for systems with finite spin-orbit coupling. If this coupling is low, spin conservation requires that one consider terms of the type $C_{kq} = t_k^\dagger t_q$, which we discuss in the next subsection (Sec. VII B). However, weak spin-orbit coupling also implies that the damping of spin excitations due to a phononic bath is weak, and thus it is not unreasonable to treat any magnetic excitations, which here are the triplons, as weakly damped oscillators. Because the strongest effects of driving the magnetic system occur when the driving frequency, ω_0, matches the magnetic energies, $2\omega_k$, estimates for the validity of the Born-Markov and rotating-wave approximations [42] are the same as for the driven phonon. We defer comments on momentum conservation in C_{kq} to Sec. VII B.

In summary, while the validity issue is a complex one, all of the approximations we have made are appropriate, and in fact for a typical condensed-matter system there is a reasonable amount of parameter space (Sec. VI). A broader discussion of materials and experiment may be found in Sec. VII C below. From a theory standpoint, our current approach is by design the simplest available, whose explicit intent is to establish the basic phenomenology, and a more detailed discussion of any given issue may require more sophisticated methodology. One example of this would be the use of flow-equation methods [105] to extend the regimes of validity, in the hierarchy of timescale approximations, of the equations of motion.

We close this part of the discussion by recalling that the intrinsic properties of the phonon-driven spin system lead to a number of phenomena occurring over a range of different frequencies and times. By frequency, the key regimes of driving are (1) in the spin band, where the response is resonant, (2) below the spin band, where it is controlled by multiphonon processes, and (3) above the spin band, which is the Floquet regime, featuring weak energy absorption and coherently superposed phase- and frequency-shifted states. By time, transient phenomena at switch-on occur (mostly) on the scale of the inverse damping (Sec. V A), drive-induced heating occurs on a strongly ω_0-dependent timescale, and relaxation phenomena at switch-off follow the Lindblad form to restore the starting state (Sec. V C).

B. Bath models and system heating

The equations of motion whose solutions we have studied in Secs. III to V are intrinsic to one type of bath. As stated in Sec. II C, the physical content of the Lindblad formalism is that the spin operators are damped by bath operators that also appear in the spin Hamiltonian. However, the nature of these terms must reflect the physics of the entire system, by which is meant the manner in which energy can be dissipated by spin and phononic processes. Here we comment briefly, and with one specific example, on how our analysis would be extended in the case of more complex bath terms.

It is clear in Sec. II C that our use of t_k as the sole type of spin-bath operator delivers the most straightforward equations of motion, and we have exploited the complete independence of all k states to explore a wide range of phenomena. However, it is also clear that damping processes involving a single t_k operator are spin-non-conserving, allowing a triplon to decay into a phonon. In a truly 1D system, meaning a spin chain in a 1D lattice, momentum conservation would restrict the phase space available for such processes, raising problems with the applicability of the Lindblad formalism (which requires that the bath contain a continuum of energy states [42]) that would at minimum mandate a significant k-dependence of the decay rate, $\gamma_{\rm s}(k)$. However, as explained in Sec. II C, such concerns are not relevant to the present analysis because the 1D triplons are embedded in a real lattice, meaning with 3D phonons. In this case, for each momentum, $\hbar k$, along the spin chains, there is a continuum of perpendicular momenta, $\hbar\vec{k}_\perp$, and hence the annihilation of the triplon can occur for a wide range of $\vec{k}_\perp$ values, with the bath phonons that are created covering a broad energy range. This energetic continuum will depend on k, but only weakly, which both justifies using the Lindblad formalism and indicates a constant, momentum-independent damping rate, $\gamma_{\rm s}$.

Nevertheless, the conventional spin-phonon coupling in any $3d$ transition-metal compound, and hence the spin-damping effect of its phononic modes, takes the form of $H_{\rm sp}$ in Eq. (17), and the spin-isotropic nature of this interaction means that phonon modes cannot alter the spin state (the number of excited triplons) directly. The most straightforward spin-conserving bath operators appropriate to this situation, based on the operators t_k in the spin-system Hamiltonian, would be of the form $C_{kq} = t_k^\dagger t_q$, and for the reason given above need not be momentum-conserving. Bath operators with the form of C_{kq} manifestly act to mix wave-vector states of the system and thus lead to a significantly more involved set of equations of motion, with in general N^2 coupled equations rather than only N. We defer a detailed analysis of this case to a follow-up study.

As already noted, the type of bath studied in the present work provides a meaningful description of systems with spin-dependent phonon scattering processes. These can arise in systems with appreciable spin-orbit coupling, meaning 4*d* and especially 5*d* magnetic ions, where the resulting anisotropic interactions include may Dzyaloshinskii-Moriya (DM), exchange anisotropies (XXZ and XYZ), or even bond-selective interactions. However, only in rather exceptional circumstances would these dissipative channels be stronger than spin-conserving damping terms, and thus the consideration of more advanced bath operators is required to discuss real experiments. In addition to the question of spin conservation, it is also necessary to address the issue of spin-system dimensionality, which as in the present study may be lower than the phonon-system dimensionality (which is 3D), and hence to establish the level at which to enforce conservation of momentum.

The nature of the bath reflects directly on the heating of the system, which was discussed for the simple, spin-non-conserving case in Sec. VI. In a more complex bath, one may expect the redistribution of energy through the modes of the spin system to be more efficient, although this is in general a small contribution to the (phonon-dominated) system temperature. Of more practical relevance to the issue of quantum coherence is the fact that a momentum-mixing bath operator would also impact the coherence of individual k-components of the spin system. From this standpoint one may consider "reservoir engineering" [106], meaning influencing the form of C_{kq} (for example by promoting forward-, backward-, or skew-scattering in the bath), as an alternative to controlling the system temperature only through the balance between the laser driving strength and the cooling apparatus (Sec. VI).

With a view to maintaining quantum coherence in the spin sector, we turn to some more general considerations for controlling the temperature of the system. We remark that in some classes of system it is possible to decouple the degrees of freedom in such a way as to obtain effective electronic or spin temperatures different from the lattice temperature. However, this is not an option in a system of spins localized on the sites of a lattice, where the temperature controlling the response of the spin system is that of the lattice. Similarly, our model is also far from the paradigm of a spatially separate system and bath, where different effective temperatures for the two components are related by controllable coupling constants. Within the confines of the situation we consider, we mention two approaches to temperature control, namely, system geometry and the laser driving protocol.

In the present work we have considered only bulk driving by the electric field of the laser, meaning that the Einstein phonon of every bond is stimulated. In Sec. VI B we showed that this "bulk" system should in fact be rather thin (tens of nanometres). However, it is certainly possible that a device of μ or mm length is illuminated only at one end, causing the phonon and spin excitations to propagate through the equilibrium material over a distance far larger than the nonequilibrium irradiated portion, and possibly larger than the penetration depth of the light. Such a situation would require a model for spatial gradients of heat, magnetization, and temperature, which would certainly be of direct interest for switching and transport in spintronic devices. To date some experiments already present this type of situation [72], and certain theoretical discussions have also invoked the framework of driving only at the ends of the system [51,52,107].

Finally, another means of controlling the system temperature lies in driving by repeated short pulses. In its simplest form, this allows the system to relax back to its cold state by the action of the heat sink (Sec. V C), although the required pulse separation would be a very slow timescale (Sec. VI B). At a more sophisticated level, pulsed driving processes allow new degrees of control over the system, including the imposition of dynamics on new timescales quite separate from the driving frequency, as in the case of Floquet engineering of the electronic band structure [34]. While certain types of driving protocol have already been proposed for controlling small numbers of quantum spins [4] and ensembles of effectively $S = 1/2$ quantum dots [56,57], for now we leave open the application of these ideas to the many-body spin systems considered here.

C. Experiment

As stated in Sec. I, the last decade has seen an enormous expansion in the technological capabilities of laser sources, both in ultrafast timescales and in high intensities, with applications both for pump-probe experiments and for steady driving. Where in Sec. I the focus of our remarks was the new physics made possible by these new sources, it is also worth commenting on the new technologies that have led to such growth in the application of lasers to condensed matter. For decades this was limited by the "Terahertz gap," the problem that light at the energies of most interest to the intrinsic processes in condensed matter was neither easily generated nor easily guided or focused, but was easily absorbed and scattered. Starting with the initial compilation of methods making it possible to engineer transient states of condensed matter [108], further technological solutions have been developed and applied to frontier science challenges [109]. The best review of terahertz enabling technologies, both for generation and for beam control, may be found in Ref. [110]. On the generation side, one has not only new free-electron laser sources but also a range of new "table-top" techniques, including plasma-based sources and high-harmonic generation, many made possible by exploiting new materials. On the control side, beam guiding, transport, focusing, and diagnostics have also benefited strongly from the optical properties of certain materials. Together this progress has led to a qualitative expansion in the type of physics that can be probed, or indeed created, in condensed matter, and the aim of the present study is to extend these capabilities to quantum magnetic materials.

For the purposes of this preliminary analysis, we have focused on well-dimerized (and thus robustly gapped) quantum spin chains, meaning that the system we consider does not, either at equilibrium or in its driven state, approach a phase transition to a magnetically ordered, to a gapless quantum disordered, or to any other different magnetic state. In a 1D system with only Heisenberg spin interactions, the primary requirement is simply that the spin gap (the one-triplon band minimum, $\omega_{\min} = \omega_{k=0}$) does not close, including on laser driving of a selected phonon. An excellent example of an inorganic compound realizing quasi-1D alternating $S = 1/2$

spin chains is $Cu(NO_3)_2$ [111], which is thought to have no anisotropy, negligible second-neighbor interactions, and a gap of approximately 0.38 meV (compared to a band width of 0.12 meV, yielding $\lambda = 0.14$). This material also shows no evidence of strong phonon coupling to the spin excitations [111], which indicates that it belongs in the weak-coupling regime we study. However, the magnetic energy scales in $Cu(NO_3)_2$ are lower by a factor of 20 than the test-case numbers presented in Sec. VI, presenting a different balance of slower heating rates, slower convergence to NESS, and altered damping ratios.

A recently discovered class of alternating spin-chain materials includes $AgVOAsO_4$ [112] and $NaVOAsO_4$ [113], which have magnetic coupling constants in the 5 meV range. Although here λ is at the upper validity limit of our present simple treatment of the spin chain (Sec. II A), as noted earlier, more sophisticated approaches are available for this purpose and no part of the equations of motion (Sec. II C) is invalidated. Another class of candidate systems is the set of metal-organic TTF compounds [114,115], and even purely organic TCNQ compounds [116], in which the spin-Peierls transition has been observed and the distorted (low-temperature) state is an alternating spin chain. A further category of interest in quantum magnetism has been alternating antiferromagnetic-ferromagnetic (AF-FM) $S = 1/2$ chains, primarily because of a tendency to Haldane physics in the strong FM regime, but in the remainder of the parameter space, which includes the materials $Na_3Cu_2SbO_6$ ($\lambda = -0.79$) [117] and $(CH_3)_2NH_2CuCl_3$ ($\lambda = -0.92$) [118], our analysis remains fully applicable regardless of the signs of the interactions.

In addition to $CuGeO_3$, which we introduced in Sec. VI to consider its thermal properties, $(VO)_2P_2O_7$ [119,120] constitutes a further system that in fact realizes alternating $S = 1/2$ spin chains with significant interchain interactions. However, the anomalously large g values that made both of these compounds attractive for equilibrium experiments in quantum magnetism do place them outside the weak-coupling regime we analyze here. In a later study we will extend our considerations to the regime of strong spin-phonon coupling, which is also described by the equations of motion derived in Sec. II. Here one may anticipate nonlinear driving effects (Figs. 3 and 5), which could allow experiments at lower laser intensities, stronger mixing of frequency harmonics (Figs. 6 and 7), stronger below-band multiphonon processes (Fig. 12), more delicate driving-induced anomalous convergence (Sec. V A), and stronger transfer of spectral weight between different frequencies (Fig. 16).

Returning to the spin sector alone, our present formalism is readily extended to alternating chains with different gap-to-bandwidth ratios, although an accurate treatment of systems with small gaps would require a more numerical approach for the systematic summation of perturbative terms to high orders, as in the method of continuous unitary transformations (CUTs) [102–104]. Other 1D gapped spin systems to which our considerations are immediately applicable include even-leg $S = 1/2$ spin ladders and Haldane ($S = 1$) chains. A parallel class of systems that could be treated by very similar considerations would be that of magnetically ordered quantum spin systems, which includes many 2D and 3D materials of all spin quantum numbers; this would involve the straightforward adoption of a (constrained) spin-wave framework to describe the spin sector. Ordered magnetic systems also provide the simplest cases in which to analyze the effects of anisotropic magnetic interactions, such as single-ion, DM, XXZ, and other terms, which have recently attracted intensive interest with a view to creating topological magnons [58–61], vortices [63], skyrmions [64], and other means of encoding protected quantum information [2]. More complex spin sectors include anisotropic systems such as Ising and XY models without magnetic order, gapless spin chains, and gapped or gapless nonordered states in higher dimensions, meaning in the former category Z_2 quantum spin liquids and in the latter algebraic spin liquids and quantum critical systems. Here the challenge is not only to find a suitable framework in which to describe the complex correlated spin sector, especially if this is changed by using laser driving to push it across a magnetic quantum phase transition, but also to deal with the situation where the excitations of the spin system extend to arbitrarily low energies, thus interacting strongly with even the acoustic phonons.

In addition to an adequate treatment of the spin sector, the quantitative analysis of real materials will require accurate lattice dynamics calculations to give the phonon modes and frequencies, and the corresponding oscillator strengths. The normal modes can be used to estimate spin-phonon coupling strengths and the frequencies to choose the laser excitation parameters. Typically, the phonon spectrum in inorganic materials extends up to the Debye energy, which rarely exceeds 100 meV (24 THz), while a lower limit for optical phonons is perhaps 5–10 meV. Spin energy scales can extend up to a one-magnon band maximum of 300 meV (70 THz) in cuprates and have no lower limit. There is no established relationship between the two, as materials with predominantly high-energy phonon modes can have a very low-energy spin sector, and those with high spin energies need have no special phonon properties. However, metal-organic systems do tend to have a softer phonon sector, due to the nature of the interactions between weakly polar organic groups, and very low magnetic energies due to the long paths between magnetic ions. Thus it is safe to say that a very wide range of frequency scales and phononic modulation possibilities is available for planning experiments of the type we discuss.

Finally, it is also necessary to consider how to measure all of the physical quantities characterizing the spin system using a terahertz laser. In Sec. VI A we presented the example of absorption of the incident laser fluence (Fig. 16), while further quantities that are also functions of frequency and temperature include reflection, polarization rotation (due to birefringence changes or the Faraday effect), and the two-magnon response. It is not generally possible to probe the wave-vector response of the spin sector, except in special cases possessing a strong coupling to one well-characterized "probe phonon" mode. In most such measurements, the signal arising due to the spin system will be weak in comparison with the many other contributions to the total response of a sample, and here we point to the strong frequency-selectivity allowed by the phonon-coupled model, and visible in Figs. 15 and 16, as the primary means of ensuring that the spin signal is detectable.

VIII. SUMMARY

We have investigated the nonequilibrium steady quantum mechanical states of a lattice spin system under the continuous, coherent laser excitation of phonons at a single frequency and in the presence of a realistic dissipation. In real materials, this dissipation is dominated by the many phonons of the lattice system, and its inclusion at the operator level, which we effect within the Lindblad formalism, goes beyond much of the work on driven many-body systems presently in the literature. We have focused for pedagogical purposes on a simple example of a gapped quantum mechanical spin system, the dimerized spin chain, and a simple example of a driving phonon, a bulk Einstein mode, but stress that the framework we have established can be extended, with additional numerics, to fully realistic examples of both systems. By establishing and solving the quantum master equations governing the time-evolution of this model system, we have demonstrated the establishment of quantum spin NESS and investigated their dependence on all of the parameters describing the lattice and spin sectors, including their driving, dissipation, and coupling.

We have performed a detailed analysis of the internal dynamics of the driven quantum spin NESS, and of the accompanying behavior of the driven lattice system. We find that the NESS amplitude shows a dramatic sensitivity to the frequency of the driving phonon, peaking strongly at the upper and lower edges of the band of two-triplon excitations. Beyond the frequency, we characterize this response as a function of the driving electric field, the lattice and spin damping coefficients, and the spin-phonon coupling, which causes a rapid onset of strong mutual feedback between sectors. We use the Fourier transform to analyze the components of the spin NESS appearing at different harmonics of the driving frequency even in the weak-coupling regime. By investigating the k-resolved response of the spin system we demonstrate that resonance in frequency is also strongly k-selective.

Our equations of motion are valid at all times and we use them to study both the transient behavior of the system when driving is switched on and the relaxation to equilibrium when the driving is removed. At switch-on we find a complex phenomenology where even the weakly coupled system can be driven close to thresholds, in triplon occupation and rate of excitation, at which its characteristic timescales are renormalized strongly. We have computed the energy flow through the composite spin-lattice system, from its arrival as the driving laser light to its dissipative loss. The energy offers a new window on frequency-sensitivity, allows us to gauge the self-consistency of our analysis by applying sum rules, and shows an unexpected "self-blocking" effect, whereby the spin system suppresses the uptake of laser power near resonance. Because the Lindblad formalism gives direct access to the energy flow into the bath, we have used our framework to estimate heating timescales and hence the practical requirements, in the form of driving limits, sample geometry, and cooling capacity, of a NESS experiment in a real material.

The framework we establish makes it possible to perform quantitative investigations of many different types of spin system, including those with magnetic order, with small or vanishing gaps, with topological properties, or with nontrivial quantum entanglement. It also enables the analysis of more complex types of bath, most notably ones describing spin-conserving dissipative processes, and hence the modeling of real materials with laser-driven phonons. With appropriate treatment of spatial gradients (in driving, magnetization, and temperature), one may also model real device geometries, leading to spintronic applications where the challenge is to preserve quantum coherence over the timescale required for reading and processing the quantum information encoded in the spin sector.

ACKNOWLEDGMENTS

We thank D. Bossini, F. Giorgianni, S. Haas, C. Lange, Z. Lenarčič, A. Rosch, Ch. Rüegg, and B. Wehinger for helpful discussions. Research at TU Dortmund was supported by the Deutsche Forschungsgemeinschaft (DFG, German Research Foundation) through Grant No. UH 90-13/1 and together with the Russian Foundation of Basic Research through project TRR 160. Research at the University of Göttingen was funded by the DFG through Grant No. 217133147/SFB 1073, project B03. Research at LANL was supported by the U.S. DOE NNSA under Contract No. 89233218CNA000001 through the LANL LDRD Program.

APPENDIX A: DETUNED TRIPLON PAIR CREATION

In Sec. V A we analyzed the gradual change of the diagonal triplon components, $u_k(t)$, in the resonant case, by which is meant for $\omega_0 = 2\omega_{k_{\rm res}}$. Henceforth we omit the subscript k. If this resonance condition is not met, we state that there is a finite detuning, $\delta = 2\omega - \omega_0$. In this Appendix we present the differences between the derivations for the detuned and resonant cases (Sec. V A). In the detuned case, Eq. (52a) still holds, but the definition of Eq. (52b) changes to

$$F(t) = \int_0^t \left[\tilde{u}(t') + \frac{3}{2}e^{\gamma_s t'}\right] e^{-i\delta t'}\, dt', \tag{A1}$$

which implies that $F(t)$ is no longer real, but complex. Equation (53a) still holds, but Eq. (53b) is modified to

$$\tilde{u}(t) = e^{\gamma_s t}u(t) \;=\; \Gamma^2\,\mathrm{Re}\left[\int_0^t e^{i\delta t'}F(t')\,dt'\right], \tag{A2}$$

with Γ as defined in Eq. (55). We stress that the validity of replacing the rapidly oscillating terms by their average, as performed in Eq. (51), is justified if $|\delta| \ll \omega_0$. If the detuning becomes too large, the deviations from the full result may become large, but comparing our analytical approximation to the results of a numerical integration revealed very good agreement over a broad range of parameter space.

Equation (A2) does not lead to a closed differential equation by double differentiation because of the restriction caused by taking the real part. It is necessary instead to take three derivatives of $\tilde{u}(t)$ and define $x(t) = d\tilde{u}/dt(t)$, for which we obtain

$$\frac{d^2x}{dt^2}(t) = (\Gamma^2 - \delta^2)x(t) + \frac{3}{2}\Gamma^2\gamma_s e^{\gamma_s t}. \tag{A3}$$

Clearly, the nature of the solutions to this differential equation depends crucially on the sign of the prefactor, $\Gamma^2 - \delta^2$. As

in the resonant case (Sec. V A), if it is positive then exponentially increasing and decreasing functions appear, whereas if it is negative then oscillating trigonometric functions appear. Solving Eq. (A3) for the initial conditions $x(0) = 0$ and $dx/dt(0) = 3\Gamma^2/2$ and then integrating the resulting expression yields $\tilde{u}(t)$, from which the expressions given for $u(t)$ in Eqs. (60) and (62) follow.

APPENDIX B: LINDEMANN CRITERION

Breakdown of the lattice is governed by the Lindemann criterion [121], which dates to Lindemann's introduction of the concept that a solid will begin to melt when $\langle q^2\rangle \approx \rho^2 a_0^2$, meaning when the fluctuations, q, of its atoms around their equilibrium positions exceed a fraction, ρ, of the interatomic distance, a_0. While Lindemann used the concept to relate $\langle q^2\rangle$ to the melting temperature, $T_{\rm m}$, for our purposes it is sufficient to relate $\langle q^2\rangle$ to $n_{\rm ph}$.

It has been established for a broad range of condensed-matter systems that Lindemann's proposed relation holds, with the value of ρ being in the range 0.1–0.15 [122–124]. To relate this result with $n_{\rm ph}$, for a local phononic oscillation the potential energy is half of the total energy,

$$\frac{1}{2}M\omega_0^2\langle q^2\rangle = \frac{1}{2}\hbar\omega_0\left(n_{\rm ph}+\frac{1}{2}\right), \tag{B1}$$

which implies

$$\frac{\langle q^2\rangle}{q_{\rm osc}^2} = n_{\rm ph}+\frac{1}{2}, \tag{B2}$$

where $q_{\rm osc}$ is the oscillator length, $\sqrt{\hbar/(M\omega_0)}$. The Born-Oppenheimer approximation [125] implies that the characteristic length scale of the atomic motion, $q_{\rm osc}$, is a fraction $(m_{\rm e}/M)^{1/4}$ of the electronic length scale, which we identify crudely with a_0; here $m_{\rm e}$ is the mass of an electron and M the mass of the oscillating atom. Thus one obtains from Eq. (B2) that

$$\frac{\langle q^2\rangle}{a_0^2}\sqrt{\frac{M}{m_{\rm e}}} = n_{\rm ph}+\frac{1}{2}, \tag{B3}$$

and hence

$$n_{\rm ph}+\frac{1}{2} \approx \rho^2\sqrt{\frac{M}{m_{\rm e}}}. \tag{B4}$$

Using the mass of the oxygen atom as a generic value for M, and $\rho^2 \approx 0.02$ for the Lindemann ratio, we conclude that the phonon number should not exceed

$$n_{\rm ph} \approx 3 \tag{B5}$$

if the sample is to remain solid. Here $n_{\rm ph}$ is the total number per atom of phonons polarized in one direction and the conventional Lindemann criterion applies because we assume the chains to be embedded in a 3D crystal (no low-dimensional instability need be considered). From the estimates made above, it is clear that the Lindemann threshold is in no way threatened by the driven phonon occupations we consider, and thus that the integrity of the periodic lattice is not an issue.

[1] V. Baltz, A. Manchon, M. Tsoi, T. Moriyama, T. Ono, and Y. Tserkovnyak, Antiferromagnetic spintronics, Rev. Mod. Phys. **90**, 015005 (2018).

[2] A. V. Chumak, V. I. Vasyuchka, A. A. Serga, and B. Hillebrands, Magnon spintronics, Nat. Phys. **11**, 453 (2015).

[3] D.-Q. Jiang, M. Qian, and M.-P. Qian, *Mathematical Theory of Nonequilibrium Steady States* (Springer, Heidelberg, 2004).

[4] G. S. Uhrig, Quantum coherence from commensurate driving with laser pulses and decay, SciPost Phys. **8**, 040 (2020).

[5] M. S. Rudner, N. H. Lindner, E. Berg, and M. Levin, Anomalous Edge States and the Bulk-Edge Correspondence for Periodically Driven Two-Dimensional Systems, Phys. Rev. X **3**, 031005 (2013).

[6] L. D'Alessio and A. Polkovnikov, Many-body energy localization transition in periodically driven systems, Ann. Phys. **333**, 19 (2013).

[7] R. Nandkishore and D. A. Huse, Many-body localization and thermalization in quantum statistical mechanics, Annu. Rev. Condens. Matter. Phys. **6**, 15 (2015).

[8] K.-O. Chong, J.-R. Kim, J. Kim, S. Yoon, S. Kang, and K. An, Observation of a non-equilibrium steady state of cold atoms in a moving optical lattice, Commun. Phys. **1**, 25 (2018).

[9] R. Labouvie, B. Santra, S. Heun, and H. Ott, Bistability in a Driven-Dissipative Superfluid, Phys. Rev. Lett. **116**, 235302 (2016).

[10] M. Schreiber, S. S. Hodgman, P. Bordia, H. P. Lüschen, M. H. Fisher, R. Vosk, E. Altman, U. Schneider, and I. Bloch, Observation of many-body localization of interacting fermions in a quasirandom optical lattice, Science **349**, 842 (2015).

[11] A. Eckardt, Colloquium: Atomic quantum gases in periodically driven optical lattices, Rev. Mod. Phys. **89**, 011004 (2017).

[12] I. Bloch, J. Dalibard, and W. Zwerger, Many-body physics with ultracold gases, Rev. Mod. Phys. **80**, 885 (2008).

[13] I. Gierz, Probing carrier dynamics in photo-excited graphene with time-resolved ARPES, J. Electron Spectrosc. Related Phenomena **219**, 53 (2017).

[14] A. Cavalleri, Photo-induced superconductivity, Contemp. Phys. **59**, 31 (2018).

[15] M. Buzzi, M. Först, R. Mankowsky, and A. Cavalleri, Probing dynamics in quantum materials with femtosecond x-rays, Nat. Rev. Mater. **3**, 299 (2018).

[16] A. Zong, X. Shen, A. Kogar, L. Ye, C. Marks, D. Chowdhury, T. Rohwer, B. Freelon, S. Weathersby, R. Li *et al.*, Ultrafast manipulation of mirror domain walls in a charge density wave, Sci. Adv. **4**, eaau5501 (2018).

[17] S. Iwai, M. Ono, A. Maeda, H. Matsuzaki, H. Kishida, H. Okamoto, and Y. Tokura, Ultrafast Optical Switching to a Metallic State by Photoinduced Mott Transition in a Halogen-Bridged Nickel-Chain Compound, Phys. Rev. Lett. **91**, 057401 (2003).

[18] A. Zong, A. Kogar, Y.-Q. Bie, T. Rohwer, C. Lee, E. Baldini, E. Ergeçen, M. B. Yilmaz, B. Freelon, E. J. Sie *et al.*, Evidence for topological defects in a photoinduced phase transition, Nat. Phys. **15**, 27 (2019).

[19] T. Kitagawa, T. Oka, A. Brataas, L. Fu, and E. Demler, Transport properties of nonequilibrium systems under the

application of light: Photoinduced quantum Hall insulators without Landau levels, Phys. Rev. B **84**, 235108 (2011).
[20] N. H. Lindner, G. Refael, and V. Galitski, Floquet topological insulator in semiconductor quantum wells, Nat. Phys. **7**, 490 (2011).
[21] P. Rodriguez-Lopez, J. J. Betouras, and S. E. Savel'ev, Dirac fermion time-Floquet crystal: Manipulating Dirac points, Phys. Rev. B **89**, 155132 (2014).
[22] T. Iadecola, D. Campbell, C. Chamon, C.-Y. Hou, R. Jackiw, S.-Y. Pi, and S. V. Kusminskiy, Materials Design from Nonequilibrium Steady States: Driven Graphene as a Tunable Semiconductor with Topological Properties, Phys. Rev. Lett. **110**, 176603 (2013).
[23] M. A. Sentef, M. Claassen, A. F. Kemper, B. Moritz, T. Oka, J. K. Freericks, and T. P. Devereaux, Theory of pump-probe photoemission in graphene: Ultrafast tuning of Floquet bands and local pseudospin textures, Nat. Commun. **6**, 7047 (2015).
[24] M. Först, C. Manzoni, S. Kaiser, Y. Tomioka, Y. Tokura, R. Merlin, and A. Cavalleri, Nonlinear phononics as an ultrafast route to lattice control, Nat. Phys. **7**, 854 (2011).
[25] A. Subedi, A. Cavalleri, and A. Georges, Theory of nonlinear phononics for coherent light control of solids, Phys. Rev. B **89**, 220301(R) (2014).
[26] A. von Hoegen, R. Mankowsky, M. Fechner, M. Först, and A. Cavalleri, Probing the interatomic potential of solids with strong-field nonlinear phononics, Nature (London) **555**, 79 (2018).
[27] A. M. Läuchli and C. Kollath, Spreading of correlations and entanglement after a quench in the one-dimensional Bose-Hubbard model, J. Stat. Mech. (2008) P05018.
[28] S. A. Hamerla and G. S. Uhrig, One-dimensional fermionic systems after interaction quenches and their description by bosonic field theories, New J. Phys. **15**, 073012 (2013).
[29] S. Paeckel, B. Fauseweh, A. Osterkorn, T. Köhler, D. Manske, and S. R. Manmana, Detecting superconductivity out of equilibrium, Phys. Rev. B **101**, 180507(R) (2020).
[30] L. Schwarz, B. Fauseweh, N. Tsuji, N. Cheng, N. Bittner, H. Krull, M. Berciu, G. S. Uhrig, A. P. Schnyder, S. Kaiser, and D. Manske, Classification and characterization of nonequilibrium Higgs modes in unconventional superconductors, Nat. Commun. **11**, 287 (2020).
[31] B. Fauseweh and J.-X. Zhu, Laser pulse driven control of charge and spin order in the two-dimensional Kondo lattice, Phys. Rev. B **102**, 165128 (2020).
[32] M. Rigol, Quantum quenches and thermalization in one-dimensional fermionic systems, Phys. Rev. A **80**, 053607 (2009).
[33] J. Berges, Sz. Borsányi, and C. Wetterich, Prethermalization, Phys. Rev. Lett. **93**, 142002 (2004).
[34] T. Oka and S. Kitamura, Floquet engineering of quantum materials, Annu. Rev. Condens. Matter Phys. **10**, 387 (2019).
[35] E. Arrigoni, M. Knap, and W. von der Linden, Nonequilibrium Dynamical Mean-Field Theory: An Auxiliary Quantum Master Equation Approach, Phys. Rev. Lett. **110**, 086403 (2013).
[36] H. Aoki, N. Tsuji, M. Eckstein, M. Kollar, T. Oka, and P. Werner, Nonequilibrium dynamical mean-field theory and its applications, Rev. Mod. Phys. **86**, 779 (2014).
[37] T. Qin and W. Hofstetter, Nonequilibrium steady states and resonant tunneling in time-periodically driven systems with interactions, Phys. Rev. B **97**, 125115 (2018).
[38] M. Eckstein and P. Werner, Ultrafast Separation of Photodoped Carriers in Mott Antiferromagnets, Phys. Rev. Lett. **113**, 076405 (2014).
[39] Y. Murakami and P. Werner, Nonequilibrium steady states of electric field-driven Mott insulators, Phys. Rev. B **98**, 075102 (2018).
[40] A. Herrmann, Y. Murakami, M. Eckstein, and P. Werner, Floquet prethermalization in the resonantly driven Hubbard model, Europhys. Lett. **120**, 57001 (2018).
[41] G. Lindblad, On the generators of quantum dynamical semigroups, Comm. Math. Phys. **48**, 119 (1976).
[42] H.-P. Breuer and F. Petruccione, *The Theory of Open Quantum Systems*, 2nd ed. (Oxford University Press, Oxford, 2007).
[43] U. Weiss, *Quantum Dissipative Systems*, 2nd ed. (World Scientific, Singapore, 2012).
[44] S. A. Sato, P. Tang, M. A. Sentef, U. De Giovannini, H. Hübener, and A. Rubio, Light-induced anomalous Hall effect in massless Dirac fermion systems and topological insulators with dissipation, New J. Phys. **21**, 093005 (2019).
[45] M. Babadi, M. Knap, I. Martin, G. Refael, and E. Demler, Theory of parametrically amplified electron-phonon superconductivity, Phys. Rev. B **96**, 014512 (2017).
[46] F. Lange, Z. Lenarčič, and A. Rosch, Pumping approximately integrable systems, Nat. Commun. **8**, 15767 (2017).
[47] Z. Lenarčič, E. Altman, and A. Rosch, Activating Many-Body Localization in Solids by Driving with Light, Phys. Rev. Lett. **121**, 267603 (2018).
[48] F. Peronaci, O. Parcollet, and M. Schiró, Enhancement of local pairing correlations in periodically driven Mott insulators, Phys. Rev. B **101**, 161101(R) (2020).
[49] N. Walldorf, D. M. Kennes, J. Paaske, and A. J. Millis, The antiferromagnetic phase of the Floquet-driven Hubbard model, Phys. Rev. B **100**, 121110(R) (2019).
[50] Y. Murakami, N. Tsuji, M. Eckstein, and P. Werner, Nonequilibrium steady states and transient dynamics of conventional superconductors under phonon driving, Phys. Rev. B **96**, 045125 (2017).
[51] T. Prosen, Open XXZ Spin Chain: Nonequilibrium Steady State and a Strict Bound on Ballistic Transport, Phys. Rev. Lett. **106**, 217206 (2011).
[52] M. Žnidarič, T. Prosen, and P. Prelovšek, Many-body localization in the Heisenberg XXZ magnet in a random field, Phys. Rev. B **77**, 064426 (2008).
[53] J. Z. Imbrie, On many-body localization for quantum spin chains, J. Stat. Phys. **163**, 998 (2016).
[54] S. A. Weidinger and M. Knap, Floquet prethermalization and regimes of heating in a periodically driven, interacting quantum system, Sci. Rep. **7**, 45382 (2017).
[55] B. Žunkovič, M. Heyl, M. Knap, and A. Silva, Dynamical Quantum Phase Transitions in Spin Chains with Long-Range Interactions: Merging Different Concepts of Nonequilibrium Criticality, Phys. Rev. Lett. **120**, 130601 (2018).
[56] A. Greilich, A. Shabaev, D. Yakovlev, Al. L. Efros, I. A. Yugova, D. Reuter, A. D. Wieck, and M. Bayer, Nuclei-induced frequency focusing of electron spin coherence, Science **317**, 1896 (2007).
[57] I. Kleinjohann, E. Evers, P. Schering, A. Greilich, G. S. Uhrig, M. Bayer, and F. B. Anders, Magnetic field dependency of electron spin revival amplitude in periodically pulsed quantum dots, Phys. Rev. B **98**, 155318 (2018).

[58] R. Shindou, R. Matsumoto, S. Murakami, and J.-i. Ohe, Topological chiral magnonic edge mode in a magnonic crystal, Phys. Rev. B **87**, 174427 (2013).

[59] K. Nakata, S. K. Kim, J. Klinovaja, and D. Loss, Magnonic topological insulators in antiferromagnets, Phys. Rev. B **96**, 224414 (2017).

[60] X. S. Wang, H. W. Zhang, and X. R. Wang, Topological Magnonics: A Paradigm for Spin-Wave Manipulation and Device Design, Phys. Rev. Appl. **9**, 024029 (2018).

[61] M. Malki and G. S. Uhrig, Topological magnon band for magnonics, Phys. Rev. B **99**, 174412 (2019).

[62] C. Broholm, R. J. Cava, S. A. Kivelson, D. G. Nocera, M. R. Norman, and T. Senthil, Quantum spin liquids, Science **367**, eaay0668 (2020).

[63] S. Gao, O. Zaharko, V. Tsurkan, Y. Su, J. S. White, G. S. Tucker, B. Roessli, F. Bourdarot, R. Sibille, D. Chernyshov *et al.*, Spiral spin-liquid and the emergence of a vortex-like state in $MnSc_2S_4$, Nat. Phys. **13**, 157 (2017).

[64] S. A. Díaz, J. Klinovaja, and D. Loss, Topological Magnons and Edge States in Antiferromagnetic Skyrmion Crystals, Phys. Rev. Lett. **122**, 187203 (2019).

[65] P. Wadley, B. Howells, J. Železný, C. Andrews, V. Hills, R. P. Campion, V. Novák, K. Olejník, F. Maccherozzi, S. S. Dhesi *et al.*, Electrical switching of an antiferromagnet, Science **351**, 587 (2016).

[66] R. Lebrun, A. Ross, S. A. Bender, A. Qaiumzadeh, L. Baldrati, J. Cramer, A. Brataas, R. A. Duine, and M. Kläui, Tunable long-distance spin transport in a crystalline antiferromagnetic iron oxide, Nature (London) **561**, 222 (2018).

[67] H. Yu, S. D. Brechet, and J.-P. Ansermet, Spin caloritronics, origin and outlook, Phys. Lett. A **381**, 825 (2017).

[68] M. Gibertini, M. Koperski, A. F. Morpurgo, and K. S. Novoselov, Magnetic 2D materials and heterostructures, Nature Nanotech. **14**, 408 (2019).

[69] T. Li, A. Patz, L. Mouchliadis, J. Yan, T. A. Lograsso, I. E. Perakis, and J. Wang, Femtosecond switching of magnetism via strongly correlated spin-charge quantum excitations, Nature (London) **496**, 69 (2013).

[70] D. Bossini, S. Dal Conte, Y. Hashimoto, A. Secchi, R. V. Pisarev, Th. Rasing, G. Cerullo, and A. V. Kimel, Macrospin dynamics in antiferromagnets triggered by sub-20 femtosecond injection of nanomagnons, Nat. Commun. **7**, 10645 (2016).

[71] D. Bossini, S. Dal Conte, G. Cerullo, O. Gomonay, R. V. Pisarev, M. Borovsak, D. Mihailovic, J. Sinova, J. H. Mentink, Th. Rasing, and A. V. Kimel, Laser-driven quantum magnonics and terahertz dynamics of the order parameter in antiferromagnets, Phys. Rev. B **100**, 024428 (2019).

[72] M. Jäckl, V. I. Belotelov, I. A. Akimov, I. V. Savochkin, D. R. Yakovlev, A. K. Zvezdin, and M. Bayer, Excitation of Magnon Accumulation by Laser Clocking as a Source of Long-Range Spin Waves in Transparent Magnetic Films, Phys. Rev. X **7**, 021009 (2017).

[73] S. Manipatruni, D. E. Nikonov, C.-C. Lin, T. A. Gosavi, H. Liu, B. Prasad, Y.-L. Huang, E. Bonturim, R. Ramesh, and I. A. Young, Scalable energy-efficient magnetoelectric spin–orbit logic, Nature (London) **565**, 35 (2019).

[74] T. S. Seifert, S. Jaiswal, J. Barker, S. T. Weber, I. Razdolski, J. Cramer, O. Gueckstock, S. F. Maehrlein, L. Nadvornik, S. Watanabe *et al.*, Femtosecond formation dynamics of the spin Seebeck effect revealed by terahertz spectroscopy, Nat. Commun. **9**, 2899 (2018).

[75] B. S. Shastry and B. I. Shraiman, Theory of Raman Scattering in Mott-Hubbard Systems, Phys. Rev. Lett. **65**, 1068 (1990).

[76] J. H. Mentink, K. Balzer, and M. Eckstein, Ultrafast and reversible control of the exchange interaction in Mott insulators, Nat. Commun. **6**, 6708 (2015).

[77] A. A. Melnikov, K. N. Boldyrev, Yu. G. Selivanov, V. P. Martovitskii, S. V. Chekalin, and E. A. Ryabov, Coherent phonons in a Bi_2Se_3 film generated by an intense single-cycle THz pulse, Phys. Rev. B **97**, 214304 (2018).

[78] F. Giorgianni, B. Wehinger, S. Allenspach, N. Colonna, C. Vicario, P. Puphal, E. Pomjakushina, B. Normand, and Ch. Rüegg, Nonlinear quantum magnetophononics in $SrCu_2(BO_3)_2$, arXiv:2101.01189.

[79] R. Singla, G. Cotugno, S. Kaiser, M. Först, M. Mitrano, H. Y. Liu, A. Cartella, C. Manzoni, H. Okamoto, T. Hasegawa *et al.*, THz-Frequency Modulation of the Hubbard U in an Organic Mott Insulator, Phys. Rev. Lett. **115**, 187401 (2015).

[80] D. M. Kennes, E. Y. Wilner, D. R. Reichman, and A. J. Millis, Transient superconductivity from electronic squeezing of optically pumped phonons, Nat. Phys. **13**, 479 (2017).

[81] M. A. Sentef, Light-enhanced electron-phonon coupling from nonlinear electron-phonon coupling, Phys. Rev. B **95**, 205111 (2017).

[82] F. Grandi, J. Li, and M. Eckstein, Ultrafast Mott transition driven by nonlinear phonons, arXiv:2005.14100 [Phys. Rev. B (to be published)].

[83] T. F. Nova, A. Cartella, A. Cantaluppi, M. Först, D. Bossini, R. V. Mikhaylovskiy, A. V. Kimel, R. Merlin, and A. Cavalleri, An effective magnetic field from optically driven phonons, Nat. Phys. **13**, 132 (2017).

[84] M. Fechner, A. Sukhov, L. Chotorlishvili, C. Kenel, J. Berakdar, and N. A. Spaldin, Magnetophononics: Ultrafast spin control through the lattice, Phys. Rev. Materials **2**, 064401 (2018).

[85] G. Mazza and A. Georges, Superradiant Quantum Materials, Phys. Rev. Lett. **122**, 017401 (2019).

[86] M. A. Sentef, M. Ruggenthaler, and A. Rubio, Cavity quantum-electrodynamical polaritonically enhanced electron-phonon coupling and its influence on superconductivity, Sci. Adv. **4**, eaau6969 (2018).

[87] S. Sachdev and R. Bhatt, Bond-operator representation of quantum spins: Mean-field theory of frustrated quantum Heisenberg antiferromagnets, Phys. Rev. B **41**, 9323 (1990).

[88] S. Gopalan, T. M. Rice, and M. Sigrist, Spin ladders with spin gaps: A description of a class of cuprates, Phys. Rev. B **49**, 8901 (1994).

[89] M. Matsumoto, B. Normand, T. M. Rice, and M. Sigrist, Field- and pressure-induced magnetic quantum phase transitions in $TlCuCl_3$, Phys. Rev. B **69**, 054423 (2004).

[90] K. P. Schmidt and G. S. Uhrig, Excitations in One-Dimensional $S = 1/2$ Quantum Antiferromagnets, Phys. Rev. Lett. **90**, 227204 (2003).

[91] Ch. Rüegg, B. Normand, M. Matsumoto, Ch. Niedermayer, A. Furrer, K. W. Krämer, H. U. Güdel, Ph. Bourges, Y. Sidis, and H. Mutka, Quantum Statistics of Interacting Dimer Spin Systems, Phys. Rev. Lett. **95**, 267201 (2005).

[92] B. Normand and Ch. Rüegg, Complete bond-operator theory of the two-chain spin ladder, Phys. Rev. B **83**, 054415 (2011).

[93] B. Fauseweh and G. S. Uhrig, Low-temperature thermodynamics of multiflavored hardcore bosons by the Brückner approach, Phys. Rev. B **92**, 214417 (2015).
[94] M. Hase, I. Terasaki, and K. Uchinokura, Observation of the Spin-Peierls Transition in Linear Cu^{2+} (Spin-1/2) Chains in an Inorganic Compound $CuGeO_3$, Phys. Rev. Lett. **70**, 3651 (1993).
[95] R. Werner, C. Gros, and M. Braden, Microscopic spin-phonon coupling constants in $CuGeO_3$, Phys. Rev. B **59**, 14356 (1999).
[96] G. S. Uhrig, Symmetry and Dimension of the Dispersion of Inorganic Spin-Peierls Systems, Phys. Rev. Lett. **79**, 163 (1997).
[97] Z. V. Popović, S. D. Dević, V. N. Popov, G. Dhalenne, and A. Revcolevschi, Phonons in $CuGeO_3$ studied using polarized far-infrared and Raman-scattering spectroscopies, Phys. Rev. B **52**, 4185 (1995).
[98] T. Lorenz, H. Kierspel, S. Kleefisch, B. Büchner, E. Gamper, A. Revcolevschi, and G. Dhalenne, Specific heat, thermal expansion, and pressure dependencies of the transition temperatures of doped $CuGeO_3$, Phys. Rev. B **56**, R501 (1997).
[99] C. Ecolivet, M. Saint-Paul, G. Dhalenne, and A. Revcolevschi, Brillouin scattering and ultrasonic measurements of the elastic constants of $CuGeO_3$, J. Phys. Condens. Matter **11**, 4157 (1999).
[100] M. Hofmann, T. Lorenz, A. Freimuth, G. S. Uhrig, H. Kageyama, Y. Ueda, G. Dhalenne, and A. Revcolevschi, Heat transport in $SrCu_2(BO_3)_2$ and $CuGeO_3$, Physica B **312-313**, 597 (2002).
[101] P. Duthil, Material properties at low temperature, CERN Yellow Report **5**, 77 (2014).
[102] C. Knetter and G. S. Uhrig, Perturbation theory by flow equations: Dimerized and frustrated $S = 1/2$ chain, Eur. Phys. J. B **13**, 209 (2000).
[103] C. Knetter, K. P. Schmidt, and G. S. Uhrig, The structure of operators in effective particle-conserving models, J. Phys. A: Math. Gen. **36**, 7889 (2003).
[104] H. Krull, N. A. Drescher, and G. S. Uhrig, Enhanced perturbative continuous unitary transformations, Phys. Rev. B **86**, 125113 (2012).
[105] M. Vogl, P. Laurell, A. D. Barr, and G. A. Fiete, Flow Equation Approach to Periodically Driven Quantum Systems, Phys. Rev. X **9**, 021037 (2019).
[106] S. Diehl, A. Micheli, A. Kantian, H. P. Büchler, and P. Zoller, Quantum states and phases in driven open quantum systems with cold atoms, Nat. Phys. **4**, 878 (2008).
[107] W. Berdanier, M. Kolodrubetz, R. Vasseur, and J. E. Moore, Floquet Dynamics of Boundary-Driven Systems at Criticality, Phys. Rev. Lett. **118**, 260602 (2017).
[108] T. Kampfrath, K. Tanaka, and K. A. Nelson, Resonant and nonresonant control over matter and light by intense terahertz transients, Nat. Photonics **7**, 680 (2013).
[109] X. C. Zhang, A. Shkurinov, and Y. Zhang, Extreme terahertz science, Nat. Photonics **11**, 16 (2017).
[110] P. Salén, M. Basini, S. Bonetti, J. Hebling, M. Krasilnikov, A. Y. Nikitin, G. Shamuilov, Z. Tibai, V. Zhaunerchyk, and V. Goryashko, Matter manipulation with extreme terahertz light: Progress in the enabling THz technology, Phys. Rep. **836-837**, 1 (2019).
[111] D. A. Tennant, B. Lake, A. J. A. James, F. H. L. Essler, S. Notbohm, H.-J. Mikeska, J. Fielden, P. Kögerler, P. C. Canfield, and M. T. F. Telling, Anomalous dynamical line shapes in a quantum magnet at finite temperature, Phys. Rev. B **85**, 014402 (2012).
[112] N. Ahmed, P. Khuntia, K. M. Ranjith, H. Rosner, M. Baenitz, A. A. Tsirlin, and R. Nath, Alternating spin chain compound $AgVOAsO_4$ probed by ^{75}As NMR, Phys. Rev. B **96**, 224423 (2017).
[113] U. Arjun, K. M. Ranjith, B. Koo, J. Sichelschmidt, Y. Skourski, M. Baenitz, A. A. Tsirlin, and R. Nath, Singlet ground state in the alternating spin-1/2 chain compound $NaVOAsO_4$, Phys. Rev. B **99**, 014421 (2019).
[114] I. S. Jacobs, J. W. Bray, H. R. Hart, L. V. Interrante, J. S. Kasper, G. D. Watkins, D. E. Prober, and J. C. Bonner, Spin-Peierls transitions in magnetic donor-acceptor compounds of tetrathiafulvalene (TTF) with bisdithiolene metal complexes, Phys. Rev. B **14**, 3036 (1976).
[115] M. C. Cross and D. S. Fisher, A new theory of the spin-Peierls transition with special relevance to the experiments on TTFCuBDT, Phys. Rev. B **19**, 402 (1979).
[116] S. Huizinga, J. Kommandeur, G. A. Sawatzky, B. T. Thole, K. Kopinga, J. M. de Jonge, and J. Roos, Spin-Peierls transition in N-methyl-N-ethylmorpholinium-ditetracyanoquinodimethanide [MEM-$(TCNQ)_2$], Phys. Rev. B **19**, 4723 (1979).
[117] Y. Miura, R. Hirai, Y. Kobayashi, and M. Sato, Spin-gap behavior of $Na_3Cu_2SbO_6$ with distorted honeycomb structure, J. Phys. Soc. Jpn. **75**, 084707 (2006).
[118] M. B. Stone, W. Tian, M. D. Lumsden, G. E. Granroth, D. Mandrus, J.-H. Chung, N. Harrison, and S. E. Nagler, Quantum Spin Correlations in an Organometallic Alternating-Sign Chain, Phys. Rev. Lett. **99**, 087204 (2007).
[119] G. S. Uhrig and B. Normand, Magnetic properties of $(VO)_2P_2O_7$ from frustrated interchain coupling, Phys. Rev. B **58**, R14705 (1998).
[120] G. S. Uhrig and B. Normand, Magnetic properties of $(VO)_2P_2O_7$: Two-plane structure and spin-phonon interactions, Phys. Rev. B **63**, 134418 (2001).
[121] F. A. Lindemann, Über die Berechnung molekularer Eigenfrequenzen, Phys. Z. **11**, 609 (1910).
[122] J. J. Gilvarry, The Lindemann and Grüneisen laws, Phys. Rev. **102**, 308 (1956).
[123] J. Dudowicz, K. F. Freed, and J. F. Douglas, Generalized entropy theory of polymer glass formation, Adv. Chem. Phys. **137**, 125 (2008).
[124] R. Gross and A. Marx, *Festkörperphysik* (Oldenbourg, Munich, 2012).
[125] M. Born and J. R. Oppenheimer, Zur Quantentheorie der Molekülen, Ann. Phys. **84**, 457 (1927).

Correction: The omission of a support statement in the Acknowledgment section has been fixed.